ABSTRACT

LUISO, SALVATORE. Separators and Electrolytes for Next Generation Li-Ion Batteries (Under the direction of Dr. Peter S. Fedkiw and Richard J. Spontak).

The focus of this research is to understand the inherent features of separators for Li-ion batteries and enable the production of fiber-based separators, whose structures are significantly different from the coherent polyolefin-based membranes currently employed in these batteries. The first hypothesis of this work is that the structure of fiber mats plays a significant role in its performance as a separator in a Li-ion cell; specifically, processing conditions used in meltblowing polyvinylidene difluoride (PVDF), a polymer used in common Li-ion batteries, may be tuned to control the fiber-mat structure, affecting its end-use in batteries. The second hypothesis of this work is that a shear-spinning process from a PVDF solution to form a separator may be used to produce a unique mat structure by influencing the morphology of shear-spun particles that form the basis of the separator.

Although significant research has been reported on electrospinning of PVDF, there are no studies reported known to us on the formation and characterization of PVDF meltblown mats because of technological barriers associated with meltblowing the polymer. We investigated the fundamental properties and characteristics of meltblown mats produced with an experimental grade of melt-blowable PVDF (Kynar® resin RC 10,287, Arkema, Inc.), with the objective of elucidating their structure-property-process relationships. With a Biax lab-scale equipment, we produced high-quality meltblown PVDF mats with low solid-volume percent (~ 22%), and an average fiber diameter varying from 2 to 6 μm.

To elucidate the performance of meltblown PVDF as a separator in Li-ion batteries, we used a 1.2-m wide Reicofil R4 meltblown pilot line at the Nonwovens Institute at NC State to fabricate high-quality meltblown PVDF mats. The resulting mats showed an average pore size as

small as 0.9 μm, and fiber diameter as small as 1.4 μm, yielding high surface area and high electrolyte uptake. The highest ionic conductivity of the electrolyte-infused mat was ~ 9.6 mS/cm (with 1M $LiPF_6$ in EC/DMC 1:1 v/v) at room temperature, and the first-cycle capacity of a $Li/LiCoO_2$ cell containing meltblown PVDF separators was 142 mAh/g (vs. 146 mAh/g for state-of-art polyolefin separator).

With the objective of investigating a new class of fibrous PVDF separators, we produced highly-branched, colloidal polymer particulates, called soft dendritic colloids, with a shear-driven polymer precipitation process. We show the morphology of the resulting PVDF particulates may be varied from fibrous to highly porous sheet-like particles depending upon the process conditions. Separators made with these particulates show low thermal shrinkage (5% at 90 ºC) and high tensile strength (<0.7% offset at 1000 psi), while the porosity (up to 80%) and particle surface area are responsible for high conductivity (1.2 mS/cm), electrolyte uptake (325%), and acceptable cell capacity (112 mAh/g in $Li/LiCoO_2$ cell) with <10% loss after 50 cycles.

We used meltblowing, electrospinning, and the high-shear precipitation process to fabricate PVDF separators with different fiber/pore diameter and distributions to draw correlations between the membranes' morphology and the electrochemical performance in a $Li/LiCoO_2$ cell. All samples showed the same trend, *i.e.* when the fiber/pore distribution was widened and/or pore size decreased, the capacity loss decreased and cycling stability increased. This effect was accentuated at C-rates higher than C/5, suggesting that the separator structure is a crucial factor to enable high-rate cycling of Li-ion batteries.

This work shows that by using a technique that precisely fabricates fibrous or fibrous-like homogeneous mats, separators may be produced with an optimal structure to improve the cycling

performance of Li-ion batteries by efficiently designing the network with a small average pore size and a wide-pore size distribution.

Separators and Electrolytes for Next Generation Li-Ion Batteries

by
Salvatore Luiso

A dissertation submitted to the Graduate Faculty of
North Carolina State University
in partial fulfillment of the
requirements for the degree of
Doctor of Philosophy

Chemical Engineering

Raleigh, North Carolina
2021

APPROVED BY:

Peter S. Fedkiw Committee Co-chair	Richard J. Spontak Committee Co-chair
Saad A. Khan	Behnam Pourdeyhimi

DEDICATION

To my parents, Viola and Giacomo, for their constant support and unconditional love.

BIOGRAPHY

Salvatore Luiso was born on March 8th, 1991, in Rimini, Italy. He grew up with his parents, Giacomo and Viola, and his brothers, Federico and Filippo. Salvatore is now married to Angela D'Orio. From a young age, he was fascinated by studying and playing musical instruments, which led him to obtain a master's degree in Clarinet in 2010 at the State Academy of Music in Pesaro. In the same year, Salvatore moved to Bologna, to pursue his undergraduate and graduate studies in Chemical and Biochemical Engineering at the University of Bologna. These studies drove his mind toward the world of electrochemical engineering. In 2014 he joined the Department of Chemical and Biomolecular Engineering at NC State to pursue his third master's degree. Salvatore joined Dr. Peter Fedkiw's group to conduct research on MoS_2 as a catalyst for hydrogen evolution reaction. After one year of intense work, Salvatore defends his master's thesis, after which he joined the Ph.D. program in the same department under the supervision of Dr. Fedkiw and Dr. Spontak, with the collaboration of Dr. Pourdeyhimi and the Nonwovens Institute. In 2019 he received a Graduate Certificate in Nonwovens Science and Technology and multiple awards in 2020.

In January 2021, Salvatore will move to Phoenix, Arizona, where he will work for ASM International as a Senior Process Engineer.

ACKNOWLEDGMENTS

I would like to gratefully and sincerely thank my advisor Dr. Peter S. Fedkiw for his guidance, understanding, and patience during my graduate studies at North Carolina State University. His mentorship was paramount in providing a well-rounded experience consistent my long-term career goals. He encouraged me to not only grow as an experimentalist and an engineer but also as a leader and an independent thinker. Not all graduate students are given the opportunity to develop their own individuality and self-sufficiency by being allowed to work with such independence. I would like to give my most sincere appreciation to my committee members, Dr. Saad Khan, Dr. Behanm Pourdeyhimi, and my co-chair Dr. Richard Spontak. The financial support of the first three years of my Ph.D. from the Nonwovens Institute (NWI) is also greatly appreciated.

I would like to thank the members of the Fedkiw research group, Mike and Sam, and all the students at NWI for their support and friendship. I also would like to thank the administrative staff, Sandra, Joan , Nancy, Angela and Jimei for their help and trouble shooting skills.

Finally, I am thankful to my wife Angela, my parents Viola and Giacomo, for their love and encouragement during my years of studies.

TABLE OF CONTENTS

LIST OF TABLES

LIST OF FIGURES

Chapter 2

Chapter 3

Chapter 4

Chapter 5

Chapter 6

Appendix A

Appendix B

Appendix C

Appendix D

CHAPTER 1: Introduction

In this research we aim to understand how alternatives to coherent membrane-type polyolefin separators can be developed from nonwoven or nonwoven-like processes using polyvinylidene difluoride (PVDF), a common binder material used in current Li-ion batteries. Our hypothesis is that meltblowing can be used to fabricate nonwoven PVDF mats and processing conditions can be tuned to affect the structure of the mats. We hypothesize that the structure of the fiber mats plays a significant role in the performance of the separator in a Li-ion cell. The second hypothesis is that a shear-spinning process may be used to produce a separator through control of the morphology of the web-forming PVDF particles and, therefore, the in-use separator performance in a cycled cell.

In order to explore these hypotheses, a systematic approach was developed, and it is expanded upon in chapter 2 through 6 in this dissertation. A summary of each chapter follows. In Appendix A, we investigate a quasi-solid state electrolyte, a summary of which follows. In Appendices B, C, and D we present supplemental information for Chapters 3, 4, and 5, respectively.

Chapter 2: Li-ion battery separators: recent developments and state-of-art

(Luiso S., Fedkiw P.S., *Curr Opin Electrochem*, 2020, 20, 99–107)

Li-ion batteries have received significant attention for their increasing ability to store energy. While the anode and cathode materials attract most scientific research, the separator, which is placed between the electrodes to prevent their physical contact and to store electrolyte, plays a critical role in a battery's operation. With increasing energy density demands in Li cells, separators properties have been adapted to stricter requirements, such as high thermal and mechanical stability or high electrolyte wettability [1]. In general, modern Li-ion batteries are affected by three

major degradation modes: (1) dissolution of transition metals from positive electrodes; (2) chemical loss of Li^+ ions; and (3) decomposition of solution components [2]. New battery separators and electrolytes need to address and possibly mitigate battery degradation by means of a reduced ionic resistance, improved network for an optimal lithium-ion flow, homogeneous structure, and possibly functionalized separators.

In Chapter 2, we discuss current trends for Li-ion battery separators. We introduce and analyze the characteristics, performance and modifications of single- and multi-layer, ceramic-based, and multifunctional separators.

Chapter 3: Fabrication and Characterization of Meltblown Poly(Vinylidene difluoride) Membranes

(Luiso, S., Henry, J.J., Pourdeyhimi, B., Fedkiw, P.S., *ACS Appl. Polym. Mater*., 2020, 2, 2849–2857)

Commercial separators are usually coherent continuous microporous membranes mainly made of polyethylene (PE) and/or polypropylene (PP). However, hydrophobic nonpolar polyolefins usually require surfactants to obtain good electrolyte wettability [3]. Nonwoven separators, in constrast, possess fibrous structures that allow a high electrolyte uptake with good structural cohesion due to strong fiber-fiber bonds within the mat. An advantageous manner to produce nonwoven separators would employ a meltblowing process, which is a well-developed, high-volume production technology to fabricate mats with randomly oriented and small-diameter (1-5 μm) fibers. Meltblown structures can be formed in several ways; today, there are mainly two processes: the Reicofil system and the Biax process. The Biax process uses a die with multiple rows of orifices each with a co-centric air stream where each fiber is enveloped by the air supply. Multiple rows are essential for high productivity despite a capillary density lower than the Reicofil

process, where instead the polymer melt is delivered to a single row of closely packed orifices and a high-velocity stream of heated air impinges on the collection of molten filaments as they exit the orifices. In the Biax process, the nozzles cannot be as closely packed as in the Reicofil system, and therefore to compensate for the fewer capillaries in a row, the Biax die uses multiple rows.

Among other polymers, poly(vinylidene fluoride) (PVDF) is a promising material for battery separators due to high polarity, low degree of crystallinity, high dielectric constant, good chemical stability, and good electrolyte wettability owing to the presence of C–F group [4,5]. To be melt-blowable, polymer resins must have high melt-flow rates, but commercial PVDF resins did not possess this property until recently [6–8]. The technological barriers associated with meltblowing PVDF at reasonable processing temperatures include an inadequate melt flow rate, which cannot be overcome by increasing the temperature due to thermal decomposition and possible generation of hydrogen fluoride [9]. By means of specific chain-transfer agents in high levels during polymerization, melt-blowable PVDF has recently been developed (Kynar® resin RC 10,287, Arkema, Inc.) [7]. These types of nonwoven structures are unobtainable with previous commercial PVDF because of the low-melt strength or low-extensional viscosity of the polymer.

In Chapter 3, we report the fabrication of meltblown PVDF mats with a lab-scale Biax meltblowing apparatus. A full characterization is reported, including fiber and membrane characteristics of the resulting webs. Process-structure-properties relationships are discussed.

Chapter 4: Meltblown PVDF as A Li-Ion Battery Separator

(Luiso, S., Henry, J.J., Pourdeyhimi, B., Fedkiw, P.S., submitted *ACS Appl. Polym. Mater.*, 2021)

Despite the simplicity of the Biax meltblown process on a small scale, the Reicofil system is dominant at the commercial scale and employed for the formation of microfibers for membranes

in a variety of applications, from barriers in the medical industry to filtration media. However, because the meltblowing equipment is not readily available at universities and PVDF resin was not melt-blowable until recently, researchers have used the electrospinning process to explore nonwoven PVDF battery separators [10]. In spite of promising results, the simplicity, and ability of electrospinning to produce functional nanofibers, electrospinning is inherently slow, expensive, and solvent intensive compared to meltblowing. Electrospun PVDF mats also often require a supporting matrix to use as battery separators because of their low mechanical strength. Meltblowing, however, has significant advantages over electrospinning, such as high processing speeds and solvent-free operation. Meltblowing also has the potential to fabricate unique structures, blends, and composites unobtainable by electrospinning. In particular, with the meltblowing process, it is possible to obtain desired structures in a controlled way, *e.g.* specific mat thickness, fiber diameter distribution, solidity, etc. [11].

In Chapter 4, we use a Reicofil meltblowing pilot-plant equipment to produce high-quality meltblown PVDF mats. We report the physical, chemical, and electrochemical properties of meltblown PVDF relevant to its use as a Li-ion battery separator.

Chapter 5: Poly(Vinylidene difluoride) Soft Dendritic Colloids as Li-Ion Battery Separators

(Luiso S., Williams A.H., Petrecca M.J., Roh S., Velev O.D., Fedkiw P.S., *J Electrochem Soc*., 168 020517, 2021)

A new method of fabricating nanofibrous material in which a polymer solution is injected into a sheared nonsolvent flow has shown that membranes fabricated with these materials may be produced in a continuous, scalable process using a laminar nonsolvent flow to elongate the polymer droplet into a fiber [12, 13], and the transition to a turbulent regime of the nonsolvent

alters the morphology resulting in highly branched soft dendritic colloids (SDCs) [14, 15]. The concentration of polymer in the injection solution dictates the morphology of the resulting particulates, from fibrous to thin nano-sheet (NS) morphologies.

In Chapter 5, we show that PVDF SDC membranes produced by shear-driven polymer precipitation may be used as separators in Li-ion cells, resulting in good cycling stability and high-rate capability. We also investigate how battery performance is effected by the particle morphology in the SDC-based separator resulting from the precipitation process.

Chapter 6: An Optimal Structure for Li-Ion Battery Fiber-Based Separators

(Luiso, S., Petrecca M.J., Williams A.H., Henry, J.J., Pourdeyhimi, B., Velev O.D., Fedkiw, P.S., in preparation for submission, *J Electrochem Soc*., 2021)

Different raw materials, combinations thereof, or manufacturing processes have attracted the attention of literature studies on battery separators [16–21], several of which showed correlations between physical and electrochemical properties of the separators [6,20,22–25]. However, these have been single-case studies and, even though the chemistry and membrane fabrication are important, only a few works have focused on understanding the role of separator structure on their electrochemical performance. Different separator morphologies may be obtained in the shear spinning process through the solvent-nonsolvent interactions (Chapter 5), and in the meltblowing process by changing the controlled variables (Chapters 3 and 4).

Nano-structured battery separators are attractive because of their high specific surface area and controllable compositions and pore structures. The fibrous network forms an interconnected nano- and microporous structure that provide both openness for enhanced lithium-ions transport and also tortuosity for Li dendrites suppression. While the trend of creating an efficient fibrous battery separator has moved toward the objective of achieving a pore size and distribution similar

to the well-established microporous membranes, *i.e.* small and uniform pore size, literature works do not clearly describe the effect that the pore network and distribution have on the electrochemical performance.

In Chapter 6, we use meltblowing, electrospinning, and a high-shear precipitation process to fabricate PVDF separators with different pore sizes and distributions. Here, we show for PVDF separators made with these three processes, a decrease in pore size and a widening of pore-size distribution in separators made with the same process result in higher electrolyte uptake and ionic conductivity of the mats, and higher discharge capacity and rate capability when cycled in $Li/LiCoO_2$ cells.

Chapter 7: Recommendations

We have demonstrated the possibility to melt-blow PVDF Kynar® resin RC 10,287 to produce a high quality mat. Fiber mats showed populations with 30-40% sub-micron fibers with diameters as small as <400 nm, but an investigation of the effect that different dies and capillary size have on the final mat structure would bring more insight on structure-property-process relationships and could possibly enable mats with smaller-diameter fibers. Li-ion batteries containing meltblown PVDF (Kynar® resin RC 10,287) separators showed long-term stability issues probably due to chain-transfer agents, additives and/or surfactants leached from the fibers and oxidized during battery operation. Meltblowing a higher purity PVDF resin would be worthwhile pursuing for solving cycling stability issues.

The morphology of the membranes may be adjusted in other unexplored ways, such as layering or mixing together SDC particles with two or more morphologies, which would tailor these membranes to specific applications. The versatility of the shear-precipitation process allows for multiple polymer precipitation, which include the investigation of new solvent/non-solvent

combinations, and for incorporation of additives such as ceramic particles, for composite separators

In Chapter 7, we discuss recommended future work to further explore the possibilities of using fiber mats as Li-ion battery separators with the objective of improving their performance during battery cycling operation. Unexplored ways of fabricating new particle morphologies are discussed and suggested experiments include the use of different dies and high-purity resins during meltblowing, 3D characterization of the fiber mat, and investigation of the effect that the β-phase has on separator performance.

Appendix A: Lithium-ion conducting water-in-salt sulfonated pentablock polymer as a quasi-solid-state electrolyte

(Luiso S., Quan T., Lu Y., Spontak R.J., Fedkiw P.S., *Advanced Energy Materials*, 2021, in preparation)

Aqueous electrolytes are an attractive alternative to common organic electrolytes and their stability window may be expanded with high concentration of Lithium salt to create a water-in-salt electrolyte (WiSE) [30]. The WISE is a liquid and in Appendix A we explore the use of midblock sulfonated pentablock co-polymer commercially known as Nexar® [26] as an ion conductive matrix in which to imbibe the WISE. The microphase-separated nanostructure of Nexar® allows for selective incorporation of polar electrolytes [27, 28] and ionic liquids [29] within the sulfonated microdomains of the polymer. Selective swelling of the sulfonated midblock provides nanoscale channels by which ions can transport, while maintaining structural integrity due to the elastomeric network, which is not possible with traditional polymer electrolytes.

In Appendix A, we describe exploratory work of a Li-ion conducting WiSE sulfonated pentablock co-polymer, and we report cycling performance of a MoS_3/$LiMnO_4$ cell with the

WiSE-polymer quasi-solid-state electrolyte. This work was carried out in conjunction with the Helmholtz-Zentrum Berlin für Materilien und Energie.

References

[1] Lagadec M.F., Zahn R., Wood V., "Characterization and performance evaluation of lithium-ion battery separators", *Nat. Energy*, vol. 4, no. 1, pp. 16–25, 2019.

[2] Banerjee A., Ziv B., Shilina Y., Ziegelbauer J.M., Liu H., Harris K.J., Botton G., Goward G.R., Luski S., Aurbach D., Halalay I.C., "Review—Multifunctional Separators: A Promising Approach for Improving the Durability and Performance of Li-Ion Batteries", *J. Electrochem. Soc.*, vol. 166, no. 3, pp. A5369–A5377, 2019.

[3] Abraham K.M., "Polymer Electrolytes Reinforced by Celgard® Membranes", *J. Electrochem.*, Soc. 142, 683, 1995.

[4] Waqas M., Ali S., Feng C., Chen D., Han J., He W., "Recent Development in Separators for High-Temperature Lithium-Ion Batteries", *Small*, 2019, vol. 15, no. 33.

[5] Barbosa J.C., Dias J.P., Lanceros-Méndez S., Costa C.M., "Recent advances in poly(Vinylidene fluoride) and its copolymers for lithium-ion battery separators", *Membranes (Basel)*, vol. 8, no. 3, 2018.

[6] Luiso S., Henry J. J., Pourdeyhimi B., Fedkiw P. S., "Fabrication and Characterization of Meltblown Poly(vinylidene difluoride) Membranes", *ACS Appl. Polym. Mater.*, 2, 2849–2857, 2020.

[7] Henry J.J., Goldbach J., Stabler S., Devisme S., Chauveau, J., "Advancements in the production of meltblown fibres", *Filtr. Sep.*, 53, 36–40, 2016.

[8] Goldbach J.T., Henry J.J., Stabler S.M., Chauveau J., High melt flow fluoropolymer composition, *US Patent Application No.20170088989(A1)*, Washington, DC: U.S. Patent and Trademark Office, 2017.

[9] Ebnesajjad S., Khaladkar P.R., “Fluoropolymer Applications in the Chemical Processing Industries”, second edition, *William Andrew*, Cambridge, MA, 2017.

[10] Li Y., Li Q., Tan Z., “A review of electrospun nanofiber-based separators for rechargeable lithium-ion batteries”, *J. Power Sources,* 443, 227262, 2019.

[11] Drabek J., Zatloukal M., “Meltblown technology for production of polymeric microfibers/nanofibers: A review”, *Physics of Fluids,* vol. 31, 2019.

[12] Velev O.D., Smoukov S., Geisen P., Wright M.C., Gangwal S., “Method for Fabricating Nanofibers”, US Patent No. 9217211B2, Washington, DC: U.S. Patent and Trademark Office, 2015.

[13] Velev O.D., Smoukov S., Marquez M. “Nanospinning of polymer fibers from sheared solutions”, US Patent No. 8551378, Washington, DC: U.S. Patent and Trademark Office, 2013.

[14] Velev O.D., Roh S. “Fractal-like polymeric particles and their use in diverse applications”, WIPO Patent No. 2017196864A1, 2017.

[15] Roh S., Williams A.H., Bang R.S., Stoyanov S.D., Velev O.D., “Soft dendritic microparticles with unusual adhesion and structuring properties”, *Nature Materials,* 18, 1315–1320, 2019.

[16] Fu Q., Lin G., Chen X., Yu Z., Yang R., Li M., Zeng X., Chen J., “Mechanically Reinforced PVdF/PMMA/SiO2 Composite Membrane and Its Electrochemical Properties as a Separator in Lithium-Ion Batteries”, *Energy Technol*, 6(1):144–52, 2018.

[17] Pan J.L., Zhang Z., Zhang H., Zhu P.P., Wei J.C., Cai J.X., Yu J., Koratkar N., Yang Z.Y., “Ultrathin and Strong Electrospun Porous Fiber Separator”, *ACS Appl Energy Mater,* 1(9):4794–803, 2018.

[18] Li M., Liao Y., Liu Q., Xu J., Sun P., Shi H., Li W., "Application of the imidazolium ionic liquid based nano-particle decorated gel polymer electrolyte for high safety lithium ion battery", *Electrochim Acta,* 10;284:188–201, 2018.

[19] Banerjee A., Ziv B., Shilina Y., Luski S., Halalay I.C., Aurbach D., "Multifunctional Manganese Ions Trapping and Hydrofluoric Acid Scavenging Separator for Lithium Ion Batteries Based on Poly(ethylene- alternate -maleic acid) Dilithium Salt", *Adv Energy Mater,* 7(3):1601556, 2017.

[20] Luiso S., Williams A.H., Petrecca M.J., Roh S., Velev O.D., Fedkiw P.S., "Poly(Vinylydene difluoride) Soft Dendritic Colloids as Li-Ion Battery Separators", *J Electrochem Soc,* 168 020517, 2021, 2021.

[21] Luiso S., Fedkiw P., "Lithium-ion battery separators: Recent developments and state of art", *Curr Opin Electrochem,* 20:99–107, 2020.

[22] Huang X., "Separator technologies for lithium-ion batteries", *J Solid State Electrochem,* 15(4):649–62, 2011.

[23] Venugopal G., Moore J., Howard J., Pendalwar S., "Characterization of microporous separators for lithium-ion batteries", *J Power Sources,* 77(1):34–41, 1999.

[24] Djian D., Alloin F., Martinet S., Lignier H., Sanchez J.Y., "Lithium-ion batteries with high charge rate capacity: Influence of the porous separator", *J Power Sources,* 172(1):416–21, 2007.

[25] Kim J.Y., Lim D.Y., "Surface-modified membrane as a separator for lithium-ion polymer battery", *Energies. Molecular Diversity Preservation International,* vol. 3, p. 866–85, 2010.

[26] Nexar, Kraton Polymers LLC, https://www.kraton.com/products/pdf/NEXAR_brochure.pdf

[27] Al-Mohsin H.A., Mineart K.P., Spontak R.J., "Highly Flexible Aqueous Photovoltaic Elastomer Gels Derived from Sulfonated Block Ionomers", *Adv Energy Mater, 5*(8):1401941, 2017.

[28] Mineart K.P., Al-Mohsin H.A., Lee B., Spontak R.J., "Water-induced nanochannel networks in self-assembled block ionomers", *Appl Phys Lett,* 108(10):101907, 2016.

[29] Vargantwar P.H., Roskov K.E., Ghosh T.K., Spontak R.J., "Enhanced Biomimetic Performance of Ionic Polymer–Metal Composite Actuators Prepared with Nanostructured Block Ionomers", *Macromol Rapid Commun,* 33(1):61–8, 2011.

[30] Suo L., Borodin O., Gao T., Olguin M., Ho J., Fan X., Luo C., Wang C., Xu K., "Water-in-salt electrolyte enables high-voltage aqueous lithium-ion chemistries", *Science,* 350(6263):938–43, 2014.

CHAPTER 2: Li-ion battery separators: recent developments and state-of-art

Abstract

Lithium-ion battery separators are receiving increased consideration from the scientific community. Single- and multi-layer separators are well-established technologies, and the materials used span from polyolefins to blends and composites of fluorinated polymers. The addition of ceramic nanoparticles and separator coatings improve thermal and mechanical properties, as well as electrolyte uptake and ionic conductivity. The state-of-art separators are actively involved in the cell chemistry through specific functional groups on their surface. Amongst the numerous properties, safety features and long-cycle life are high-priority requirements for next-generation Li-ion batteries.

Introduction

Owing to the demand for "green" products, Li-ion batteries have received considerable attention as an energy storage system [1,2]. Although the separator, which is placed between the anode and the cathode, is not directly involved in electrochemical reactions, its structure and its properties play an important role in cell performance. The primary purpose of the separator is to prevent the physical contact of electrodes while serving as the electrolyte reservoir to enable ion transport. Nowadays separators have new important requirements; for example, separators for electric vehicles or energy storage stations need high thermal and mechanical stability, together with a high electrolyte wettability [3]. Li-ion batteries experience critical issues when operated at extreme temperatures. The spatial and temporal fluctuations of temperature inside batteries originating from internal “hot spots” (regions of high current density) may result in internal short circuits and lead to thermal runaway [4]. Low temperatures (below 0 °C) are detrimental for Li-

ion battery performances with a loss in power and energy capabilities or even damage in the structure of cells [5].

While separators may be divided into categories according to their structure (such as microporous membranes, nonwoven mats, gel-polymer electrolytes, and composite membranes [6]), new trends suggest a classification based on number of layers, ceramics addition, and surface modification [5,7–9]. This change is due to a shift of focus from obtaining a specific membrane morphology to implementing new desired properties, especially in terms of safety. The state-of-art separators have a thickness less than 10 μm [1], and the risk of electrolyte degradation or dendrite formation is increased in batteries with high-energy density [2]. In general, modern Li-ion batteries are affected by three major degradation modes: (1) dissolution of transition metals from positive electrodes; (2) chemical loss of Li^+ ions; and (3) decomposition of solution components [9]. Large overpotentials prevent the theoretical voltage and specific capacity of the cell from being obtained and contribute to heat generation and lithium plating [10].

In this review, we discuss current trends for Li-ion battery separators. We introduce and analyze the characteristics, performance and modifications of single- and multi-layer, ceramic-based, and multifunctional separators (Fig. 1). Table 1 summarizes pertinent information about the separators discussed in this review.

Table 1. Summary of literature results on Li-ion battery separator

Material	Ion Conductivity (mS cm^{-1})	Thickness (μm)	Thermal shrinkage	Electrolyte uptake (wt%)	Tensile strength (MPa)	Preparation procedure	Ref.
PP/PE	1.35	25	~0%@150°C[1]	148	13	Multilayer coextrusion and $CaCO_3$ template method	21
PP/PE	1.46	25	3%@150°C	157	16	Multilayer coextrusion and thermal induced phase separation	20
PP/Silica aerogel	0.63	31	25%@160°C	346	N/R[2]	PP separator coated with PVDF and silica aerogel slurry	30
PP/Silicone	0.25	N/R	1%@160°C	96	N/R	$K_2Cr_2O_7$-activated PP in trichloromethylsilane atmosphere	25
PE/SnO_2	0.72	N/R	~0%@130°C	119	160	Binder assisted coating of SnO_2 onto PE	24
SiO_2-grafted PE	0.84	15	4%@120°C	N/R	N/R	3-Methacryloxypropyltrimethoxysilane and 1,8-bis(triethoxysilyl)octane react withUVO-treated PE separator	49
PE/$SiO_xC_yH_z$	0.36	12	10%@130°C	105	N/R	PE separator is treated with hexamethyldisiloxane/O_2/Ar plasma	50
PP/PPTA	0.90	30	~0%@200°C	N/R	35	Poly-p-phenylene terephthamide is polymerized and cast on Celgard PP	43
PP/PDA/SiO_2	0.55	N/R	22%@160°C	130	N/R	Celgard PP soaked in dopamine, then silane (GPTMS) solutions	26
PP/PVDF/metal oxide	1.69	35	18%@160°C	218	N/R	Celgard PP coated (doctor blade) with PVDF/metal oxide soln.	27
PE/PVDF/SiO_2	2.50	20	3%@170°C	380	11	Layered electrospun PVDF/PE/PVDF solution with SiO_2	35
PVDF/PMMA/SiO_2	4.00	30	~0%@150°C	406	33	Electrospun PVDF/PMMA/SiO_2 solutions are hot-pressed	34

HFP, hexafluoropropylene; PEGDMA, poly(ethylene glycol) dimethacrylate; PEEK, poly(ether ketone); PE, poly(ethylene); PP, poly(propylene); ALD, atomic layer deposition; PPTA, poly-p-phenyleneterephthamide; PDA, polydopamine; PVDF, poly(vinylidene fluoride); PMMA, poly(methyl methacrylate); TrFE, trifluoroethylene; PAN, polyacrylonitrile; MaLi2, maleic acid; P(MMA-ANEA), poly(methylmethacrylate-acrylonitrile-ethyl acrylate); EMITFSI, Lithium bis(trifluoromethanesulfonyl)imide/N-ethyl-N-methyl-imidazolium bis(trifluoromethanesulfonyl)imide; POSS, silsesquioxane; PVA, poly(vinylacetate), PU, Polyurethane; PI, polyimide.

[a]~0 = 'no visible shrinkage'. [b]N/R = 'not reported'.

Table 1. Continued

PVDF-TrFE/Al_2O_3	5.80	N/R	N/R	320	3	Polymer and Al_2O_3 electrospun together in methyl ethyl ketone	13
PVDF-HFP	0.81	N/R	3%@160℃	75	33	Electrophoretic deposition to bond separator and graphite anode	12
PVDF-HFP	1.08	N/R	5%@150℃	188	16	Electrolyte-soaked polymer creates inter-particle chain structure	16
PVDF-HFP/PE	1.01	24	~0%@150℃	216	16	Hierarchical solvent liberation method	17
PVDF-HFP/PAN	1.73	70	~0%@150℃	420	19	Core-shell structure via co-axial electrospinning	14
PVDF-HFP/Cellulose	1.89	115	~0%@200℃	310	1	PVDF-HFP, cellulose acetate in NMP cast on glass, treated with LiOH	40
PVDF-HFP/PE-*alt*-$MALi_2$	1.90	50	N/R	110	N/R	PE-*alt*-$MALi_2$ embedded in PVDF-HFP with phase inversion	46
PVDF-HFP/SiO_2	1.26	30	5%@160℃	420	14	Colloidal PVDF-HFP/SiO_2 suspension cast on a metal plate	33
PVDF-HFP/Al_2O_3	1.24	42	~0%@200℃	240	N/R	Al_2O_3 deposited with ALD on electrospun PVDF-HFP	36
PVDF-HFP/Al_2O_3	3.27	N/R	~0%@150℃	115	23	Instantly Reformed Gel with Direct Post-Solidation	19
PVDF-HFP/Al_2O_3	0.05	40	4% @150 ℃	372	18	Phase inversion PVDF solution mixed with Al_2O_3 solution	4
PVDF-HFP/LLZO	0.74	25	~0%@160℃	251	18	Post-solidation of LLZO incorporated in PVDF-HFP gel	44
PE/P(MMA-AN-EA) /SiO_2/Al_2O_3/EMITFSI	3.20	N/R	N/R	N/R	160	Emulsion polymerization of MMA:AN:EA(4:2:1). Polymer and metal oxides in DMF are cast (doctor blade) on PE Celgard for phase inversion	39

HFP, hexafluoropropylene; PEGDMA, poly(ethylene glycol) dimethacrylate; PEEK, poly(ether ketone); PE, poly(ethylene); PP, poly(propylene); ALD, atomic layer deposition; PPTA, poly-p-phenyleneterephthamide; PDA, polydopamine; PVDF, poly(vinylidene fluoride); PMMA, poly(methyl methacrylate); TrFE, trifluoroethylene; PAN, polyacrylonitrile; MaLi2, maleic acid; P(MMA-ANEA), poly(methylmethacrylate-acrylonitrile-ethyl acrylate); EMITFSI, Lithium bis(trifluoromethanesulfonyl)imide/N-ethyl-N-methyl-imidazolium bis(trifluoromethanesulfonyl)imide; POSS, silsesquioxane; PVA, poly(vinylacetate), PU, Polyurethane; PI, polyimide.

[a]~0 = 'no visible shrinkage'. [b]N/R = 'not reported'.

Table 1. Continued

P(MMA-POSS)	**3.41**	**220**	**N/R**	**275**	**N/R**	**Phase conversion: polymer + vinyl-trimethoxysilane/nonwoven**	**18**
PEEK/PMMA	1.03	41	~0%@150°C	173	70	Chloromethylated PEEK and PMMA tri-layer electrospun and pressed	51
Tissue paper/Al_2O_3	1.64	48	~0%@130°C	N/R	5	Al_2O_3 spray-coated on tissue paper	37
PVA/SiO_2	1.81	25	~0%@170°C	405	11	Electrospinning of PVA and tetraethyl orthosilicate solution	29
PU/Graphene oxide	3.73	100	~0%@170°C	733	3	Polyurethane and graphene oxide in THF/DMF are electrospun	41
Cellulose/glass fiber	1.14	20	~0%@200°C	N/R	N/R	3-step filtration: layered fibrous cellulose/glass/cellulose	22
Cross-linked PEGDMA	3.00	100	N/R	N/R	N/R	PEGDMA, vinylsulfonic acid sodium salt, diethyl allylphosphate in UV	52
Fluorinated PI	1.50	35	N/R	620	32	FPI made with polycondensation, cross-linking	15

HFP, hexafluoropropylene; PEGDMA, poly(ethylene glycol) dimethacrylate; PEEK, poly(ether ketone); PE, poly(ethylene); PP, poly(propylene); ALD, atomic layer deposition; PPTA, poly-p-phenyleneterephthamide; PDA, polydopamine; PVDF, poly(vinylidene fluoride); PMMA, poly(methyl methacrylate); TrFE, trifluoroethylene; PAN, polyacrylonitrile; MaLi2, maleic acid; P(MMA-ANEA), poly(methylmethacrylate-acrylonitrile-ethyl acrylate); EMITFSI, Lithium bis(trifluoromethanesulfonyl)imide/N-ethyl-N-methyl-imidazolium bis(trifluoromethanesulfonyl)imide; POSS, silsesquioxane; PVA, poly(vinylacetate), PU, Polyurethane; PI, polyimide.

[a]~0 = 'no visible shrinkage'. [b]N/R = 'not reported'.

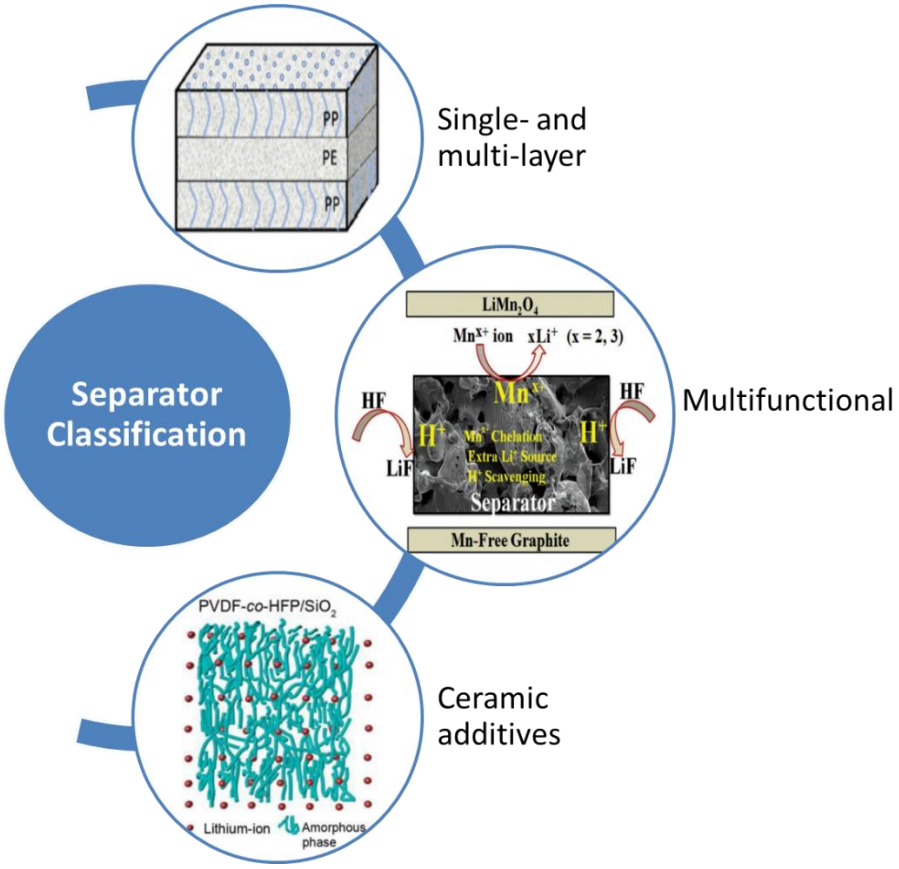

Figure 1. Separator classification. Single- and multi-layer cartoon reprinted from [53], copyright 2015, with permission from Elsevier; ceramic additives schematic reprinted from [33], copyright 2018, with permission from WILEY; multifunctional schematic reprinted from [46], copyright 2016, with permission from WILEY.

Discussion

Single- and multi-layer separators

Because thick separators (>50 μm) decrease the areal power density, most commercial batteries have employed thin (<25 μm) polyolefin monolayer microporous separators, whose characteristics are good mechanical strength, excellent chemical stability, low cost, and advantageous thermal shutdown properties [11]. Mechanically and electrochemically stable polymers, such as fluorinated or aromatic polymers, have also been considered, as explained below [7]. Among other polymers, Poly(Vinylidene Fluoride) (PVDF) and its copolymers possess high polarity, low degree of crystallinity, high dielectric constant, good chemical stability, and good

electrolyte wettability owing to the presence of C–F group [5,7]. Han *et al.* [12] directly deposited a layer of PVDF-HFP (hexafluoropropylene) separator on a graphite anode through electrophoretic deposition in a surfactant-free colloidal system, resulting in a separator with high thermal stability (3% shrinkage at 160 °C for 5 h) and high mechanical strength (33 MPa). Although Poly(vinylidene fluoride-co-trifluoroethylene) has been rarely used in Li-ion batteries, its semi-crystalline and non-reactive nature, flexibility, thermal stability, and piezoelectric properties, make it a promising candidate [13]. Electrospun core–shell fiber structure combining PVDF-HFP (for electrolyte stability) and PAN (for thermal and mechanical stability) resulted in a highly porous structure and excellent electrochemical properties, but with only 19 MPa for tensile strength [14]; whereas electrospun fluorinated polyimide separator has shown robust mechanical properties (~32 MPa stress at break) after cross-linking with thermal annealing at 300 °C [15].

PVDF-HFP separators can be improved with an inter-particle chain structure [16]. First, the polymer is partially dissolved in acetone, cast on a substrate, and dried. Then, through an electrolyte soaking and drying procedure, both undissolved polymer particles and polymer chains rearrange toward a higher-density structure, and the particles are no longer visible. The prepared separator has a highly porous and polar structure, with 188 wt% electrolyte uptake. The interactions between solvents and non-solvents influence the formation of pores and phase transformation process [17,18], leading to different morphologies, such as sponge-like or finger-like with an asymmetric distribution of pores [5]. With a similar concept, a separator can be prepared with two different solvents, such as N-methyl pyrrolidone (NMP) and acetone. The variation in solvent evaporation rate creates a hierarchical structure with high porosity, leading to enhanced ionic conductivity (Fig. 2). The authors attribute a near-zero capacity fading at 10C after 1000 cycles to the increased Li^+ transport channels due to the inter-island structure [17,19].

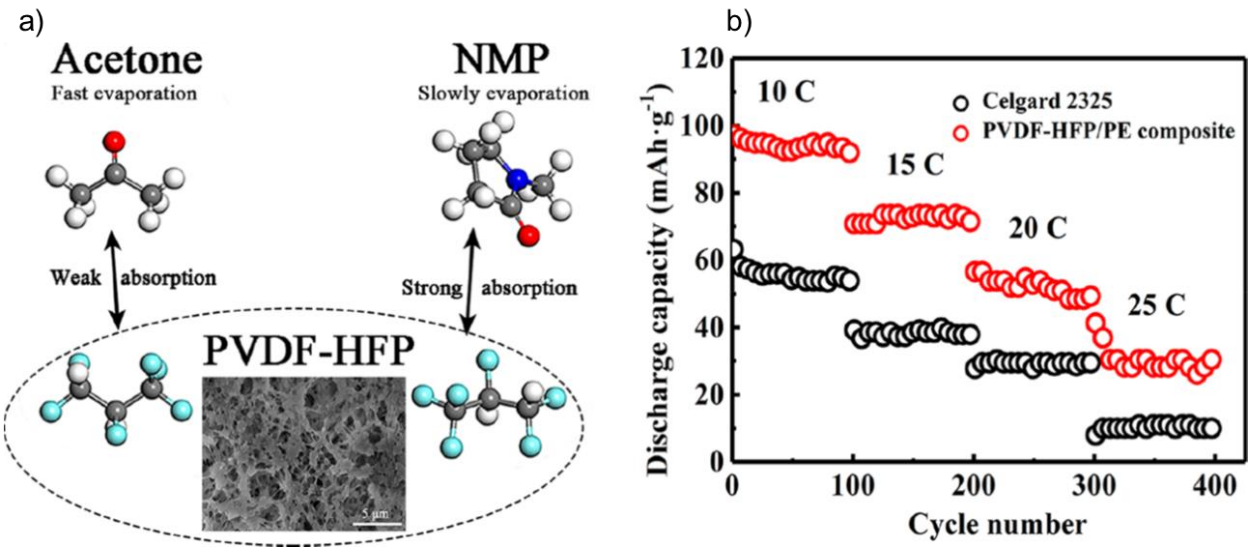

Figure 2. Illustration and SEM image (a) and rate-capability measurements (b) of PVDF-HFP/PE separator enabled by dual-solvent hierarchical gas liberation. Reprinted with permission from [17], copyright 2018, ACS.

Dual-layer Poly(Ethylene)/Poly(Propylene) (PE/PP) and tri-layer (PP/PE/PP) separators are advantageous to address safety issues that may arise from single-layer separators. A multilayer PE/PP separator made via a combination of multilayer co-extrusion and thermally induced phase separation shows high thermal stability with shutdown capability at wide temperature window [20]. Its highly porous structure provides enhanced electrolyte uptake and ionic conductivity. Similar to multilayer co-extrusion, a template method by use of $CaCO_3$ can create a PE–PP multilayer separator with an adjustable thermal shutdown capability, with high thermal stability at 160 °C [21]. A tri-layer structure of PP/PE/PP microporous membranes provides unique puncture strength (at least 300 g mil^{-1}), and the low-melting PE layer acts as a thermal fuse, while the higher-melting PP layers provide physical integrity above PE melting point [11,20]. To obtain a more homogenous distribution of current and fast migration of Li-ions between electrodes, other materials may be used in the layers, such as cellulose nanofibers and glass microfibers, which combine a nanoporous and a microporous structure [22]. The high and uniform porosity enhances

electrolyte uptake and improves the electrochemical performance, while a thermal annealing at 200 °C for 30 min increases the thermal stability.

Ceramics and other composite separators

Ceramic coatings on the separator or the positive electrode has had some advantages in preventing internal short circuits due to metal particle penetration [23]. Electronic insulating metal oxides, such as SiO_2, Al_2O_3 SnO_2 [24], or silicone [25] can be included within the separator through sol-gel method [26], in situ deposition, film casting [27], or physical vapor deposition [28] on one or both sides of a polyolefin separator. The thin (as low as 2 μm) coating provides reduced shrinkage of the separator at shutdown temperatures, better cycling (in terms of C-rate capacities and cycle capabilities [6,26,27]), and improved electrolyte wetting because of the inorganic oxide ceramic phase [26,27,29]. The addition of hydrophobic-silica aerogel to a PP separator, for example, creates a highly porous structure, high affinity to liquid electrolytes, and provides a thermal insulation capability [30]. Additional thin ceramic layers on anodes can lower the risk of local particle penetration and of thermal runaway [31].

Complex coatings are becoming common. For example, it is reported [23] that the Sumitomo separator used by Panasonic and Tesla Motors involves a coating with ceramic particles as well as an aromatic polyamide to increase the penetration strength. Improved coatings should not impede ion flux, but improve penetration strength or combine chemically with lithium dendrites [32]. PVDF-HFP/SiO_2 separator prepared in acetone, in a unique way without using a surfactant, exhibits high thermal stability (4.5% shrinkage 160 °C for 1 h), good mechanical strength (14 MPa), enhanced ionic conductivity (1.2 mS cm^{-1}), and long cycle performance [33]. The authors claim that the improvement in Li^+ transport efficiency indicates that the electrolyte is also absorbed by the SiO_2 nanoparticles, which decrease the polymer crystalline phase (Fig. 3).

The combination of ceramic nanoparticles with nanofibers creates a unique environment with excellent properties. Poly(vinyl alcohol)/SiO_2 membranes fabricated through sol-gel electrospinning are simple but effective separators [29], whereas a more complex electrospun PVDF/PMMA/SiO_2 separator [34] has excellent mechanical (tensile strength ~33 MPa) and cycling properties (capacity retention 91% at 0.2C after varying-rate capability measurements). Electrospinning can create ultrathin and strong porous PVDF/PE/PVDF tri-layer separators [35], and the addition of silica nanoparticles results in an electrolyte uptake of 380 wt%, and an ionic conductivity of 2.5 mS cm^{-1}. The sandwich-like structure delivers superior discharge capacity even at high current densities. Nanoparticles may also be deposited through atomic layer deposition (ALD) [36]. The resulting separator shows a 0% shrinkage at 200 °C and robust fire retardant capability, without compromising the cell performance. Paper-based separators are an interesting alternative to polyolefin membranes for more economically viable separators [37].

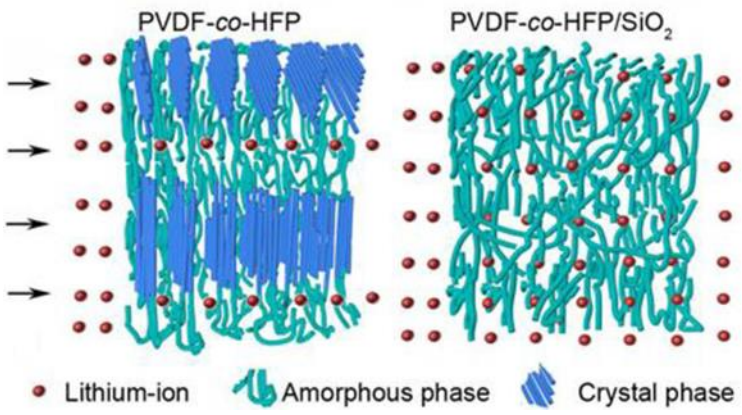

Figure 3. Illustration of the difference in the amorphous and crystal phases of PVDF-co-HFP (a) and PVDF-co-HFP/SiO_2 (b) separators. Reprinted from [33], copyright 2018, with permission from WILEY.

Ionic liquid (IL) electrolytes are a safer alternative to existing organic electrolytes. A good compatibility between IL electrolytes and separator materials would increase the separator wettability, which is the current major drawback with these electrolytes [38]. A poly(methyl

methacrylate-acrylonitrile-ethyl acrylate) (P(MMA–AN–EA))-coated Celgard 2400 was investigated in Lithium bis(trifluoromethanesulfonyl)imide/N-ethyl-N-methyl-imidazolium bis(trifluoromethanesulfonyl)imide (EMITFSI) IL electrolyte [39]. When equal parts of SiO_2 and Al_2O_3 are added to the separator, the improved bond strength of Si–O/Al–O cross-section points and the polymer network results in excellent thermal and mechanical stabilities. The authors report that chemical interactions between metal oxide nanoparticles and electrolyte provide a high ionic conductivity (3.2 mS cm^{-1}), and high oxidation potential (5.7 V).

Organic materials, such as cellulose, are also used as fillers in polymers for the fabrication of composite separators due to increased ionic conductivity, electrolyte uptake, electrochemical performances, and abundance of raw material in nature [40]. Sometimes the use of inorganic materials as additives with polymers results in a non-uniform dispersion. Various particle surface modification techniques have been reported to solve this problem but the solutions are costly and time-consuming. Graphene oxide (GO) has high dispersion in polymer matrices due to its polar groups, and GO-modified polyurethane separators show high electrolyte uptake (733 wt%), high ionic conductivity (3.7 mS cm^{-1}), and superior thermal stability (up to 300 °C) as compared to metal oxides fillers [41]. Urethanes and fluorinated polymers, when modified with charged functional groups, may potentially be used as matrices for solid electrolytes. Scientists have recently focused on decoupling ionic conductivity from polymer segment relaxation to explore new ion transport mechanisms for solid electrolytes [1,40]. The fibrillar units of poly-p-phenylene terephthalamide or LLZTO have been used to generate various migration routes for Li-ions between electrodes [42,43]. LLZTO, in particular, suppresses lithium dendrites growth by forming a highly ductile quasi-solid composite separator [44].

Multifunctional separators

Traditionally, battery separators are chemically and electrochemically inert. However, a new conceptual framework for Li-ion battery design proposes that separators should actively participate in the cell chemistry, to enhance performance and enable additional features. Multifunctional chemically active separators may, for example, trap transition metal cations, such as Mn, attract acid species, or dispense Li ions, with significant battery performance benefits [9,45,46]. Keeping the surface of the graphite negative electrode free from Mn impurities during the cell formation cycles is essential for the creation of a SEI with superior properties (maximally ionically conducting, while electronically insulating) that enables an improved capacity retention and prolonged cell life [46].

Banerjee *et al.* [47] reported a separator made with PVDF-HFP matrix and a modified cross-linked styrene-divinylbenzene copolymer functionalized with disodium iminodiacetate groups. $LiMn_2O_4$/Graphite cells with the aforementioned separator showed no capacity loss at 55 °C cycling even after saturation of the separator with Mn ions. The thin uniform SEI provides a uniform current distribution and reduced losses of Li^+ ions, and the resulting smaller interfacial resistances increase the capacity utilization and improve the power performance of Li-ion batteries [48]. The same group [46] embedded a poly(ethylene-*alternate*-maleic acid) (PE-*alt*-$MALi_2$) into a PVDF-HFP matrix with a phase inversion procedure. The separator not only (1) traps dissolved Mn ions (proved by elemental analysis on separator after use), but it also (2) scavenges hydrogen fluoride (FTIR showed a protonation of the Li carboxylate groups of the functional polymer due to HF), and (3) it's a source of sacrificial Li^+ ions. Multifunctional separators offer new possibilities to the incorporation of ceramics into Li-ion battery separators. SiO_2-chemically grafted on a PE separator improves the adhesion strength, thermal stability (<5% shrinkage at 120

°C for 30 min) and electrolyte wettability as compared to the physical SiO_2-coating on PE separator [49]. A surface-grafting method overcomes the issues of coating and improves the performances of conventionally polyolefin separators, but this technique is expensive and requires special equipment. Qin *et al.* [50] proposed a binder-free technique with reactive atmospheric pressure plasma containing Ar/O_2/hexamethyldisiloxane to functionalize a PE separator with a thin layer of $SiO_xC_yH_z$. The resulting polar functional groups on the PE substrate improve the wettability, electrolyte uptake, and ionic conductivity.

While an increase in performance is always desirable, multifunctional separators can also add new features, like anti-shrinkage properties or flame-retardancy [50,51]. Amino functionalized poly(ether ketone) (PEEK) with anti-shrinkage property and thermal stability was used in the outer layers of a tri-layer separator, while PMMA was the intermediate layer [51]. The electrospun PEEK/PMMA/PEEK separator has high thermal stability (0% shrinkage at 150 °C), and high thermal shutdown window (100-270 °C). Cross-linked monofunctional sulfonate and phosphate species incorporated in a multifunctional oligomer separator introduce flame-retardancy feature (Fig. 4) and improve Li-ion transport properties [52].

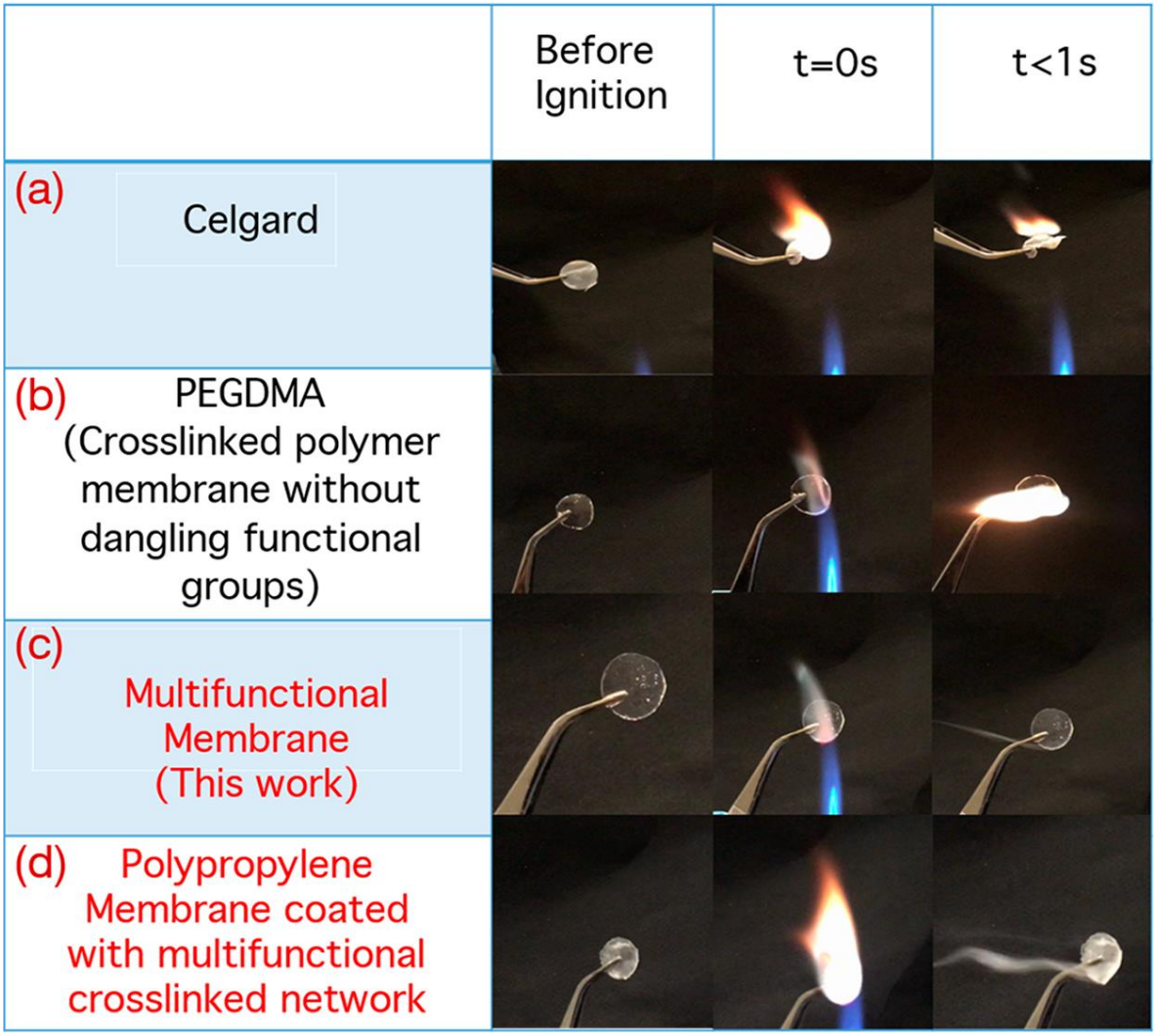

Figure 4. Flame retardant properties of electrolyte-imbibed multifunctional membranes compared to commercial separator: (a) Celgard, (b) cross-linked Polyethylene glycol dimethacrylate (PEGDMA), (c) multifunctional membrane, and (d) multifunctional membrane as a coating on the commercial separator. Reprinted with permission from [52], copyright 2018, ACS.

Conclusions

The separator has an active role in the cell because of its influence on energy and power densities, safety and cycle life. In this review, we highlighted new trends and requirements of state-of-art Li-ion battery separators. In single- and multi-layer polyolefin or PVDF-based separators, the combination of different polymer layers, the use of fluorinated polymers, the two-miscible-solvents and the solvent/non-solvent techniques are all beneficial to increase the properties and

performance of the separator. The addition of ceramic additives increases thermal and mechanical properties, but the traditional incorporation techniques do not provide additional functionality. Multifunctional separators, instead, offer a new range of possibilities when functional groups are incorporated in the separator, which is now chemically active and provides additional features in terms of safety and performance. Research needs to take into consideration both the market and safety needs. By nano-engineering the material network in a multifunctional separator, we would be able to create preferred pathways for ion transport in 3D structures that maximize both the Li ions motion and safety, and reduce degradation.

References

[1] Liu J., Bao Z., Cui Y., Dufek E., Goodenough J.B., Khalifah P., Li Q., Liaw B.Y., Liu P., Manthiram A., Meng S.Y., Subramanian V.R., Toney M.F., Viswanathan V.V., Whittingham S.M., Xiao J., Xu W., Yang J., Yang X. Q., Zhang J.G., "Pathways for practical high-energy long-cycling lithium metal batteries", *Nature Energy*, vol. 4, no. 3. pp. 180–186, 2019.

[2] Zeng X., Li M., Abd El-Hady D., Alshitari W., Al-Bogami A.S., Lu J., Amine K., "Commercialization of Lithium Battery Technologies for Electric Vehicles", *Advanced Energy Materials*, vol. 9, no. 27. Wiley-VCH Verlag, p. 1900161, 2019.

[3] Lagadec M. F., Zahn R., Wood V., "Characterization and performance evaluation of lithium-ion battery separators", *Nat. Energy*, vol. 4, no. 1, pp. 16–25, 2019.

[4] Ali S., Tan C., Waqas M., Lv W., Wei Z., Wu S., Boateng B., Liu J., Ahmed J., Xiong J., Goodenough J.B., He W., "Highly Efficient PVDF-HFP/Colloidal Alumina Composite Separator for High-Temperature Lithium-Ion Batteries", *Adv. Mater. Interfaces*, vol. 5, no. 5, pp. 1–10, 2018.

[5] Waqas M., Ali S., Feng C., Chen D., Han J., He W., "Recent Development in Separators for High-Temperature Lithium-Ion Batteries", *Small*, vol. 15, no. 33, 2019.

[6] Costa C.M., Lee Y.H., Kim J.H., Lee S.Y., Lanceros-Méndez S., "Recent advances on separator membranes for lithium-ion battery applications: From porous membranes to solid electrolytes", *Energy Storage Mater.*, vol. 22, no. July, pp. 346–375, 2019.

[7] Barbosa J.C., Dias J.P., Lanceros-Méndez S., Costa C.M., "Recent advances in poly(Vinylidene fluoride) and its copolymers for lithium-ion battery separators", *Membranes (Basel).*, vol. 8, no. 3, 2018.

[8] Yuan M., Liu K., “Rational design on separators and liquid electrolytes for safer lithium-ion batteries”, *J. Energy Chem.*, vol. 43, pp. 58–70, 2020.

[9] Banerjee A., Ziv B., Shilina Y., Ziegelbauer J.M., Liu H., Harris K.J., Botton G., Goward G.R., Luski S., Aurbach D., Halalay I.C., “Review—Multifunctional Separators: A Promising Approach for Improving the Durability and Performance of Li-Ion Batteries”, *J. Electrochem. Soc.*, vol. 166, no. 3, pp. A5369–A5377, 2019.

[10] Eller J., Ebner M., Burns C., Dahn J., Wood V., “Quantifying Inhomogeneity of Lithium Ion Battery Electrodes and Its Influence on Electrochemical Performance”, *J. Electrochem. Soc.*, vol. 165, no. 2, pp. 339–344, 2018.

[11] Heidari A.A., Mahdavi H., “Recent Development of Polyolefin-Based Microporous Separators for Li−Ion Batteries: A Review”, *Chem. Rec.*, pp. 1–27, 2019.

[12] Han Y., Ye L., Boateng B., Sun Q., Zhen C., Chen N., Shi X., Dickerson J.H., Li X., He W., “Direct electrophoretic deposition of an ultra-strong separator on an anode in a surfactant-free colloidal system for lithium ion batteries”, *J. Mater. Chem. A*, vol. 7, no. 4, pp. 1410–1417, 2019.

[13] Bicy K., Suriyakumar S., Anu Paul P., Anu A.S., Kalarikkal N., Stephen A.M., Geethamma V.G., Rouxel D., Thomas S., “Highly lithium ion conductive, Al_2O_3 decorated electrospun P(VDF-TrFE) membranes for lithium ion battery separators”, *New J. Chem.*, vol. 42, no. 24, pp. 19505–19520, 2018.

[14] Yang S., Ma W., Wang A., Gu J., Yin Y., “A core-shell structured polyacrylonitrile@poly(vinylidene fluoride-hexafluoro propylene) microfiber complex membrane as a separator by co-axial electrospinning”, *RSC Adv.*, vol. 8, no. 41, pp. 23390–23396, 2018.

[15] Kong L., Yan Y., Qiu Z., Zhou Z., Hu J., "Robust fluorinated polyimide nanofibers membrane for high-performance lithium-ion batteries", *J. Memb. Sci.*, vol. 549, pp. 321–331, 2018.

[16] Ye L., "An Efficient Route to Polymeric Electrolyte Membranes with Interparticle Chain Microstructure Toward High-Temperature Lithium-Ion Batteries", *Adv. Mater. Interfaces*, vol. 4, no. 11, pp. 1–6, 2017.

[17] Luo R., Wang C., Zhang Z., Lv W., Wei Z., Zhang Y., Luo X., He W., "Three-Dimensional Nanoporous Polyethylene-Reinforced PVDF-HFP Separator Enabled by Dual-Solvent Hierarchical Gas Liberation for Ultrahigh-Rate Lithium Ion Batteries", *ACS Appl. Energy Mater.*, vol. 1, no. 3, pp. 921–927, 2018.

[18] Liu B., Huang Y., Zhao L., Huang Y., Song A., Lin Y., Wang M., Li X., Cao H., "A novel non-woven fabric supported gel polymer electrolyte based on poly(methylmethacrylate-polyhedral oligomeric silsesquioxane) by phase inversion method for lithium ion batteries", *J. Memb. Sci.*, vol. 564, pp. 62–72, 2018.

[19] Liu J., Shi X., Boateng B., Han Y., Chen D., He W., "A Highly Stable Separator from an Instantly Reformed Gel with Direct Post-Solidation for Long-Cycle High-Rate Lithium-Ion Batteries", *ChemSusChem*, vol. 12, no. 4, pp. 908–914, 2019.

[20] Li Y., Pu H., "Facile fabrication of multilayer separators for lithium-ion battery via multilayer coextrusion and thermal induced phase separation", *J. Power Sources*, vol. 384, pp. 408–416, Apr. 2018.

[21] Li Y., Pu H., Wei Y., "Polypropylene/polyethylene multilayer separators with enhanced thermal stability for lithium-ion battery via multilayer coextrusion", *Electrochim. Acta*, vol. 264, pp. 140–149, Feb. 2018.

[22] Pan R., Sun R., Wang Z., Lindh J., Edström K., Strømme M., Nyholm L., "Sandwich-structured nano/micro fiber-based separators for lithium metal batteries", *Nano Energy*, vol. 55, pp. 316–326, Jan. 2019.

[23] Blomgren G.E., "The Development and Future of Lithium Ion Batteries", *J. Electrochem. Soc.*, vol. 164, no. 1, pp. A5019–A5025, 2017.

[24] Xiang Y., Zhu W., Qiu W., Guo W., Lei J., Liu D., Qu D., Xie Z., Tang H., Li J., "SnO2 Functionalized Polyethylene Separator with Enhanced Thermal Stability for High Performance Lithium Ion Battery", *ChemistrySelect*, vol. 3, no. 3, pp. 911–916, 2018.

[25] Gao H., Chen Y., Sun H., Zhao A., Wang L., Liu N., "Silicone modified polypropylene separator for high temperature lithium ion battery applications", *Mater. Res. Express*, vol. 5, no. 6, 2018.

[26] Chao C.Y., Chen Y., Sun H., Zhao A., Wang L., Liu N., "Enhanced wettability and thermal stability of polypropylene separators by organic–inorganic coating layer for lithium-ion batteries", *J. Appl. Polym. Sci.*, vol. 135, no. 28, pp. 1–7, 2018.

[27] Shekarian E., Nasr J., Mohammadi M. R., Bakhtiari T., Javanbakht O., "Enhanced Wettability and Electrolyte Uptake of Coated Commercial Polypropylene Separators with Inorganic Nanopowders for Application in Lithium-ion Battery", *J Nanostruct*, vol. 9, no. 4, pp. 736–750, 2019.

[28] Herle G., "Ceramic coating on battery separators", US Patent No. 10,193,116 B2, Washington, DC: U.S. Patent and Trademark Office. 2019.

[29] Chen S., Zhang Z., Li L., Yuan W., "Covalently-Bonded Poly(vinyl alcohol)-Silica Composite Nanofiber Separator with Enhanced Wettability and Thermal Stability for Lithium-Ion Battery", *ChemistrySelect*, vol. 3, no. 47, pp. 13365–13371, 2018.

[30] Feng G., Li Z., Mi L., Zheng J., Feng X., Chen W., "Polypropylene/hydrophobic-silica-aerogel-composite separator induced enhanced safety and low polarization for lithium-ion batteries", *J. Power Sources*, vol. 376, pp. 177–183, Feb. 2018.

[31] Kwade A., Haselrieder W., Leithoff R., Modlinger A., Dietrich F., Droeder K., "Current status and challenges for automotive battery production technologies", *Nat. Energy*, vol. 3, no. 4, pp. 290–300, 2018.

[32] Li M., Lu J., Chen Z., Amine K., "30 Years of Lithium-Ion Batteries", *Adv. Mater.*, vol. 30, no. 33, pp. 1–24, 2018.

[33] Boateng B., Zhu G., Lv W., Chen D., Feng C., Waqas M., Ali S., Wen K., He W., "An Efficient, Scalable Route to Robust PVDF-co-HFP/SiO2 Separator for Long-Cycle Lithium Ion Batteries", *Phys. Status Solidi - Rapid Res. Lett.*, vol. 12, no. 10, pp. 2–7, 2018.

[34] Fu Q., Lin G., Chen X., Yu Z., Yang R., Li M., Zeng X., Chen J., "Mechanically Reinforced PVdF/PMMA/SiO2 Composite Membrane and Its Electrochemical Properties as a Separator in Lithium-Ion Batteries", *Energy Technol.*, vol. 6, no. 1, pp. 144–152, Jan. 2018.

[35] Pan J.L., Zhang Z., Zhang H., Zhu P.P., Wei J.C., Cai J.X., Yu J., Koratkar N., Yang Z.Y., "Ultrathin and Strong Electrospun Porous Fiber Separator", *ACS Appl. Energy Mater.*, vol. 1, no. 9, pp. 4794–4803, 2018.

[36] Shen X., Li C., Shi C., Yang C., Deng L., Zhang W., Peng L., Dai J., Wu D., Zhang P., Zhao J., "Core-shell structured ceramic nonwoven separators by atomic layer deposition for safe lithium-ion batteries", *Appl. Surf. Sci.*, vol. 441, pp. 165–173, May 2018.

[37] Wang Z., Xiang H., Wang L., Xia R., Nie S., Chen C., Wang H., "A paper-supported inorganic composite separator for high-safety lithium-ion batteries", *J. Memb. Sci.*, vol. 553, pp. 10–16, May 2018.

[38] Francis C.F.J., Kyratzis I.L., Best A.S., “Lithium-Ion Battery Separators for Ionic-Liquid Electrolytes: A Review”, *Adv. Mater.*, vol. 1904205, pp. 1–22, 2020.

[39] Li M., Liao Y., Liu Q., Xu J., Sun P., Shi H., Li W., “Application of the imidazolium ionic liquid based nano-particle decorated gel polymer electrolyte for high safety lithium ion battery”, *Electrochim. Acta*, vol. 284, pp. 188–201, Sep. 2018.

[40] Asghar M.R., Zhang Y., Wu A., Yan X., Shen S., Ke C., Zhang J., “Preparation of microporous Cellulose/Poly(vinylidene fluoride-hexafluoropropylene) membrane for lithium ion batteries by phase inversion method”, *J. Power Sources*, vol. 379, pp. 197–205, 2018.

[41] Liu X., Song K., Lu C., Huang Y., Duan X., Li S., Ding Y., “Electrospun PU@GO separators for advanced lithium ion batteries”, *J. Memb. Sci.*, vol. 555, pp. 1–6, Jun. 2018.

[42] Wang Y., Sokolov A.P., “Design of superionic polymer electrolytes”, *Current Opinion in Chemical Engineering*,Volume 7, Pages 113-119, 2015.

[43] He L., Qiu T., Xie C., Tuo X., “A phase separation method toward PPTA–polypropylene nanocomposite separator for safe lithium ion batteries”, *J. Appl. Polym. Sci.*, vol. 135, no. 39, pp. 1–9, 2018.

[44] Shi X., Sun Q., Boateng B., Niu Y., Han Y., Lv W., He W., “A quasi-solid composite separator with high ductility for safe and high-performance lithium-ion batteries”, *Journal of Power Sources*

Volume 414, Pages 225-232, 2019.

[45] Banerjee A., Shilina Y., Ziv B., Ziegelbauer J.M., Luski S., Aurbach D., Halalay I.C., “Review—Multifunctional Materials for Enhanced Li-Ion Batteries Durability: A Brief Review of Practical Options”, *Journal of The Electrochemical Society*, 164 (1) A6315-A6323 (2017).

[46] Banerjee A., Ziv B., Shilina Y., Luski S., Halalay I.C., Aurbach D., "Multifunctional Manganese Ions Trapping and Hydrofluoric Acid Scavenging Separator for Lithium Ion Batteries Based on Poly(ethylene-*alternate*-maleic acid) Dilithium Salt", *Adv. Energy Mater*., 2017, 7, 1601556.

[47] Banerjee A., Ziv B., Luski S., Aurbach D., Halalay I.C., "The Effectiveness of Multifunctional Li-Ion Battery Separators past Their Saturation with Transition Metal Ions", *J. Electrochem. Soc.*, vol. 165, no. 10, pp. A2096–A2101, 2018.

[48] Liu H., Banerjee A., Ziv B., Harris K.J., Pieczonka N.P.W., Luski S., Botton G.A., Goward G.R., Aurbach D., Halalay I.C., "Elucidating the Li-Ion Battery Performance Benefits Enabled by Multifunctional Separators", *ACS Appl. Energy Mater.*, vol. 1, no. 5, pp. 1878–1882, May 2018.

[49] Na W., Koh K.H., Lee A.S., Cho S., Ok B., Hwang S.W., Lee J.H., Koo C.M., "Binder-less chemical grafting of SiO2 nanoparticles onto polyethylene separators for lithium-ion batteries", *J. Memb. Sci.*, vol. 573, pp. 621–627, Mar. 2019.

[50] Qin S., Wang M., Wang C., Jin Y., Yuan N., Wu Z., Zhang J., "Binder-Free Nanoparticulate Coating of a Polyethylene Separator via a Reactive Atmospheric Pressure Plasma for Lithium-Ion Batteries with Improved Performances", *Adv. Mater. Interfaces*, vol. 5, no. 19, pp. 1–7, 2018.

[51] Li Z., Xiong Y., Sun S., Zhang L., Li S., Liu X., Xu Z., Xu S., "Tri-layer nonwoven membrane with shutdown property and high robustness as a high-safety lithium ion battery separator", *J. Memb. Sci.*, vol. 565, pp. 50–60, Nov. 2018.

[52] Stalin S., Choudhury S., Zhang K., Archer L.A., “Multifunctional Cross-Linked Polymeric Membranes for Safe, High-Performance Lithium Batteries”, *Chem. Mater.*, vol. 30, no. 6, pp. 2058–2066, 2018.

[53] Shi C., Zhang P., Huang S., He X., Yang P., Wu D., Sun D., Zhao J., “Functional separator consisted of polyimide nonwoven fabrics and polyethylene coating layer for lithium-ion batteries”, *Journal of Power Sources*, 298, 158e165, 2015.

CHAPTER 3: Fabrication and Characterization of Meltblown Poly(Vinylidene difluoride) Membranes

Abstract

The meltblowing process may be employed to produce high volume of nonwoven Poly(Vinylidene difluoride) (PVDF) mats with fine fibers that lead to small pores. Although significant research has been reported on electrospinning of PVDF, there are no studies reported on the formation and characterization of PVDF meltblown mats because of the technological barriers associated with meltblowing the polymer. We investigated the fundamental properties and characteristics of an experimental grade of melt-blowable PVDF (Kynar® resin RC 10,287, Arkema, Inc.) with the objective of elucidating the structure-property-process relationships of the melt-blown mats. We have produced high-quality meltblown PVDF mats with low solid-volume percent (as low as 22%), and an average fiber diameter varying from 2 to 6 μm. The electrochemical resistance and absorbance capacity (electrolyte uptake up to 200%) of meltblown PVDF make it suitable for battery separator applications. We show interactions of the meltblown PVDF with the electrolyte lead to a morphology change in the fibers and a 3% decrease in crystallinity. By using cutting-edge meltblowing technologies, meltblown PVDF could become the separator in next generation Li-ion batteries.

Introduction

Nonwoven mats are used in a broad range of applications, with medical, hygiene, automotive, wipes, filtration, geosynthetics and interlinings representing dominant markets [1]. Among the many processes to produce nonwovens, meltblowing is well-known for its high production of structures with fiber diameters as low as 1 μm or less (using emerging high- density

dies) [2,3]. Meltblown structures can be formed in several ways; today, there are two main processes (Fig. 1):

a) Reicofil system based on Exxon-type die geometries [4,5]

b) Biax FiberFilm die – The process is referred to as Biax, Multi-row or SpunBlown® [6,7]

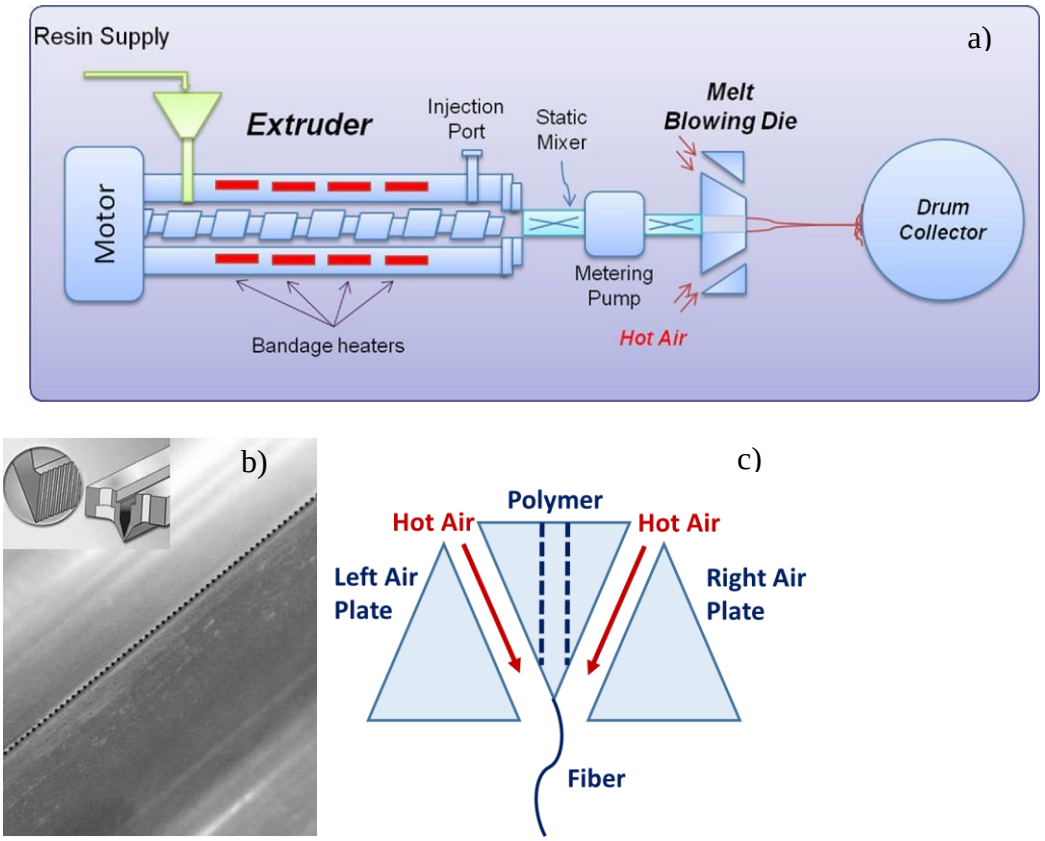

Figure 1. a) Schematic of the meltblowing process. Reprinted from ref. [2], Copyright 2013, with permission from Elsevier. b) Exxon type die with a bottom view of the spinneret, reprinted from ref. [8], Copyright 2016, with permission from Elsevier, and c) schematic of the die in a Reicofil meltblowing process.

The Reicofil die geometry is dominant and employed for the formation of microfibers for membranes used in the medical industry as barriers, as well as filtration media and other applications. In the Reicofil technology, an extruder feeds a molten polymer to a melt-pump that precisely delivers the polymer to a row of fine orifices. As the polymer exits the orifices, two converging, high-velocity streams of heated air [8] impinge on the molten filaments. The diameter

of the extruded filaments is attenuated by the air flow and fine fibers are formed. After the polymer threads are stretched by hot air, the resulting fibers are expanded into room temperature air. Due to the mixture of high-speed hot air and fibers with ambient air, fiber bundles move forward and backward (whipping). These movements stretch the filaments due to so-called “form drag”. This form drag appears with every change in fiber direction, leading to a variability in the fiber diameter, and it is the most significant cause behind roping where one or more filaments are entangled, touch and form large fibers.

Generally, fiber-diameter attenuation is achieved by three different forces: aerodynamic drag near the die, aerodynamic drag near the collector, and fiber elongation due to fiber vibration movements along the spin line; however, most attenuation occurs near the die, as reported by Bresee *et al*. [9] In the meltblowing process, the fibers are collected on a moving collector (conveyor belt or drum). As the fibers exit the orifices and approach the collector surface, they slow down, go through bending instability, touch one another and form a bond at the contact points since they are not fully solidified.

Filaments produced by the meltblowing process have generally low chain orientation. In addition, the fibers do not often crystallize until reaching the collector. The processing conditions influencing the final properties of the meltblown fibers and webs include: melt temperature, throughput, die geometry, air flowrate and temperature, die-to-collector-distance (DCD) and collector speed. By varying any of these parameters, the final properties of the fibers, such as the cross-sectional shape, diameter, morphology, and web structure can be changed. The process requires extremely low melt viscosities to form fine fibers. The die is the most critical part of this technology [10].

The fiber size for a given melt flow-rate (MFR, defined as the mass of polymer that flows in 10 minutes in a capillary with specific size, pressure, and temperature [11]) depends on the mass flow rate through the capillaries and speed of air impinging on the fibers. In general, lower throughput rates or higher MFR, barrel temperatures, and air velocities yield finer fibers. However, each polymer possesses a unique natural draw ratio, a physical quantity directly related to the extensional viscosity and creep behavior of the polymeric materials. In general, the natural draw ratio limits fiber attenuation to a maximum value that determines the final fiber size after the local whipping and further local stretching due to the various drag forces. The limitation of the natural draw ratio implies that in order to achieve ultrafine fibers (< 1 µm), the throughput must be further reduced. To ensure that there is continuous flow in the capillaries would require a further decrease in the size of the capillaries and that, in turn, may require a low-melt viscosity. Current commercial systems use a capillary size of 300 to 500 µm while new high-density dies have smaller capillaries (180 to 250 µm).

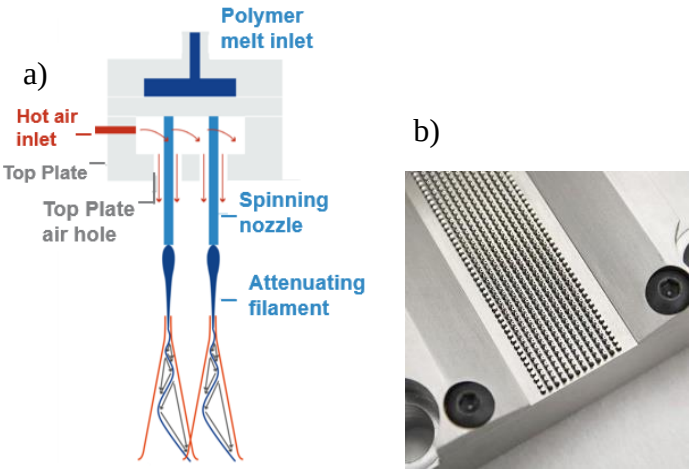

Figure 2. Schematic (a) and photograph (b) of the die in a Biax meltblowing process. Reprinted from ref. [8], Copyright 2016, with permission from Elsevier **.**

The Biax process uses multiple rows of orifices with co-centric air stream where each fiber is enveloped by a co-centric air supply. The multiple rows are essential for high productivity

despite a capillary density lower than Reicofil (Fig. 2), which is potentially beneficial in terms of fiber formation and the evolution of the morphology in the fiber structure. However, the nozzles can not be too closely packed and therefore, to compensate for the fewer capillaries in a row, the die uses multiple rows and can far exceed the throughput of the Reicofil system when four or more rows are used. This may be advantageous to reduce the probablity of fiber entanglement since the fibers are further apart.

Meltblowing produces mats with randomly oriented and small-diameter (1-5 μm) fibers. These features favor filtration applications [2,12,13]. The high specific surface area of the mats results in high filtration efficiency for particles from gas or liquid streams. On the other hand, to produce finer fibers, only polymers that have a reasonably low melt viscosity can be meltblown.[2,14] The material properties and the process variables are the parameters that affect the formation of meltblown fibers. Viscosity, MFR, elasticity and molecular weight belong to the former, while die and air temperature, air flowrate, polymer throughput, and die-to-collector distance (DCD) belong to the latter. The limiting factor is, however, the pressure in the die. This becomes a bottleneck for high-viscosity polymers that are not appropriate for meltblowing. One way to overcome this problem is to increase the number of capillaries, or their diameters, or decrease the molecular weight of the polymer to decrease viscosity.

The future of meltblowing resides in nanofiber materials, which are considered vital for the next generation of hi-tech nonwovens [3,10,12,13,15]. One process commonly cited in the academic literature for producing nanofibers is electrospinning, which uses electrostatic force to draw charged threads of polymer solutions to make nonwovens [16]. Melt processing, however, has significant advantages over electrospinning, such as high processing speeds and solvent-free operation. Meltblowing also has the potential to fabricate unique structures, blends, and

composites unobtainable by electrospinning. If meltblowing could be used to produce materials in the nanofiber range, it would provide a faster, easier, and less costly alternative to the electrospinning technique [17,18]. In particular, with the meltblowing process, it is possible to obtain desired structures in a much more controlled way, *e.g.* specific mat thickness, fiber diameter distribution, solidity, etc. [3].

Poly(Vinylidene difluoride) (PVDF) is a thermoplastic fluoropolymer produced by polymerization of vinylidene difluoride and is used in applications requiring high purity, such as batteries and sensors, as well as resistance to solvents and acids [15,19–21]. This is due to inherent PVDF properties, such as chemical and electrochemical resistance (including resistance to acids, oxidizing agents, solvents such as hydrocarbons, alcohols, alkyl and aromatic ethers, and aqueous salt), fire retardancy, higher melt temperatures than the more common polyolefins and polyesters, allowing for its use in high temperature applications, piezoelectricity and pyroelectricity [22–24]. Although significant research has been reported on the electrospinning of PVDF and use of the resulting (often post-treated) nonwoven mats as a separator in Li-ion batteries [25–31] and filtration media [32–34], there are no peer-reviewed publications on the formation and use of PVDF mats made by meltblowing. The technological barriers associated with meltblowing PVDF at reasonable processing temperatures include an inadequate melt flow rate, which cannot be overcome by increasing the temperature due to thermal decomposition and possible generation of hydrogen fluoride [35]. Extensive research has been done to synthesize branched polyolefins, such as polyethylene (PE) or polypropylene (PP), with a combination of low-shear viscosity (at low-molecular weight) and high-extensional viscosity (melt strength) ideal for meltblowing [36-40]. On the other hand, PVDF with low-molecular weight, which is necessary for a high-melt flowrate, has low-melt strength [41,42]; in contrast, high-molecular weight PVDF would require

temperatures close to its degradation to increase melt flowrate for melt-blowing. To overcome this problem, Hedhli *et al.* [41,43] showed specific chain-transfer agents added during polymerization increases the extensional viscosity in low-molecular weight PVDF but the resulting (unprocessed) polymer is strain-hardened due to long-chain branching.

By means of specific chain-transfer agents in high levels during polymerization, melt-blowable PVDF has recently been developed (Kynar® resin RC 10,287, Arkema, Inc.) [44]. This particular PVDF has low-molecular weight (15 to 100 kDa) and melt viscosities less than 1 kilopoise (kP) at 230° C and 100 s^{-1} [45]. One use for the high melt flow PVDF is in the formation of very small diameters fibers, useful for meltblown nonwoven materials. These types of nonwoven structures are unobtainable with previous commercial PVDF because of the low-melt strength or low-extensional viscosity of the polymer.

In this work, we report the fabrication of meltblown PVDF mats with a lab-scale Biax meltblowing apparatus. A full characterization is reported, including fiber and membrane characteristics of the resulting webs. Process-structure-properties relationships are discussed.

Experimental

An experimental grade of Poly(Vinylidene difluoride) (PVDF) Kynar® resin RC 10,287 (Arkema, Inc.) was used in this work. The PVDF has low-molecular weight with melt viscosity of 0.2 kP at 100 s^{-1} and 230°C, and is synthesized using emulsion polymerization, with a total amount of initiator between 0.05 to 2.5 wt%, and with 0.1 to 0.2 wt% fluorinated emulsifying agent (surfactant). The weight average molecular weight is between 15 and 100 kDa with a 2.0 poly-dispersity index with no oligomers (<10 kDa) in the products [45]. One way to obtain a low molecular weight PVDF is by using a chain-transfer agent at high levels. Some useful chain-transfer agents are C2 to C18 hydrocarbons like ethane, propane, butane, etc. The amount of chain-

transfer agent is 0.2 to 10.0 wt%. Chain-transfer agents can be added all at once at the beginning of the reaction, in portions throughout the reaction, or continuously as the reaction progresses, depending on the desired properties of the final products. The reaction is started and maintained by the addition of an initiator, such as an inorganic peroxide [45].

Thermal Analysis

We used Differential Scanning Calorimetry (DSC) and Thermal gravimetric Analysis (TGA) to determine the meltblowing temperature window (melting and degradation temperatures, respectively). The two techniques were both run in a nitrogen gas environment. DSC was also used to determine the PVDF crystallinity and interactions between PVDF and the electrolyte. The degree of crystallinity χ_c of PVDF is given by:

$$\chi_c = \frac{\Delta H_m}{\Delta H_m^*} \times 100 \qquad (1)$$

where ΔH_m is the measured melting enthalpy and ΔH_m^* = 104.5 J/g is the melting enthalpy of PVDF with χ_c=100% respectively [46].

Rheology

With steady and oscillatory shear experiments, we obtained viscosity curves using a TA DHR rheometer and an Instron CEAST, Smart Rheo 2000 – Dual Capillary Rheometer. Melt flow rate (MFR) was obtained with an Instron CEAST, 7026 Melt Flow Tester.

Meltblowing Process

PVDF Kynar® resin RC 10,287 was dried overnight at 70 ºC to avoid water vapor formation during meltblowing. We fabricated the webs using a Biax lab scale meltblowing set-up at the Nonwovens Institute at NC State University [47]. Polymer pellets were melted and pressurized using a single-screw extruder. The motor-driven screw transports the material through the extruder while three independently controlled heaters melt the polymer and maintain the desired

temperatures. The first heater is in the feed zone, where the polymer pellets are preheated at 180 ºC before entering the transition zone, where the polymer is compressed and homogenized at 227 ºC (second heater). The third heater is in the metering zone, where the polymer is transported at maximum pressure in the forward direction and a breaker plate filters out the impurities. In this zone, the polymer reaches its final temperature, 250 ºC.

Once the melted polymer exits the extruder, it enters a melt pump that meters and delivers the polymer to the die assembly. The 12.5-cm long die had 12 row/744 hole capillaries of 230-□m diameter. The fibers were collected as a mat on a rotating drum collector. Webs from the collector were wound onto rolls.

Operating Conditions

The process variables controlled were air pressure (in psi), polymer throughput measured in g $hole^{-1}$ min^{-1} (ghm), and die-to-collector distance (DCD) in cm. Three values (low, medium, high) for each variable were chosen and a matrix of 27 samples was developed as a design of experiments (Table 1). The lowest throughput was split in 3 different values to obtain a web with no "shots" (large particles of polymer in the mat with diameter much greater than fiber diameter). The collector speed was kept at a value that resulted in a basis weight of 30 g m^{-2}. The mats were calendered with a Klieverick belt Calender at 6 bar and 155 ºC to consolidate fiber-fiber bonds and decrease mat thickness.

Table 1. Design of experiments for meltblowing PVDF (Numbers listed in italic correspond to sample number.

	Throughput (ghm)	**0.09**	**0.11**	**0.14**	**0.17**			**0.254**		
DCD (cm)	**Air pressure (psi)**	**8**	**11**	**14**	**8**	**11**	**14**	**8**	**11**	**14**
35		*1*	*2*	*3*	*4*	*5*	*6*	*7*	*8*	*9*
40		*10*	*11*	*12*	*13*	*14*	*15*	*16*	*17*	*18*
45		*19*	*20*	*21*	*22*	*23*	*24*	*25*	*26*	*27*

Microscopy

To examine the fiber morphology, we sputter coated the samples with a thin layer of gold and analyzed them with a scanning electron microscope (Phenom Desktop SEM). Images were taken at 1500-2000X under a 5 kV accelerating voltage. We measured fiber diameters using Fiji (ImageJ) software, by taking at least 100 measurements from 5 different areas in each sample. We used a JEOL JSM-7600F SEM outfitted with a cryogenic transfer system and stage at -180 ºC (maintained by liquid nitrogen) to assess electrolyte absorption in the fibers. We kept the temperature of the experiments constant at -180 ºC with liquid Nitrogen. Light microscopy images were collected using an Olympus BX-60 microscope in the transmission mode on samples before and after wetting with electrolyte.

Thickness and Solid Volume Percent

We used a Mitutoyo micrometer to measure mat thickness. Solid volume percent σ is calculated as:

$$\sigma = \left(\frac{W}{t\rho_{\text{fiber}}} \right) \times 100 \qquad (2)$$

where W is the basis weight of the mat in g cm^{-2}, t is the thickness in cm, and ρ_{fiber} is the density of the polymer in g cm^{-3}.

Tensile Strength

Tensile strength was measured with an Instron 3400 (Mid-Range) universal testing system. Samples were cut in strip of 2.5 cm x 15 cm and placed between the machine clamps. We set-up the experiments to run up to ~6.8 kPa (100 psi) or until sample rupture. Sample peak loads and strains at break are reported.

Capillary Flow Porosimetry

The inter-fiber spacing (pore) size were analyzed with a capillary flow porosimeter from Porous Materials Inc. (PMI, Ithaca NY). Each sample was imbibed with a highly-wetting liquid (Salwick®, PMI, Ithaca, NY, USA) with a known surface tension of 20.1 dynes/cm. No visible contact angle was detected, so we assumed a contact angle of 0º for calculating pore diameter by using the Young–Laplace equation [48]: $D = 4\gamma_{L/G}\cos\theta / p$, where p is the extrusion pressure in MPa, D is the pore diameter in mm, $\gamma_{L/G}$ is the surface tension of Salwick in N/mm, and θ is the contact angle of Salwick with the sample. This technique provides the pore diameter at the most constricted part of the pore, the bubble-point diameter (calculated from the pressure required to force the first air bubble out of the mat), as well as the pore diameter distribution.

Electrolyte Uptake

We measured electrolyte uptake to investigate a potential application of the meltblown PVDF as a Li-ion battery separator. We performed a preliminary experiment to assess wettability of the membrane by measuring the time for a mat to absorb a drop of electrolyte, and the time was

less than a second. We determined electrolyte uptake with Eq. (3) by weighing the separators before and after soaking for 10 min in a 1M $LiPF_6$ Ethylene Carbonate/Dimethyl Carbonate 1:1 wt% mixture.

$$\text{Electrolyte uptake} = \left(\frac{W_a - W_b}{W_b} \right) \times 100 \qquad (3)$$

where W_a and W_b are the weights of separator before and after soaking in the electrolyte.

Results and Discussion

Thermal and Rheological Properties

Through DSC and TGA measurements, we found a melting temperature of 172 ºC and an onset of degradation at 280 ºC (Fig. 1, Appendix B). This is surprising considering that common PVDF resins tend to have decomposition onset temperatures at or above 350 ºC [49,50].

We performed rheological experiments at temperatures between 200 and 260 ºC, *i.e.,* above the melting point and below the onset of thermal degradation. The results (Fig. 3) revealed that the polymer is indeed melt-processable with a steady-shear viscosity at 200 ºC close to PP Metocene™ MF650W (from LyondellBassell), known to be suitable for meltblowing [51]. The viscosity curves were obtained by combining the results from steady shear, oscillatory shear and capillary viscosity experiments (see Appendix B). We were able to superimpose the data from these three experiments after applying the necessary correction, *i.e.* Cox-Merz rule for oscillatory shear and Bagley and Rabinowitz corrections for capillary experiments. The melt flow rate was 1316 g/10 min at 230 ºC (ASTM standard temperature [52]). The significantly low viscosity and high extensional viscosity (melt strength) are keys to melt-blow this polymer. We set the temperature of the meltblowing setup at 250 ºC to obtain a low fiber diameter, while avoiding degradation.

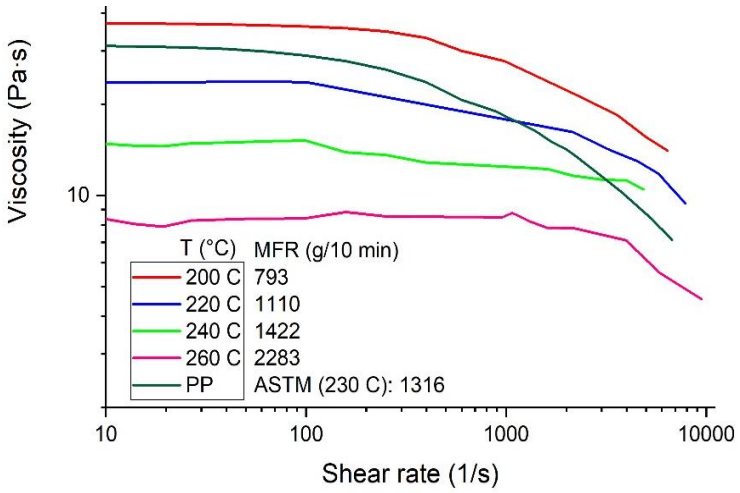

Figure 3. Rheological properties of Kynar® resin RC10,287 at different temperatures.

Polymer crystallinity is an important factor in membranes, *e.g.*, in battery separators a low crystallinity is desirable to facilitate the absorption and stability of liquid electrolyte [53,54]. The untreated polymer crystallinity was ~ 53%. However, the meltblowing process decreased the crystallinity to 48%, due to rapid re-crystallization of the fibers in the air stream, and introduced a new population of crystals in the crystalline part of the polymer, as shown by the appearance of a second smaller peak in the meltblown PVDF DSC results (Fig. 4a).

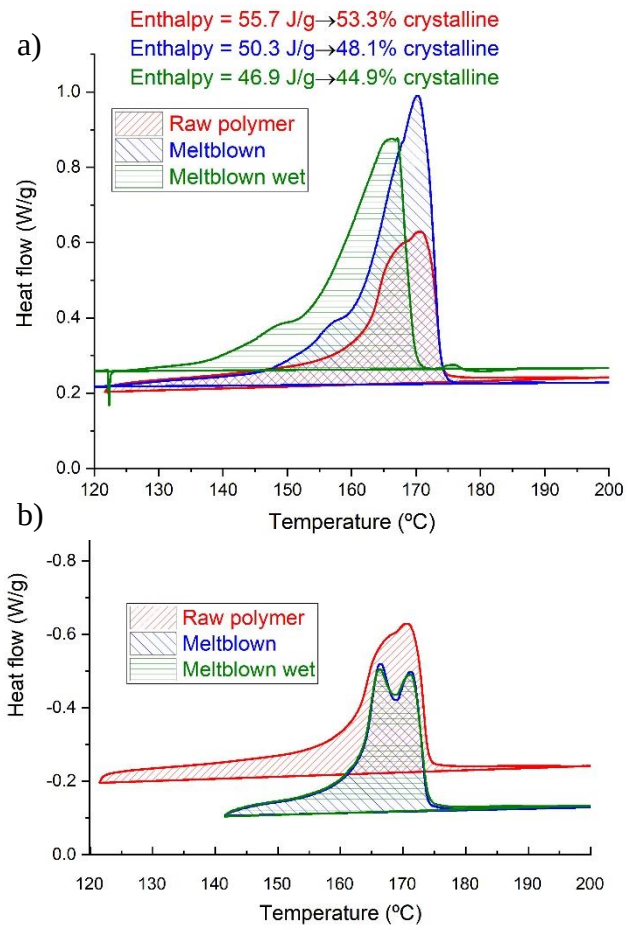

Figure 4. DSC first heat (a) and second heat (b) of Kynar® resin RC 10,287 raw, meltblown and meltblown after soaking in the electrolyte.

By inspection, we noticed a change in the structure and optical properties of the polymer after soaking in electrolyte (1M $LiPF_6$ EC/DMC). DSC was performed on meltblown PVDF after soaking in the electrolyte for nominally 15 minutes followed by overnight drying. The DSC results of the meltblown PVDF after soaking indicated a further decrease in crystallinity (~ 45%) and a change in the size of the two populations of crystals, noticeable by the shift of the peaks compared to the meltblown before soaking (Fig. 4a) [55,56]. This clearly shows interactions occurring between the electrolyte and the PVDF fibers, as discussed in the next paragraph. We presume that the new population of crystals is mostly present in the outer surface of the fibers, where the solvent was absorbed As seen in the second-heat curves (Fig. 4b), it is clear that the meltblowing process

introduced a second low-melting population of crystals. We speculate that the polymer shearing during meltblowing may have caused a phase separation. The second-heat DSC data from meltblown and electrolyte-imbibed meltblown mats are similar; hence, the polymer change in crystallinity and crystal size cause by the electrolyte are not permanent.

SEM and Fiber Diameter

Cryo-SEM on PVDF fibers imbibed with EC/DMC solvent (soaked for 24 h) revealed that the liquid interacts with the fibers, and a thin layer of frozen liquid around the surface of the fibers is indicative of these interactions (Fig. 5).

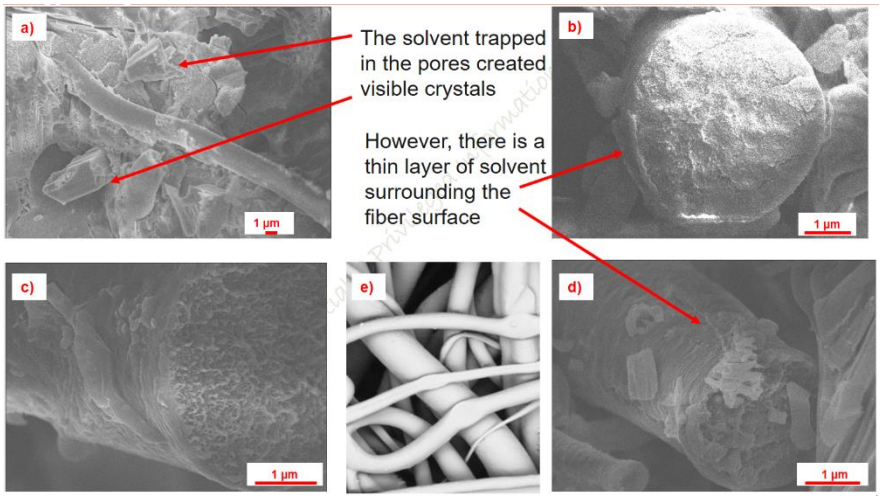

Figure 5. Cryo-SEM images of meltblown PVDF and EC/DMC at various locations (a), (b), (c), (d). Fiber mat before wetting with electrolyte (e).

The liquid diffuses in the amorphous domains of the outer surface of the fibers up to a certain penetration depth. We speculate that the original population of crystals is confined in the core of the fiber (similar to the raw polymer), where the liquid is not able to penetrate, while the outer surface is less crystalline, thus allowing liquid absorption. Figure 3 in appendix B shows TEM diffraction patterns of a fiber cross-section that support this hypothesis.

The electrolyte modifies the morphology of the fibers by forming a gel-like structure in the outer surface. The electrolyte-imbibed fiber mat has three regions, liquid in the pores, fibers solid-core and gel-like outer fiber surface. The liquid absorption makes the fibers swell and their diameter increases by 20-40% (not shown here). The entire mat quickly becomes (< 1 s) more homogeneous after adding electrolyte (Fig. 6). Even though there could be some evaporative loss of solvent trapped in the pores, the gel-like structure seems to be stable over time as assessed by visual examination of the electrolyte-imbibed mat.

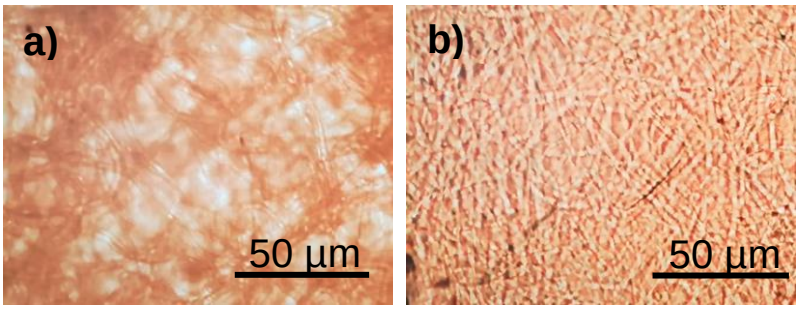

Figure 6. Optical images of meltblown PVDF mat before (a) and after (b) the addition of electrolyte.

Fig. 7 shows representative SEM images of the fiber mats and the fiber diameter distributions for few samples of the group. We were able to obtain fibers with no “shots”. The diameter distributions of meltblown fibers vary with process conditions. Low throughput and high air pressure (as in sample 3) produce mats with low fiber diameter and a narrow distribution. High throughput and low air pressure (as in sample 7), produce mats with high fiber diameter and a wide distribution.

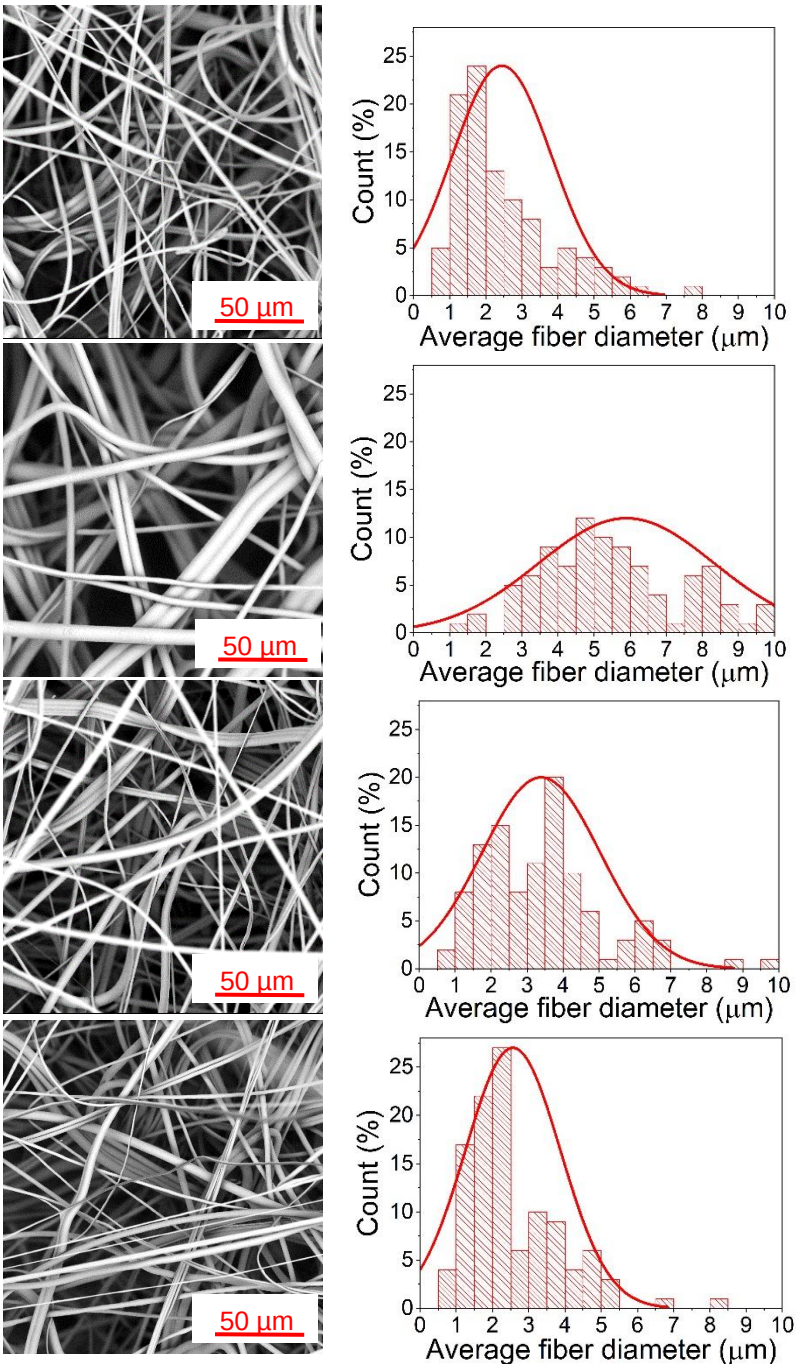

Figure 7. SEM and fiber diameter distributions of samples 3, 7, 14, and 21 according to Table 1.

By changing the die-to-collector distance (DCD), the mass flow rate of meltblown polymer (throughput), and the air pressure during the meltblowing process, as shown in Table 1, the average fiber diameter varied from 2 to 6 µm. In general, we observe that the fiber diameter decreases when

polymer throughput decreases or air pressure increases. This dependence mainly occurs because the drag force is higher than in the low air-pressure case, and the air is able to attenuate better the polymer filaments. Lowering the polymer mass flow rate decreases the fiber diameter because the same drag force from the air jet acts on a decreased polymer mass. In general, it is advised to balance the melt flow (pump pressure) with the air speed (air pressure). If the former is too high, the airflow is not able to attenuate well the polymer, if the latter is too high, the mat will present "shots". The DCD does not have a significant influence on fiber diameter. The collector position determines the point at which the fibers impact the belt. If the collector is close to the die, the fibers impact the belt while still molten filaments, hence creating a low quality mat. If the collector is far from the die, the fibers impact the belt after the crystallization; hence, they will not create strong fiber-fiber bonds. In particular, PVDF resins crystallize very quickly, thus further thermal calendaring should be used to increase the strength of the bonds.

The fiber diameter distribution can be controlled through the process parameters. Depending on the desired final application, we produce mats with a narrow distribution and low average fiber diameter or mats with a wider distribution. This is an important feature for membranes especially in filtration application.

Thickness, Solid Volume Percent, Pore Size, and Electrolyte Uptake

Fiber mats produced at low throughputs have a low fiber diameter that makes the fibers pack more closely. However, the solid volume percent must be low to enable efficient gas/ion transport for applications, but a low thickness is essential for membrane applications. The thickness was reduced from ~ 300 to ~ 65 μm by calendering the mats, which increases the solid volume percent.

It is challenging to measure the electrolyte uptake because of the nonwovens inherent capacity of holding liquid not just in their pores but also on the surface of the mat. To generate reproducible data, we took into account only the electrolyte that remains in the mat after pressing the separator in the cell. This is why the process of removing excess electrolyte from the mat surface is crucial.

High throughput samples show a low surface area and a low solid volume percent but can have varied electrolyte uptake, with a high DCD resulting in low electrolyte uptake. The solid volume percent at high throughput is not affected significantly by other variables (Fig. 8a). Figure 8b indicates approximately a linear relationship between electrolyte uptake and surface area (calculated from fiber diameter). At low throughput, a low air pressure gives high uptake, while at medium and high throughputs, a high air pressure is necessary to achieve a high electrolyte uptake. High throughput leads to high fiber diameter, low solid volume percent and low electrolyte uptake; this is in contrast with our expectations, suggesting that solvent-polymer interactions play an important role for the electrolyte uptake. Low/medium throughputs samples show the highest uptake and the highest surface area, with variable solid volume percent. If there were no uptake by the fibers, we would not find a dependence of surface are on electrolyte uptake seen in Fig. 8b. We may conclude fiber diameter (hence, surface area) has a more significant effect on electrolyte uptake than the solid volume percent because of the electrolyte absorbed in the gel-like region near the fiber surface.

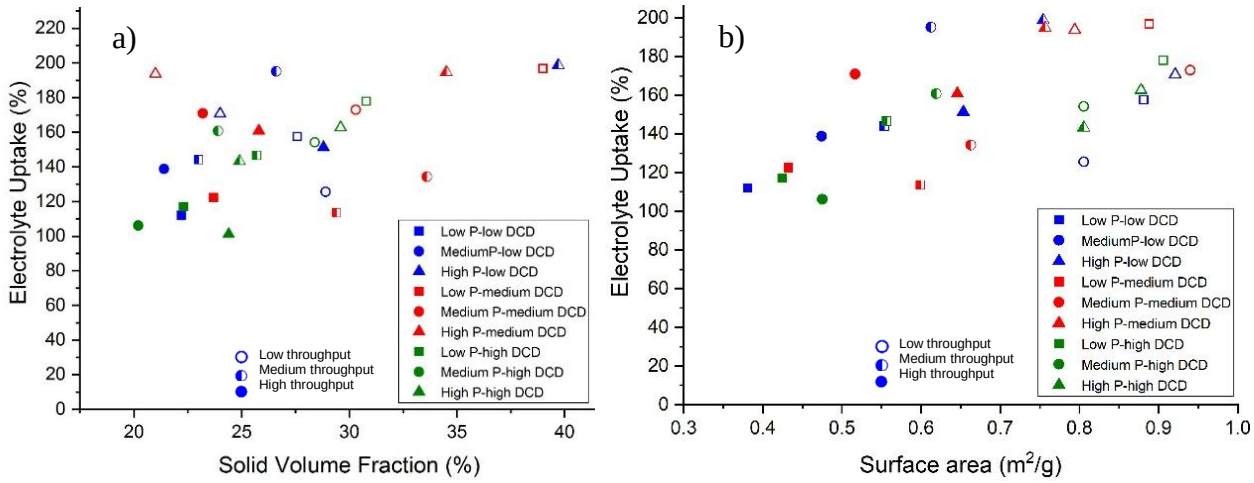

Figure 8. Electrolyte uptake vs solid volume percent (a) and vs surface area (b) at different process parameters.

Small fibers create small pores (Fig. 9), where the electrolyte is more easily held. However, in this case small fibers lead to a high solid volume percent, which could be detrimental for application as a separator for Li-ion batteries. On the other hand, small pores prevent micro-short circuits, which is a common problem in nonwoven battery separators.

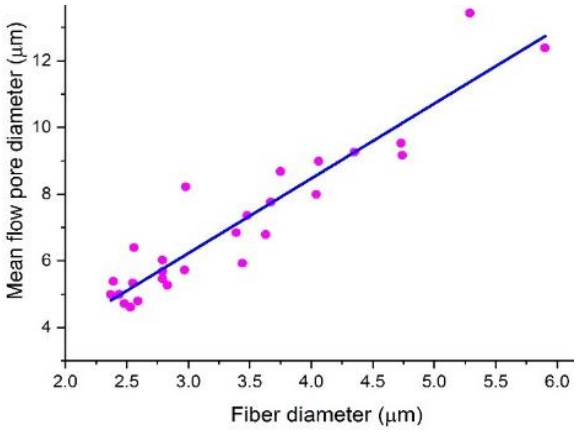

Figure 9. Pore size from porosimetry vs fiber diameter.

Table 1 in appendix B, shows the tensile properties of the mats. The cross-direction peak load is in general half of that in the machine direction, while the strain at break is similar for both

directions. The samples at 30 g m^{-2} showed similar results (~ 1.0-1.4 kPa in machine direction), while the sample at high basis weight has a high strength at break, as expected. The relatively low values for tensile strength can be attributed to the weak fiber bonding. One way to overcome this is to optimize the calendaring process to create more contact points between the fibers.

Conclusions

We have demonstrated the possibility to melt-blow PVDF Kynar® resin RC 10,287 to produce a high quality mat. By changing the die-to-collector distance, throughput, and air pressure, fibers with diameters as small as 400 nm were produced with an average diameter as low as 2 µm. We have highlighted some relationships between the process parameters (throughput, air pressure, die-to-collector distance) and the mat properties (fiber diameter, solid volume percent, electrolyte uptake). Samples made at low throughput and low air pressure give high uptake, while at medium and high throughputs a high air pressure is necessary to achieve a high electrolyte uptake. The fiber surface area plays an important role to design a high-absorbent mat. The interactions occurring between the electrolyte and the PVDF fibers lead to a high uptake with small fibers, despite the increase in solid volume percent. The pore size was approximately proportional to the fiber diameter. The latter and its distribution are controlled by the process parameters. The interactions with the electrolyte decreased the crystallinity of the polymer and produced a gel-like structure in the fiber outer layers, thus generating a tri-region system. These interactions could be beneficial for an increased ion conductivity due to the increased electrolyte, and because of an increased stability of the system.

Meltblown PVDF may be the basis for a successful nonwoven membrane in applications requiring good mechanical properties and resistance to chemical and thermal degradation, and the

meltblowing process has an advantage in comparison to electrospinning in terms of volume production and ease of manufacturing.

References

[1] Russell S.J., Textile Institute, "Handbook of Nonwovens", *Woodhead Publishing,* 2007.

[2] Hassan M.A., Yeom B.Y., Wilkie A., Pourdeyhimi B., Khan S.A., "Fabrication of nanofiber meltblown membranes and their filtration properties", *J. Memb. Sci.* 427, 336–344, 2013.

[3] Drabek J. , Zatloukal M., "Meltblown technology for production of polymeric microfibers/nanofibers: A review", *Physics of Fluids* vol. 31 2019.

[4] Harding J.W., Keller J.P.,Buntin R.R., "Melt-Blowing Die For Producing Nonwoven Mats", *US Patent No. 3825380A,* Washington, DC: U.S. Patent and Trademark Office,1974.

[5] Lohkamp D.T., Keller J.P. "Meltblowing die using capillary tubes", *US Patent No. 3825379A,* Washington, DC: U.S. Patent and Trademark Office, 1974.

[6] Schwarz E., "Apparatus and Process for Uniformly Melt-Blowing A Fiberforming Thermoplastic Polymer in a Spinnerette Assembly of Multiple Rows of Spinning Orifices", *US Patent No. 5476616A*, Washington, DC: U.S. Patent and Trademark Office, 1995.

[7] Biax Fiberfilm Corporation, Spun-blown®/Meltblown Systems, https://www.biax-fiberfilm.com/spunblown-systems (accessed 4/14/2020).

[8] Wente V.A., Boone E.L., and Fluharty C.D., "Manufacture of Superfine Organic Fibers" U.S. Department of Commerce, Office of Technical Services Report No. PBI 11437, 1954.

[9] Bresee R.R., Ko W.C. "Fiber Formation during Melt Blowing", *International Nonwovens Journal,* Volume: os-12 issue: 2, 2003.

[10] Yarin A.L., Pourdeyhimi B., Ramakrishna S., "Fundamentals and Applications of Micro- and Nanofibers", *Cambridge University Press,* 2014.

[11] ASTM D1238-13, Standard Test Method for Melt Flow Rates of Thermoplastics by Extrusion Plastometer, ASTM International, West Conshohocken, PA, 2013, www.astm.org

[12] Tan D.H., Zhou C., Ellison C.J., Kumar S., Macosko C.W., Bates F. S., "Meltblown fibers: Influence of viscosity and elasticity on diameter distribution", *Journal of Non-Newtonian Fluid Mechanics,* Vol. 165, 15–16, 892-900, 2010.

[13] Ellison C.J., Phatak A., Giles D.W., Macosko C.W., Bates F.S. ,"Melt blown nanofibers: Fiber diameter distributions and onset of fiber breakup", *Polymer,* Vol. 48, 11, 3306-3316, 2007.

[14] Batra S.K., Pourdeyhimi B., "Introduction to nonwovens technology", DEStech *Publications,* 2012.

[15] Chen S., Tao X., Zeng W., Yang B., Shang S., "Quantifying Energy Harvested from Contact-Mode Hybrid Nanogenerators with Cascaded Piezoelectric and Triboelectric Units" *Adv. Energy Mater.* 7, 1–9, 2017.

[16] Greiner A., Wendorff J. H., "Electrospinning: A Fascinating Method for the Preparation of Ultrathin Fibers", *Angew. Chemie Int. Ed.* 46, 5670–5703, 2007.

[17] Uppal R., Bhat G., Eash C., Akato K., "Meltblown Nanofiber Media for Enhanced Quality Factor", *Fibers Polym.* 14, 660–668, 2013.

[18] Balogh A., Farkas B., Faragó K., Farkas A., Wagner I., Van Assche I., Verreck G., Nagy Z. K., Marosi G., "Melt-Blown and Electrospun Drug-Loaded Polymer Fiber Mats for Dissolution Enhancement: A Comparative Study", *J. Pharm. Sci.* 104, 1767–1776, 2015.

[19] Dang Z.M., Yuan J.K., Yao S.H., Liao R.J., "Flexible nanodielectric materials with high permittivity for power energy storage", *Advanced Materials,*vol. 25 6334–6365, 2013.

[20] Chang C., Tran, V.H., Wang J., Fuh Y.K., Lin L., "Direct-write piezoelectric polymeric nanogenerator with high energy conversion efficiency", *Nano Lett.* 10, 726–731, 2010.

[21] Brochu P., Pei Q., “Advances in Dielectric Elastomers for Actuators and Artificial Muscles”, *Macromol. Rapid Commun.* 31, 10–36, 2010.

[22] Song J.Y., Wang Y. Y., Wan C.C., “Review of gel-type polymer electrolytes for lithium-ion batteries”, *J. Power Sources* 77, 183–197, 1999.

[23] Dang Z.M., Yuan J.K., Zha J.W., Zhou T., Li S.T., Hu G. H., “Fundamentals, processes and applications of high-permittivity polymer-matrix composites”, *Progress in Materials Science,* vol. 57, 660–723, 2012.

[24] Liu F., Hashim N.A., Liu Y., Abed M.R.M., Li, K., “Progress in the production and modification of PVDF membranes”, *J. Memb. Sci.* 375, 1–27, 2011.

[25] Gopalan A., Santosh P., Manesh K.M., Nho J.H., Kim S.H., Hwang C.G., Lee K.P., “Development of electrospun PVdF–PAN membrane-based polymer electrolytes for lithium batteries”, Journal of Membrane Science, Vol. 325, 2,683-690, 2008.

[26] Yanilmaz M., Chen C., Zhang X., “Fabrication and characterization of SiO_2/PVDF composite nanofiber-coated PP nonwoven separators for lithium-ion batteries”, *J. Polym. Sci. Part B Polym. Phys.* 51, 1719–1726, 2013.

[27] Gao K., Hu X., Dai C., Yi T., “Crystal structures of electrospun PVDF membranes and its separator application for rechargeable lithium metal cells”, *Mater. Sci. Eng. B Solid-State Mater. Adv. Technol.* 131, 100–105, 2006.

[28] Kim J. R., Choi S. W., Jo S. M., Lee W. S., Kim B.C., “Electrospun PVdF-based fibrous polymer electrolytes for lithium ion polymer batteries”, *Electrochim. Acta,* 50, 69–75, 2004.

[29] Choi S.S., Lee Y.S., Joo C.W., Lee S.G., Park J.K., Han,K. S., “Electrospun PVDF nanofiber web as polymer electrolyte or separator”, *Electrochimica Acta,* 50, 339–343, 2004.

[30] Choi S.W., Jo S. M., Lee W.S., Kim Y.R., “An electrospun poly(vinylidene fluoride) nanofibrous membrane and its battery applications”, *Adv. Mater.* 15, 2027–2032, 2003.

[31] Kimura N., Sakumoto T., Mori Y., Wei K., Kim B.S., Song K. H., Kim I. S., “Fabrication and characterization of reinforced electrospun poly(vinylidene fluoride-co-hexafluoropropylene) nanofiber membranes”, *Compos. Sci. Technol.,* 92, 120–125, 2014.

[32] Zhou W., Bahi A., Li Y., Yang H., Ko F., “Ultra-filtration membranes based on electrospun poly(vinylidene fluoride) (PVDF) fibrous composite membrane scaffolds”, *RSC Adv.,* 3, 11614–11620, 2013.

[33] Agyemang F.O., Li F., Momade F.W.Y., Kim H., “Effect of poly(ethylene oxide) and water on electrospun poly(vinylidene fluoride) nanofibers with enhanced mechanical properties as pre-filter for oil-in-water filtration”, *Mater. Chem. Phys.,* 182, 208–218, 2016.

[34] Hou D., Lin D., Ding C., Wang D., Wang J. ,“Fabrication and characterization of electrospun superhydrophobic PVDF-HFP/SiNPs hybrid membrane for membrane distillation”, *Sep. Purif. Technol.,* 189, 82–89, 2017.

[35] Ebnesajjad S., Khaladkar P.R., “Fluoropolymer Applications in the Chemical Processing Industries”, second edition, *William Andrew,* 2017.

[36] Qiu W., Sworen J., Pyda M., Nowak-Pyda E., Habenschuss A., Wagener K.B., Wunderlich B., “Effect of the Precise Branching of Polyethylene at Each 21st CH2 Group on Its Phase Transitions, Crystal Structure, and Morphology”, *Macromolecules*, 39, 1, 204–217, 2006.

[37] Santangelo P.G., Roland C.M., Puskas J.E., “Rheology of Star-Branched Polyisobutylene”, *Macromolecules,* 32, 6, 1972–1977, 1999.

[38] Shroff R.N., Mavridis H., “Long-Chain-Branching Index for Essentially Linear Polyethylenes”, *Macromolecules,* 32, 25, 8454–8464, 1999.

[39] Lee J.H., Archer L.A., “Stress Relaxation of Star/Linear Polymer Blends”, *Macromolecules*, 35, 17, 6687–6696, 2002.

[40] Graebling D., “Synthesis of Branched Polypropylene by a Reactive Extrusion Process”, *Macromolecules*, 35, 12, 4602–4610, 2002.

[41. Hedhli L., Mekhilef N., Moyses S., Lewis R.H., “Characterization of Randomly Branched Poly(vinylidene fluoride)”, *Macromolecules*, 41, 2011-2021, 2008.

[42] Ebnesajjad S., “Introduction to Fluoropolymers”, second edition, *William Andrew*, 2013.

[43] Hedhli L., Mekhilef N., “Branched fluoropolymers”, *Intern. Patent Appl. WO2007061488A3*, 2006.

[44] Henry J.J., Goldbach J., Stabler S., Devisme S., Chauveau, J., “Advancements in the production of meltblown fibres”, *Filtr. Sep.*, 53, 36–40, 2016.

[45] Goldbach J.T., Henry, J.J., Stabler S.M., Chauveau J., “High melt flow fluoropolymer composition”, *US Patent Application No. 20170088989(A1)*, Washington, DC: U.S. Patent and Trademark Office, 2017.

[46] Nakagawa K., Ishida Y. “Annealing effects in poly(vinylidene fluoride) as revealed by specific volume measurements, differential scanning calorimetry, and electron microscopy”, *J. Polym. Sci. Part A-2 Polym. Phys.*, 11, 2153–2171, 1973.

[47] Lab Scale Equipment – The Nonwovens Institute, https://thenonwovensinstitute.com/capabilities-and-facilities/lab-scale-equipment/ (accessed 4/14/2020).

[48] Jena A., Gupta, K., “Liquid Extrusion Techniques for Pore Structure Evaluation of Nonwovens”, *International Nonwovens Journal*, Vol: os-12 issue: 3, 2003.

[49] Ouyang Z.W., Chen E.C., Wu, T.M., “Thermal stability and magnetic properties of polyvinylidene fluoride/magnetite nanocomposites”, *Materials (Basel)*, 8, 4553–4564, 2015.

50. Li H., Kim H., “Thermal degradation and kinetic analysis of PVDF/modified MMT nanocomposite membranes”, *Desalination*, 234, 9–15, 2008.

[51] Metocene MF650W| LyondellBasell, https://www.lyondellbasell.com/en/polymers/p/Metocene-MF650W/067cded2-a7be-48ef-80c3-ea44287e4ff0 (accessed 4/14/2020).

[52] ASTM D1238-13. “Standard test method for melt flow rates of thermoplastics by extrusion plastometer”, *Annual book of ASTM standards*, 269–281, 2004.

[53] Cao J.H., Zhu B.K., Xu, Y.Y.,“Structure and ionic conductivity of porous polymer electrolytes based on PVDF-HFP copolymer membranes”, *J. Memb. Sci.*, 281, 446–453, 2006.

[54] Li H., Chen. Y.M., Ma X.T., Shi J.L., Zhu B.K., Zhu L.P., “Gel polymer electrolytes based on active PVDF separator for lithium ion battery. I: Preparation and property of PVDF/poly(dimethylsiloxane) blending membrane”, *J. Memb. Sci.*, 379, 397–402, 2011.

[55] Wunderlich, B., “Macromolecular Physics”, *Academic Press: New York*, Vol. 3, Crystal Melting, 1980.

[56] Yamada K., Hikosaka M., Toda A., Yamazaki S., Tagashira K., “Equilibrium Melting Temperature of Isotactic Polypropylene with High Tacticity: 1. Determination by Differential Scanning Calorimetry”, *Macromolecules*, 36, 4790-4801, 2003.

CHAPTER 4: Meltblown PVDF as A Li-Ion Battery Separator

Abstract

Among types of Li-ion battery separators, nonwoven mats have the advantage of low production cost, low mass, and high porosity. Nonwoven polyvinylidene difluoride (PVDF) shows promising results as a separator because of its chemical and mechanical stability and affinity for electrolytes commonly employed in Li-ion cells. We investigated the use of a melt-blowable PVDF (Kynar® resin RC 10,287, Arkema, Inc.) to produce meltblown PVDF mats, with the objective of elucidating their performance as a separator in Li-ion batteries. High-quality meltblown PVDF mats were produced with a 1.2-m wide Reicofil R4 meltblown pilot line at the Nonwovens Institute and subsequently consolidated through thermal compaction in a hydraulic press. The resulting mats showed high homogeneity (low roping and fiber entanglements), an average pore size as small as 0.9 μm, and fiber diameter as small as 1.4 μm, yielding high surface area and electrolyte uptake. After thermally compacting the nonwoven mat, the thickness and pore size decrease along with electrolyte absorbence and conductivity. The highest ionic conductivity of the electrolyte-infused mat was ~ 9.6 mS/cm (room temperature with 1M $LiPF_6$ in EC/DMC 1:1 v/v), and the first-cycle capacity of a Li/$LiCoO_2$ cell containing meltblown PVDF separators was 142 mAh/g. In this work, we report the physical, chemical, and electrochemical properties of meltblown PVDF relevant to its use as a Li-ion battery separator.

Introduction

While significant research has focused on negative and positive electrode materials in rechargeable Lithium-ion (Li-ion) batteries, battery separators have only recently received more consideration from the scientific community. Commercial separators are mainly polyolefins, such as polyethylene (PE) or polypropylene (PP). However, nonpolar polyolefins are hydrophobic with

low surface energy and exhibit poor affinity to polar organic electrolytes used in Li-ion cells, and surfactants are needed to obtain good electrolyte wettability [1]. Nonwoven separators possess fibrous structures that allow a high electrolyte uptake with good structural cohesion due to intertwined fibers within the mat. Nonetheless, nonwoven battery separators produced with common high-production processes have shown lower performances than microporous polyolefins separators, which may be attributed to inadequate pore structure [2]. Among other polymers, PVDF is a promising material for battery separators due to high polarity, low degree of crystallinity, high dielectric constant, good chemical stability, and good electrolyte wettability owing to the presence of C–F group [3–5]. An advantageous manner to produce nonwoven PVDF separators would employ a meltblowing process, which is a well-developed, high-volume production technology. To be melt-blowable, polymer resins must have high melt-flow rates, but commercial PVDF resins did not possess this property until recently [6–8]. Researchers have successfully electrospun PVDF from solution with the goal of exploring it as a nonwoven battery separator [9]. Electrospun PVDF has attracted the attention of the scientific community as a separator in Li-ion batteries [10–15] and filtration media [16–18]. Table 1 summarizes reports on the use of PVDF in battery separators, and these studies are expanded upon below. Unless otherwise specified, the electrolyte used was 1M LiPF6 in EC:DMC (1:1 w/w).

Electrospun PVDF was reported as early as in 2003 by Choi et al. [14], who found the nanofibrous polymer electrolyte consisted of a solid polymer phase with PVDF fibers partially swollen after electrolyte uptake. In this case, the electrolyte uptake was 260%, double that of commercial Celgard® membranes, and its ionic conductivity was 1.7 mS/cm at 20°C (vs. ~1 mS/cm for Celgard®). Kim et al. [13] prepared thermally stable electrospun PVDF with an average fiber diameter of 0.5-1.4 μm, and an apparent porosity and a mean pore size of 80-89% and 1.1-

4.3 µm, respectively. The resulting mats showed 350% electrolyte uptake (1M LiPF6-EC/DMC/DEC 1:1:1 by weight), 1 mS/cm ionic conductivity at room temperature, and stability in a Graphite/LiCoO2 cell at 60 °C. The mat's ionic conductivity and electrolyte uptake increased with a decrease in fiber diameter. Electrospun PVDF thermally-treated at 150-160°C showed increased mechanical properties (+44% Young's modulus, +179% tensile strength, +35% elongation at break vs. untreated mats), despite the small fiber diameters (100-800 nm) [12,19]. The increased crystallinity and fiber diameter after thermal treatment were reported to be the reason for the improved physical properties.

Table 1. Summary of remarkable literature results on non-woven PVDF as separator in Li-ion batteries.

Material	Ion Conductivity (mS/cm)	Porosity	AFD (nm)	Electrolyte uptake	Remarks	Ref.
Celgard®	1.0	40%	No fibers	130%	Made of PP - On the market now	This work
PVDF	1.0	80%	514	N/R	Thermal treatment → High mechanical properties	12
PVDF	1.0	80-89%	450-1038	320-360%	From high crystallinity → high thermal stability	13
PVDF	1.7	83%	250	260%	-	14
PVDF	N/D	N/R	336	1200%	Plasma pre-post-treatment	20
PVDF	2.0	N/R	100-800	73%	Thermal treatment → High mechanical properties	19
PVDF-HFP	0.4	59%	1000	210%	No improvements	21
PVDF-HFP	2.3	N/R	1000	750%	Activation with ionic liquid	22
TPP@PVDF-HFP	0.4	N/R	900	N/D	Flame-retardant properties	23
P(VDF-HFP)/PAN	6.5	80%	400	475%	Blend membrane of the 3 polymers	24
PVDF/PMMA	3.5	77%	1000	330%	High anodic stability	25
PVDF/TPU	3.2	86%	570	342%	High electrochemical stability	26
PVDF-LAGP/PEO	10.9	93%	2400	831%	In situ porosity generation	27

HFP, hexafluoropropylene; PP, poly(propylene); PVDF, poly(vinylidene fluoride); TPP, triphenyl phosphate; PMMA, poly(methyl methacrylate); PAN, polyacrylonitrile; TPU, Thermoplastic polyurethane; LAGP, lithium aluminum germanium phosphate; PEO, polyethylene oxide.
[a]N/R = 'not reported'.

Table 1. Continued

SiO_2/PVDF	2.6	N/R	N/R	370%	SiO_2 electrospraying and PVDF electrospinning	28
SiO_2/PVDF/PP	2.6	53-73%	312	237%	-	29
SiO_2/Al2O_3/PVDF	2.1	62%	3280	366%	Melt-electrospinning	30

HFP, hexafluoropropylene; PP, poly(propylene); PVDF, poly(vinylidene fluoride); TPP, triphenyl phosphate; PMMA, poly(methyl methacrylate); PAN, polyacrylonitrile; TPU, Thermoplastic polyurethane; LAGP, lithium aluminum germanium phosphate; PEO, polyethylene oxide.
[a]N/R = 'not reported'.

Safety of PVDF nonwoven battery separators may be improved by encapsulating a flame-retardant agent inside a protective PVDF-HFP (hexafluoropropylene) [23] or by introducing a thermoplastic resin in the mat with a thermal shutdown function [20]. In the second case, Choi *et al.* [20] introduced PE chains on an electrospun PVDF mat through an ethylene plasma treatment; it's among the earliest nonwoven separators to incorporate this kind of safety measure. An atmospheric-pressure plasma treatment improves the mat hydrophilicity, which strongly influences electrolyte uptake and overall safety of the cell [20]. Laurita *et al.* [19] performed a plasma treatment of a PVDF solution before electrospinning (the solution was plasma-exposed) and of the PVDF fiber web after electrospinning. Although the mechanical properties and electrolyte uptake significantly increased with the treatment (Young's modulus from 9 to 32 MPa, tensile strength from 1 to 5 MPa, elongation at break from 80% to 130%, and electrolyte uptake from 500% to 1200%), the unknown cost of such a process seems impracticable. PVDF possesses relatively high crystallinity, and many researchers believe that high crystallinity results in decreased ionic conductivity due to the reduced migration rate of lithium ions in the crystalline phase [31]. One effective method for lowering the crystallinity of nonwoven mats is to use suitable PVDF co-polymers, such as electrospun PVDF-HFP [21], or modified PVDF [22]. For example, Cheruvally *et al.* [22] imbibed PVDF-HFP mats with a room temperature ionic liquid. The ionic conductivity was 2.3 mS/cm, but the capacity loss was significant in a Li/$LiFePO_4$ cell at discharge rates higher than 1C.

Electrospun PVDF has poor mechanical properties. In order to improve these properties, researchers have focused on composites and blends of PVDF, such as adding polyolefin supports and/or matrices [32,33], adding ceramic or colloidal particles to the PVDF spinning solution [34–38], or electrospinning multiple polymers from the same solution [25]. Raghavan *et al.* [24] created

three-dimensional, layered-structured composite separators of electrospun PVDF-HFP and PAN (Polyacrylonitrile) with fiber diameters of ~400 nm and thicknesses from 25 to 50 μm depending on the separator's layers. These authors claim the electrolyte uptake of 470% and ionic conductivity of 6.5 mS/cm were due to high porosity (>80%). Li *et al.* [25] fabricated electrospun PVDF/PMMA with 23% crystallinity, 77% porosity and 330% electrolyte uptake for 1 M $LiClO_4$ in EC/PC (1:1, v/v). The resulting ionic conductivity was 3.5 mS/cm and the oxidative stability was 5.1 V. The addition of inorganic particles into polymer membranes may reduce their crystallinity and improve the migration of lithium ions [31]. Inorganic particles or organic-inorganic particles [39] may also improve wettability due to high polarity and increased surface area due to roughening [31]. PVDF-LAGP (lithium aluminum germanium phosphate) [27] modified with PEO (polyethylene oxide) shows high conductivity (10.9 mS/cm) and electrolyte uptake (831%), and cell-cycling stability.

Composites and blends are often necessary when using PVDF in a nonwoven battery separator. Multilayer composite separators showed improved conductivity and mechanical properties when a dispersion of PVDF and ceramic particles (300 nm Al_2O_3 or 7 nm SiO_2 nanoparticles) was electrospun on polyolefin nonwoven separators (PP and PE) [29,33]. Yanilmaz *et al.* [29] prepared a SiO_2/PVDF composite nanofiber-coated PP membrane by electrospinning SiO_2/PVDF dispersions onto both sides of PP nonwovens. The resulting structures showed high ionic conductivity (2.6 mS/cm) and improved mechanical properties (+322% Young's modulus, +77% tensile strength vs. freestanding nanofiber mat). With addition of 15% SiO_2 nanoparticles (7 nm), the fiber surface roughness increased significantly, and the electrolyte uptake increased from 226% to 291%. The increase in fiber surface roughness and decrease in fiber diameter lead to an increase in fiber surface area and electrolyte uptake, due to PVDF-electrolyte interactions, as

we have shown in a previous work [6]. Zhu *et al.* [40] reported that PVDF forms a thin porous gel layer when cast-coated onto PP/PE spunbond nonwoven separators and soaked in 1M $LiPF_6$ in EC/DMC/EMC 1/1/1 w/w/w, with a resulting surface pore size <100 nm and a conductivity of 0.3 mS/cm. Cells ($Li/LiFePO_4$) containing these PVDF-PP/PE separators showed lower voltage hysteresis between charge and discharge compared to Celgard® 2730, which the authors attribute to improved Li^+ transference number in the PVDF-PP/PE separators. Alcoutlabi *et al.* [41,42] prepared an electrospun PVDF-CTFE (chlorotrifluoroethylene) coated Celgard® membrane. As a matrix, they used either single-layer PP membranes or trilayer PP/PE/PP membranes. A novel nozzle-less electrospinning equipment produced fibers with 130-nm nominal diameter with good adhesion between the separator and the electrode. Lee *et al.* [43–45] prepared similar mats, but mixed PVDF-CTFE with PVDF-HFP, while Zhu *et al.* [46] used a polyethylene terephthalate-PVDF hybrid membrane to improve thermal and dimensional stability.

Recently, variations of electrospinning have been considered to either increase rate of production [47] or avoid the use of solvents [30]. In the first case, a novel tip-induced electrospinning process uses multiple tips that are mechanically dipped into and removed from the polymer solution to seed small liquid spikes on the solution surface. A strong electrical field initiates and extends liquid jets from the top of these spikes to deposit nanofibers on the collector [47]. In the second case, melt-electrospinning was used with a low-viscosity PVDF to create a separator with a solvent-free process [30]. A novel and relatively unexplored high-volume fabrication method of nonwoven PVDF battery separators is the scalable nanospinning of sheared solutions, which produces hierarchically structured polymeric microparticles having branched nanofiber coronas with a dendritic morphology [48–53].

Despite promising results, the simplicity, and ability of the process to produce functional nanofibers, electrospinning is inherently slow, expensive, and solvent intensive compared to meltblowing. Also, as noted earlier, electrospun PVDF is not mechanically strong enough to use as a battery separator, and it often requires a supporting matrix. In a previous work, we showed the feasibility of meltblowing PVDF, and we reported mat characteristics and interactions with common organic electrolytes [6]. However, there are no studies to our knowledge reported on the use of PVDF mats as battery separators produced by the meltblowing process because of the complexity of the equipment required and of technological barriers associated with processing PVDF: its melt flow rate is inadequate at low temperature, and high temperature is not possible because of the generation of hydrogen fluoride. Melt processing of PVDF to form a battery separator has significant advantages over electrospinning, such as greater processing speeds and solvent-free operation, and meltblowing has the potential to fabricate unique mat structures that have mechanical strength to serve as a battery separator.

In this work we use a commercially-scalable meltblowing pilot-plant equipment to produce high-quality meltblown PVDF mats. We report the physical, chemical, and electrochemical properties of meltblown PVDF relevant to its use as a Li-ion battery separator.

Experimental

We used an experimental grade of Poly(Vinylidene difluoride) (PVDF) Kynar® resin RC 10,287 (Arkema, Inc.). The resin has low-molecular weight (15 to 100 kDa), melt viscosity of 20 Pa·s at 230° C at a shear rate of 100 s^{-1}, and a 2.0 poly-dispersity index. Chain-transfer agents in high level during polymerization were used to create a polymer with high melt-strength and high extensional viscosity, ideal for a meltblowing process [6–8].

Meltblowing Process

We described in a previous publication the details of the meltblowing process with the Reicofil and the Biax die geometry, and we showed that PVDF Kynar® resin RC 10,287 may be meltblown in a Biax meltblown [6]. In this work, we used a 1.2-m wide Reifenhauser-Reicofil R4 Meltblown pilot line at the Nonwovens Institute at NC State University (Fig. 1, Appendix C) for meltblowing the same PVDF resin [54]. The die was a single row with 45 holes per inch, with 1.2 mm die tip and 1.2 mm setback. The temperature in the first two extruder zones were 50 ºC and 180 ºC, respectively, while the temperature was kept at 240 ºC elsewhere downstream, including the hot air jets that impinged upon the extruded melt. The process variables controlled were airflow rate (in $m^3\ h^{-1}$), polymer throughput (in kg h^{-1}), die-to-collector distance (DCD, in cm) and basis weight (BW, in g m^{-2}). Based on our previous work [6], we designed experiments with the most significant combinations of these variables (Table 2). One production run for each cell entry in Table 2 was performed.

Table 2. Design of experiments for meltblowing PVDF. Die-to Collector-Distance was 15 cm and Basis Weight was 40 g m^{-2} unless otherwise specified (Number(s) in cell correspond(s) to sample number). [a]DCD = 20 cm, [b]BW = 30 g m^{-2}, [c]BW = 20 g m^{-2}.

Throughput (kg h^{-1})	11	36	46	69
Air flow ($m^3\ h^{-1}$)				
600		*4*		
800	*6*			
1000	*7,8*[c]			
1100		*3*	*1*[a]	*5*
1200		*2*[a,b]		

Microscopy

To examine the fiber morphology, we used a field emission scanning electron microscope (FEI Verios 460L). Images were taken at 1000-2500X under a 2 kV accelerating voltage. We determined fiber diameters, using Fiji (ImageJ) software, by taking at least 100 measurements from 5 different areas in each sample. We performed cryo-SEM measurements using a JEOL JSM-7600F SEM outfitted with a cryogenic transfer system and stage (-180 ºC) to visualize fibers with and without absorbed liquid electrolyte.

Thickness and solid volume percent

We used a Mitutoyo micrometer to measure mat thickness. Solid volume percentage ε is calculated with Eq. (1):

$$\varepsilon = \left(\frac{W}{t\rho_{\text{fiber}}} \right) \times 100 \qquad (1)$$

where W is the basis weight of the mat in g cm^{-2}, t is the thickness in cm, and ρ_{fiber} is the density of the polymer in g cm^{-3}.

Capillary Flow Porosimetry

An in-plane porometer (Porous Materials Inc.) was used to analyze the pore size and distribution of the nonwovens mats. Samples were analyzed with a highly-wetting liquid (Salwick®) with a known surface tension of 20.1 dynes cm^{-1}. We did not detect a visible contact angle, and a contact angle of 0º was used for calculating pore diameter by using the Young–Laplace equation [55]: $D = 4\gamma_{L/G} cos\theta / p$, where p is the extrusion pressure in MPa, D is the pore diameter in mm, $\gamma_{L/G}$ is the surface tension of Salwick in N/mm, and θ is the contact angle of Salwick with the sample. Porosimetry provides the pore diameter at the most constricted part of the pore, the bubble point diameter, as well as the pore-diameter distribution.

Fourier-Transform Infrared Spectroscopy (FT-IR)

FT-IR measurements were performed with a ThermoFischer Nicolet™ iS50 FTIR Spectrometer with a wavenumber resolution of 2 cm^{-1} to determine the percentage of β-phase in the meltblown mats. Because of the absence of the γ-phase (no peak at 1234 cm^{-1}), the percentage of β is [56]:

$$F_\beta = \frac{I_{840}}{\left(\frac{K_{840}}{K_{763}}\right)\cdot I_{763} + I_{840}} \times 100 \qquad (2)$$

where, I_{840} and I_{763} are the absorbencies (peak areas) at 840 and 763 cm^{-1}; K_{840} and K_{763} are equal to 7.7×10^4 and 6.1×10^4 cm^2 mol^{-1}. These data are reported in the Appendix C.

Electrolyte Uptake

Preliminary experiments revealed the PVDF mats absorbed electrolyte quickly (<1 s). We determined equilibrium electrolyte uptake with Eq. (3) by weighing the separators before and after soaking for 10 min in a 1M $LiPF_6$ Ethylene Carbonate/Dimethyl Carbonate 1:1 v/v mixture.

$$\text{Electrolyte uptake} = \left(\frac{W_a - W_b}{W_b}\right)\times 100 \qquad (2)$$

where W_b and W_a are the weights of separator before and after soaking in the electrolyte, respectively.

Ionic Conductivity

After punching out disc samples (15.9 mm diameter) and measuring their thickness, in an Argon-filled glove-box we sandwiched the separators between stainless steel spacers and added 50 µl of 1M $LiPF_6$ in EC/DMC (1:1 v/v). We assembled the structure in a CR2032 coin cell and performed electrochemical impedance spectroscopy (EIS) measurements with a Bio-Logic VMP3 16-Channel Potentiostat. The frequency sweep ranged from 500 kHz to 1 Hz with an amplitude of

10 mV. We measured the conductivity at high temperatures with a temperature-controlled chamber. The conductivity σ is calculated with Eq. (4):

$$\sigma = \frac{t}{R_{ion} \cdot A} \qquad (4)$$

where t is the membrane thickness, R_{ion} is the measured ionic resistance (high-frequency intercept of Nyquist plot), and *A* is the membrane area.

Rate capability and cyclying performance.

We assembled coin cells with a $LiCoO_2$ cathode (Electrodes and More, Richardson, TX) and a Li metal anode, with 1 M $LiPF_6$-EC/DMC (1:1 v/v) and performed chronopotentiometry measurements with the VMP3. We conditioned the cells by cycling them between 3 V and 4.20 V at a constant rate of C/20 for 5 cycles and thereafter cycled them at different C-rates at room temperature. A minimum of 3 replicas per separator were assembled into coin cells and cycled to assess reproducibility.

Results and Discussion

A high extensional viscosity, despite its low molecular weight, is a unique characteristic of this grade of PVDF that enabled meltblowing the polymer at high air flow rates (up to 1200 $m^3\ h^{-1}$). This flow rate represents the upper limit for normal low-viscosity PP designed for meltblowing. The average fiber diameter ranged from 1.4 to 2.5 µm, with 30-40% sub-micron fibers (as low as 400 nm) (Fig. 1). The fiber diameter of these mats are similar to current meltblown PP at similar throughput. Comparable results have been obtained in literature only with ad hoc modifications of the equipment/process [57–59] or with special in-house resins [60]. Our work, to our knowledge, is the first instance in which not only PVDF mats have been fabricated with an industrially-made resin on a large scale meltblowing equipment, but the meltblown PVDF mats have also shown such a low-fiber diameter.

Strong fiber-fiber bonds were formed during the meltblowing process, and the mat thickness varied from ~ 70 to 140 μm. Fig. 1 shows representative SEM images of the mats and the fiber diameter distributions. The distributions are surprisingly narrow, spanning only few microns in all cases, an essential feature for most membrane applications. The mats with the lowest average fiber diameter were obtained either by decreasing the polymer throughput or by increasing the airflow rate. However, the maximum airflow at a specific throughput is dictated by the extensional viscosity and natural draw ratio of the polymer. Lower throughputs require lower air flows to avoid fiber breakage. For example, samples 2 and 3 were made at 36 kg h^{-1} and at 1200 and 1100 m^3 h^{-1}, respectively, and they show a similar average fiber diameter as samples 6, 7, and 8, whose throughputs and airflows are lower. If throughputs and air flow are not balanced, a high instability leads to fiber roping, entanglements, and a wide-size distribution, as in case of samples 6, 7, and 8, where throughputs were low with a high airflow, or in case of sample 4, where airflow was too low. All samples show a solid volume percentage of ~20%, suitable for battery separator applications.

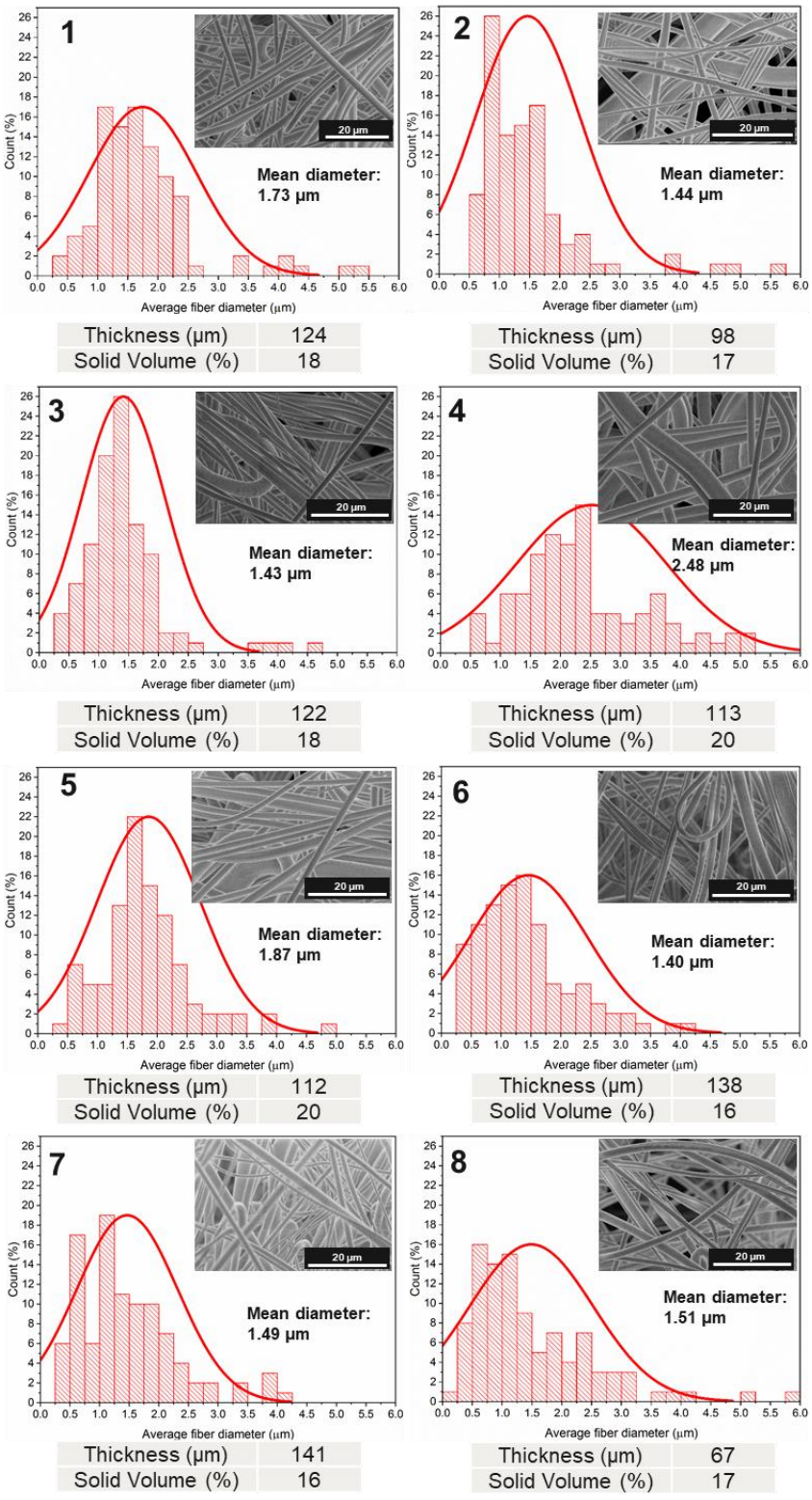

Figure 1. SEM and fiber diameter distributions of meltblown samples. Numbers in figures correspond to entries in Table 2.

Cryo-SEM of meltblown mats imbibed with electrolyte revealed that interactions occur between the fibers and the electrolyte. In previous work [6], we reported on the absorption of electrolyte in the outer surface of the PVDF fibers, with a subsequent localized change in crystallinity. Depending on the fiber size, the solvent is absorbed differently across the fiber cross-section because of the difference in crystallinity. Fibers with a diameter <1 µm show a cracked cross-section, indicating a deeper solvent penetration, while larger fibers show a rough and homogeneous cross section (Fig. 2). We believe crystalline and amorphous domains are distributed differently in fibers with different diameters. Results from Fig. 2 show that electrolyte penetrates deeper in small fibers (<1 µm), which suggest a more amorphous core compared to bigger fibers.

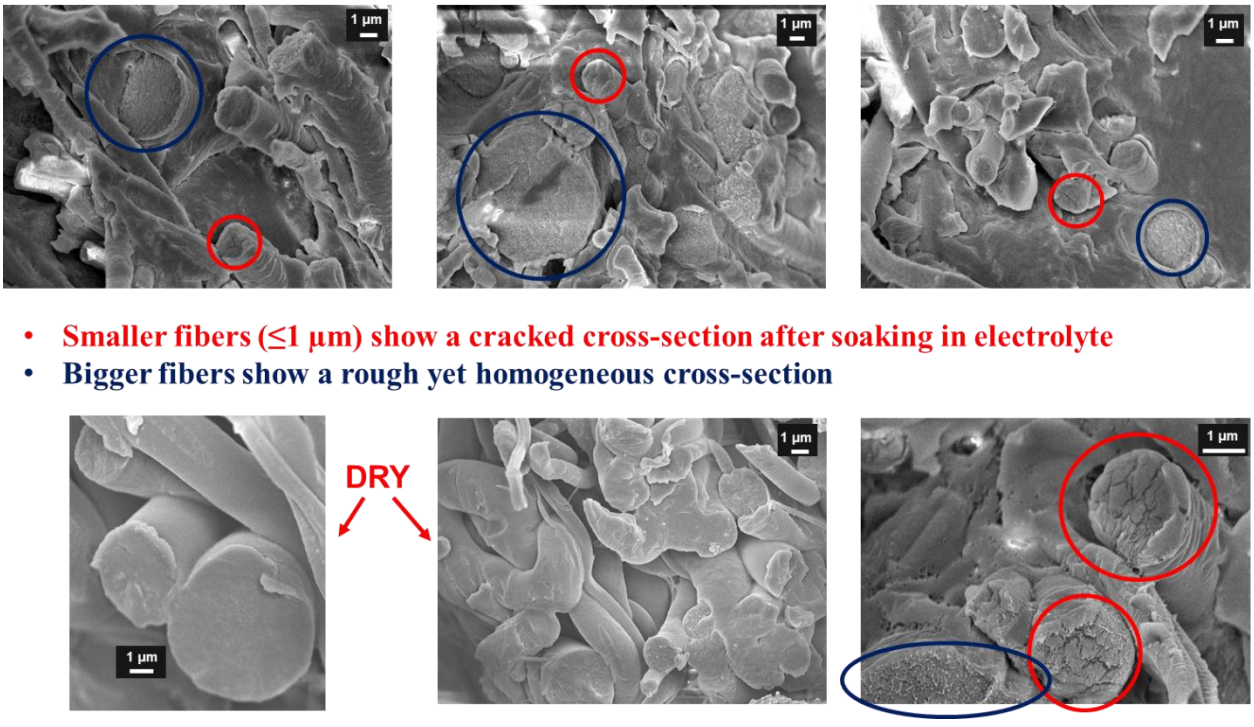

Figure 2. Cryo-SEM images of meltblown PVDF in 1M $LiPF_6$ EC/DMC electrolyte. Small-diameter fibers are cracked and circled in red, larger homogeneous fibers are circled in blue. Dry fiber cross-sections are reported for comparison.

Pore Analysis, Electrolyte Uptake, and Ionic Conductivity

The PVDF meltblown mats were pressed at 165 ℃ for 10-15 seconds and for 20-30 seconds. Melt-pressing increases the solid volume percentage by decreasing the mat thickness. A low thickness (< 25 μm) is desirable for Li-ion battery applications. Melt-pressing the mats significantly reduces the pore size from ~ 11 to ~ 2 μm for the shorter pressing times and down to 0.9 μm for the longer pressing times (Fig. 3). Although the fiber diameter is only slightly changed with pressing, the electrolyte absorbency is affected by partial melting of the polymer during the pressing operation. The PVDF fibers normally swell when immersed in electrolyte [6] due to liquid absorbed in the outer surface of the fiber. Melt-pressing for a short time does not allow the entire mat to reach high temperature, hence the fibers close to the mat surface that are partially melted will cool down quickly, increasing the amount of amorphous regions in the mat. Thus, the increase in fiber diameter after soaking in electrolyte for mats pressed for shorter times is higher (+42%) than for unpressed mats (+21%) because of a higher electrolyte absorbency. In contrast, melt-pressing for a long time will keep the material at high temperature for longer time during cooling, and the slower rate of annealing increases the crystallinity and decreases the absorbency of the fibers. In this case, the fibers partial melting is prolonged and there is a 15% increase in fiber diameter (from 1.41 to 1.63 μm) in the dry samples (before wetting) (Fig. 3 row b and c).

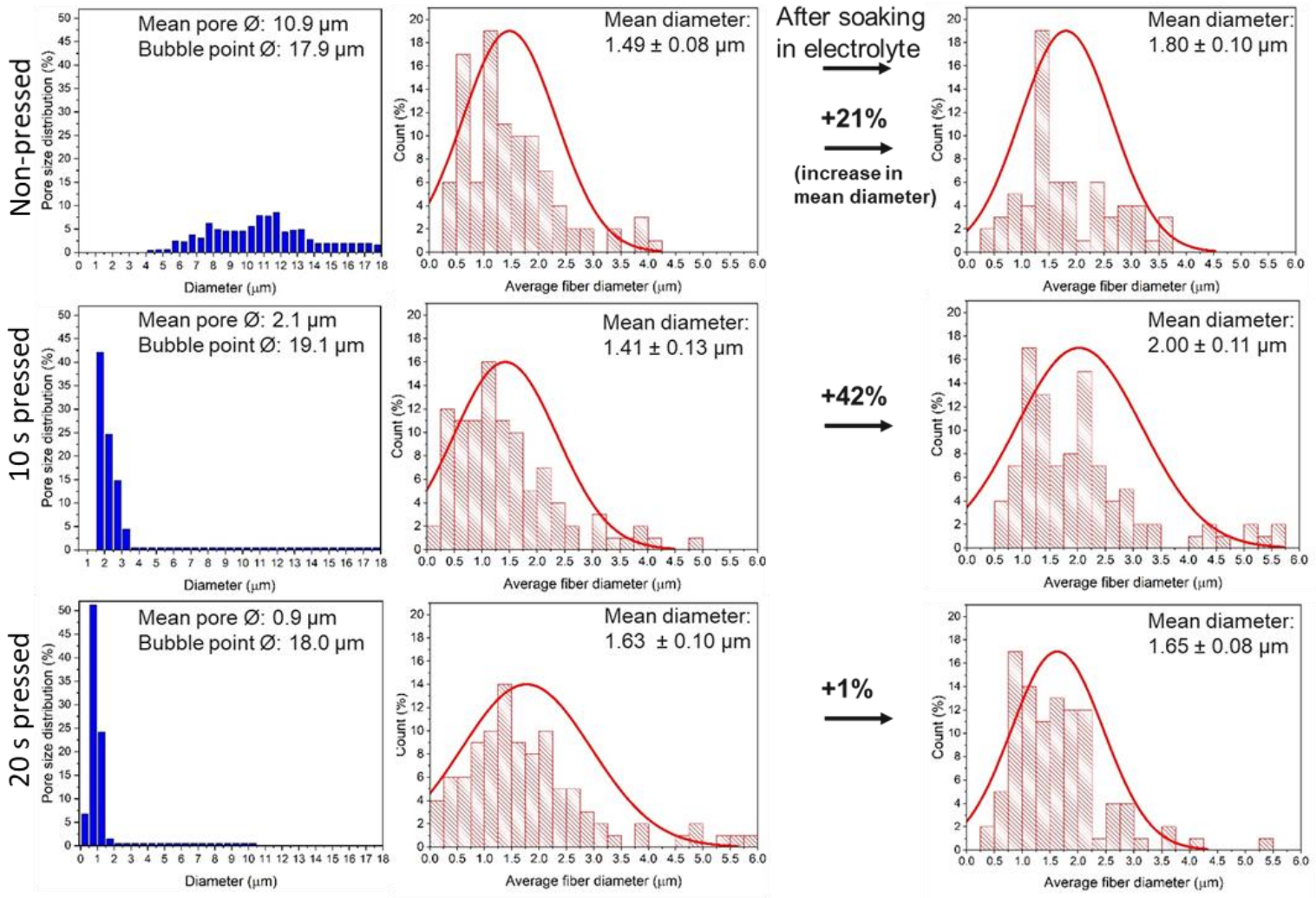

Figure 3. Pore and diameter distributions before and after soaking in 1M LiPF6 EC/DMC electrolyte of sample 7 (Table 2) unpressed (row a), melt-pressed for 10 s (row b), and melt-pressed for 20 s (row c).

The bubble-point diameter (an indicator of the largest pore diameter), and the mean-pore diameter for all samples pressed and non-pressed are shown in Fig. 4a. The pore size is determined by a combination of throughput and airflow; samples made at high throughputs (*e.g.*, sample 5) or at low airflow (*e.g.*, sample 4) show high bubble-point and mean-pore diameters. Most samples have a mean pore size between 10 and 14 μm, while the bubble-point diameter is generally low for samples at low throughputs (*e.g.*, sample 6 and 7). Thermal compacting the samples reduces their thickness approximately 3-fold (Fig. 4b) from 110-160 to 40-50 μm; the bubble pore diameters vary significantly for the unpressed mats, but they are nearly all ~ 17 μm for the pressed mats. The mean pore diameter depends on fiber diameter and solid volume percent [61–63], and since the solid volume percentage is nearly constant for all pressed samples except for short-time-pressed sample 1 (essentially identical thickness, same basis weight and polymer density), the difference in pore size between pressed samples is due principally to the difference between their fiber diameter. The ionic conductivity is related to the electrolyte uptake, which is usually higher for unpressed samples because of the higher pore size and lower solid volume percentage. Samples 6 and 7 (lowest throughputs and fiber diameters) showed low mean pore diameter (11 μm), highest thickness (~170 μm) and highest conductivity (9.6 mS/cm). After thermal compaction, the conductivity of most samples is ~ 0.5–1 mS/cm, generally 2 or 3 times lower than for unpressed samples.

Separators with varying requirements may be fabricated by appropriate choice of the processing conditions, and some generalizations can be made for the Reicofil equipment. For example, for separators requiring high conductivity without stringent thickness limitations, a low throughput (11 kg/h) and high airflow (800-1000 m^3/h) produces mats with high porosity but still small fiber diameters. If there are stringent thickness limitations, one could either decrease the

basis weight (*e.g.*, sample 8), increase both throughput and airflow (*e.g.*, sample 2, this can only happen with polymers with high melt strength), or melt-press the samples for a short time (10 s). In the last case, a compromise between thickness, fiber diameter and conductivity is desirable, as in samples 1, 6, and 7. These samples have a low average fiber diameter and a wide-size distribution, which allowed them to cycle in a Li/$LiCoO_2$ cell. In contrast, it was not possible to cycle samples with big fiber diameter (or big pore size) and/or narrow distribution because of internal cell failures (not shown here). Hence, we selected sample 1 and 6 (from Table 2) for cell-cycling performance measurements.

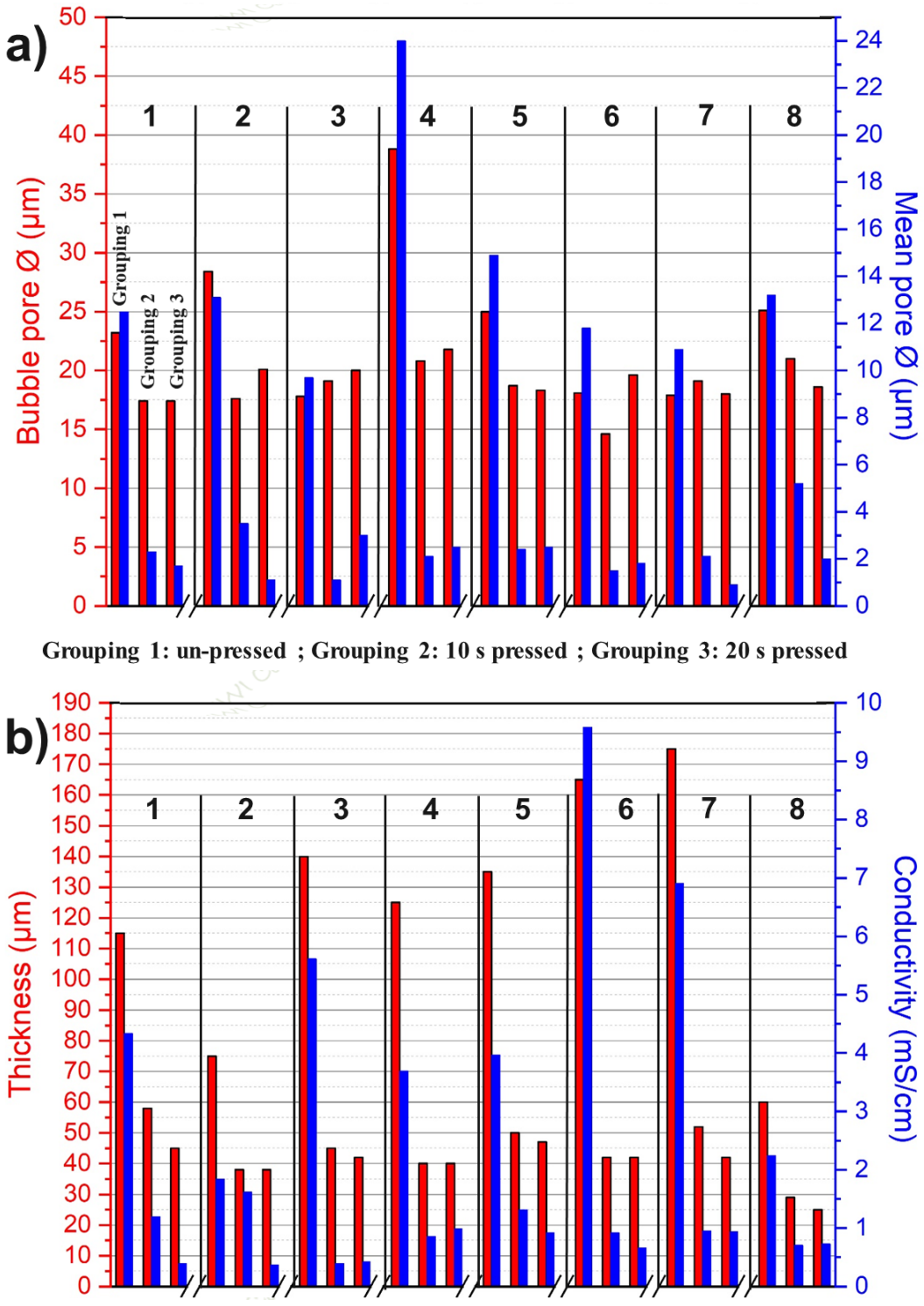

Figure 4. Bubble point and mean pore diameters (a), thickness and ionic conductivity (after soaking in 1M $LiPF_6$ EC/DMC) (b) of meltblown PVDF samples. Numbers at the top of each figure correspond to sample number (Table 2).

Cell-Cycling Performance

The first-cycle capacity, obtained at a C/10 discharge rate (Fig. 5a), is similar for both meltblown PVDF separators and Celgard® 2500, a commercial PP separator. However, we noticed that, in most instances, cells with meltblown PVDF separators could not reach a full charge after assembling and cycling them at C/10 rate. Instead, the potential became stable at ~3.9 V for as long as current was applied. Nonetheless, after cycling the cells at C-rates higher than C/10, we were able to not only obtain full charge at those C-rates, but we could reach the upper cut-off voltage (4.2 V) even at low C-rate, *e.g.* C/20 (Fig. 5b). We interpret this as a sort of necessary activation step. Since this activation step was needed in almost all instances, we took SEM images of the separator after cycling to examine at possible morphological changes (Fig. 3, Appendix C). Results show that the fibers after use in a cycled cell are no longer smooth, but show a significant increase in roughness. We speculate that this morphological change is related to the activation step. There are new features present on the fiber surface that may be related to the interactions between the PVDF and the electrolyte[6] and may be a reason of cycling instability, as discussed below.

Only cells with samples 1, 3, 6, and 7 were able to completely charge (4.2 V upper cut-off voltage was reached). Because in preliminary experiments cells using sample 6 showed lower capacity loss compared to the other samples, we cycled sample 6 separators in Li/$LiCoO_2$ cells for 50 charge/discharge cycles at C/5 rate to determine if meltblown PVDF separators were capable of repeated, cyclic use. A constant capacity loss in the first 50 cycles was indicative of instability problems (Fig. 5d), while the coulombic efficiency remained high for the first 35 cycles but decreased afterwards. Possible morphological changes to the fibers and large pore size, which may permit electronic short, may be the reason of decrease in cycling capacity and columbic efficiency.

We believe that large pore size caused micro-shorts, especially in cells with sample 2, 4, 5, and 8, which were not able to completely charge. On the other hand, the activation step and fiber morphological changes suggest that material(s) has (have) leached from the PVDF fibers in the mat is (are) irreversibly oxidized in the cell before the battery is able to cycle. Because chain-transfer agents, such as C2 to C18 hydrocarbons and alkyl and aryl esters, are used in high level (up to 30% of the total monomer) during polymerization, there are likely little amounts of residual monomer left in the PVDF resin [8]. The latter may also contain additives, such as low-molecular weight glycols, and other surfactants ((non-)ionic or (non-)fluorinated) to improve melt-processability of the PVDF resin. Chain-transfer agents, additives, and surfactants are susceptible to oxidation and our electrochemical data suggest they remain in the Kynar® resin that we used.These residual components result in fiber morphological changes, separator activation step, and unstable cell capacity.

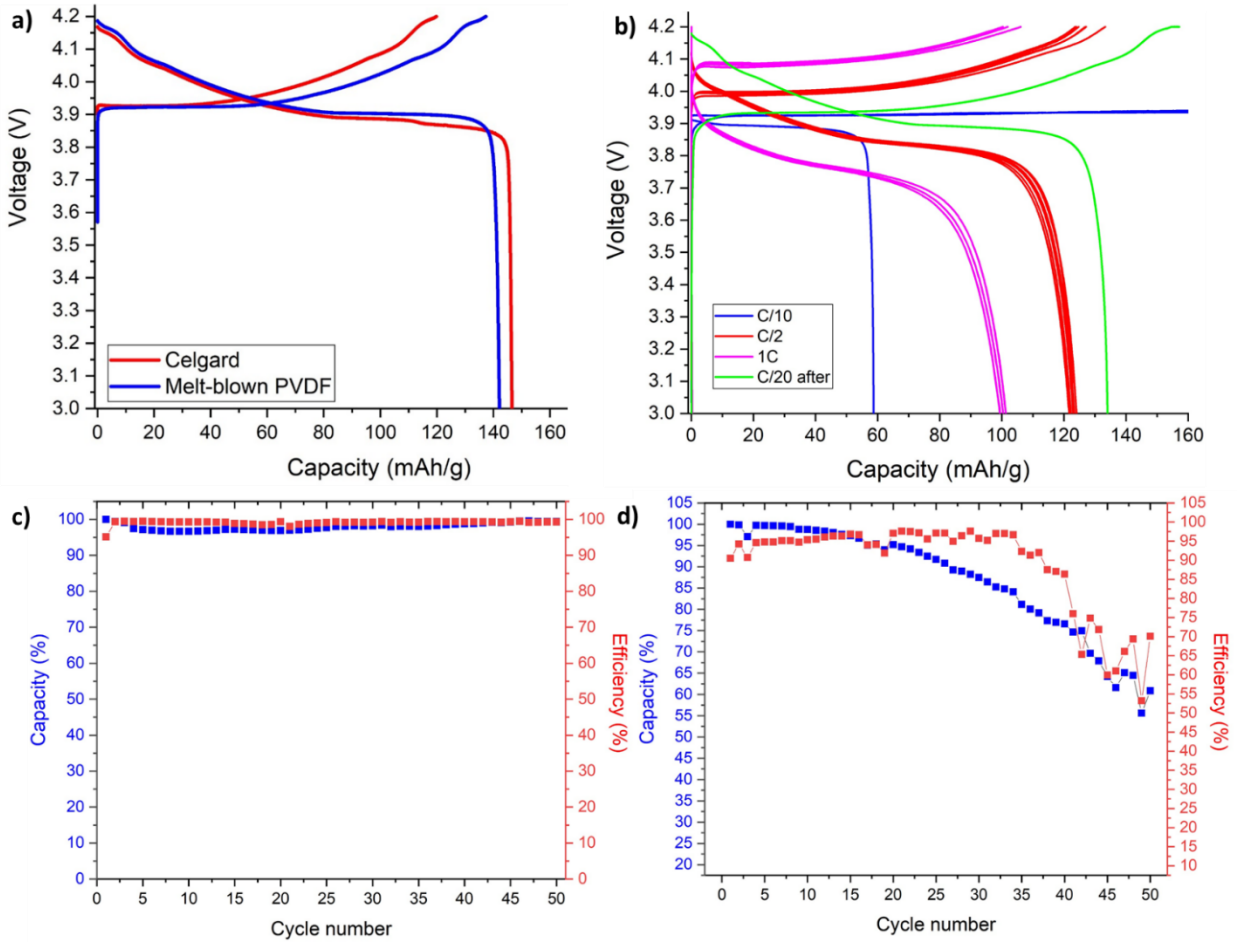

Figure 5. First-cycle capacity of Celgard® and unpressed meltblown PVDF (sample 6, Table 2) at C/10 rate (a), charge-discharge curves at of meltblown PVDF (b), and cycling stability at C/5 of Celgard® (c) and of meltblown PVDF (d).

Melt-pressing decreases the thickness of the separators, bringing it close to market requirements (15-25 [9,31]), but the process modifies irreversibly the fiber mat structure. As previously mentioned, both the pore size and the electrolyte uptake decrease after melt-pressing (Fig. 3), and these changes not only have an effect on the ionic conductivity (Fig. 4b), but also on cell performance, as discussed below. We performed rate capability experiments on sample 1 (Table 2) before and after melt-pressing. Fig. 6 shows that cells with meltblown PVDF separators have good capacity retention at C/10 and at C/5, but show a significant loss at C/2, with subsequent instability during cycling. However, after melt-pressing, the cell capacity shows a significant loss

(40%) even at C/5. It is important to note that cells with pressed and unpressed separators show a similar capacity loss (~20%) at C/10 after rate-capability experiments, suggesting that the increased capacity loss at high C/rate for cells with melt-pressed separator is reversible. The interactions between the PVDF and the electrolyte play an important role in cell performance, because the mat conductivity is affected by the fibers absorbing the electrolyte according to their distribution of crystalline and amorphous regions (Fig. 2 and 4). Melt-pressing modifies the ability of the fibers to absorb the electrolyte (Fig. 3), which is reflected in the cell performance (Fig. 6). Moreover, the decrease in pore size leads to a decrease in the amount of electrolyte present, resulting in a decrease in local current density and an increase in electrode over-potential. The latter is clearly visible in Fig. 6, where the cell containing a melt-pressed sample reached the upper cut-off voltage at a lower capacity (hence faster) than the one with unpressed meltblown PVDF.

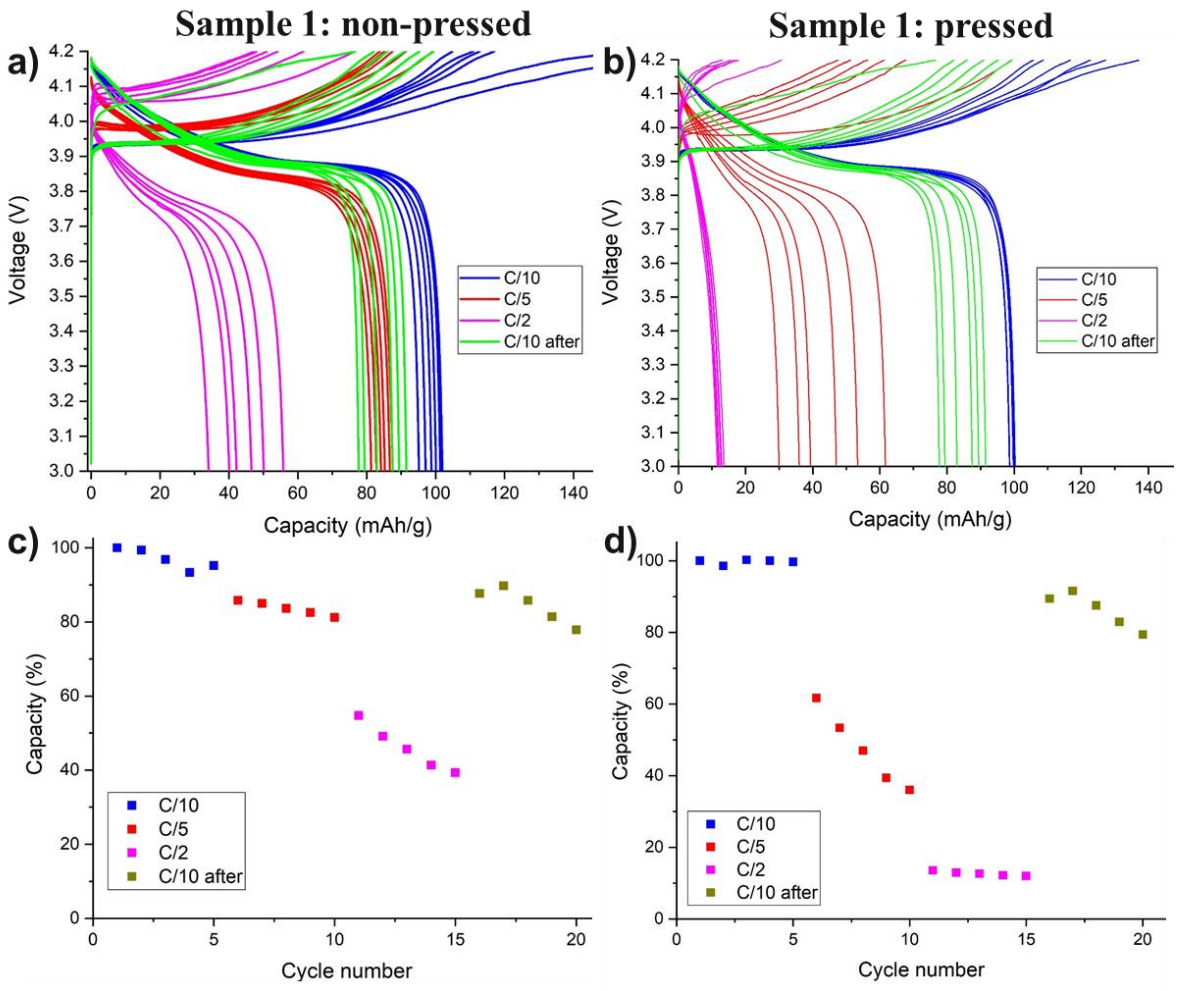

Figure 6. Charge-discharge curves and rate capability data of sample 1 meltblown PVDF before (a, c) and after melt-pressing (b, d).

Conclusion

We have shown it is possible to process PVDF Kynar® resin RC 10,287 in pilot-plant scale meltblowing equipment, and we obtained high-quality mats. By changing the process variables, we obtained an average fiber diameter as low as 1.4 µm, which is the lowest end of this technology at its current state. Fiber mats showed in general 30-40% sub-micron fibers with diameters as small as <400 nm. Melt-pressing the mats reduces the thickness and pore size, and increases the solid volume percentage. We have drawn some relationships between the process parameters and the

mat properties, including guidelines on obtaining specific desired separator properties. We reported the electrochemical properties and cycling performance of meltblown PVDF relevant to its use as a Li-ion battery separator. The cells containing meltblown PVDF separators showed a first-cycle capacity similar to Celgard®, with good rate capability up to 1C. Cycle-life experiments showed long-term stability issues for these separators probably due to large pore size that caused micro-shorts. The activation step necessary to completely charge the batteries and fiber morphological changes after cycling are most likely due to chain-transfer agents, additives and/or surfactants leached from the fibers and oxidized during battery operation.

The meltblowing process is advantageous because of high-volume production, ease of manufacturing and small-diameter fibers. PVDF Kynar® resin RC 10,287 and the processing parameters employed in this work enabled continuous polymer processing from the Reicofil meltblown line; processing conditions outside the range reported in Table 2, continuous fibers could not be meltblown. As a result, candidate mats may be formed by meltblowing this polymer, however challenges remain to be addressed for their use in battery separator applications.

References

[1] Abraham K. M., "Polymer Electrolytes Reinforced by Celgard® Membranes", *J. Electrochem. Soc.* 142, 683, 1995.

[2] Arora P., Zhang Z., "Battery Separators", *Chem. Rev.* 104, 4419–4462, 2004.

[3] Waqas M. *et al.,* "Recent Development in Separators for High-Temperature Lithium-Ion Batteries", *Small* 15, 2019.

[4] Barbosa J.C., Dias J.P., Lanceros-Méndez S., Costa C.M., "Recent advances in poly(Vinylidene fluoride) and its copolymers for lithium-ion battery separators", *Membranes (Basel).* 8, 2018.

[5] Luiso S., Fedkiw P., "Lithium-ion battery separators: Recent developments and state of art", *Curr. Opin. Electrochem.,* 20, 99–107, 2020.

[6] Luiso S., Henry J.J., Pourdeyhimi B., Fedkiw, P. S., "Fabrication and Characterization of Meltblown Poly(vinylidene difluoride) Membranes", *ACS Appl. Polym. Mater.* 2, 2849–2857, 2020.

[7] Henry J.J., Goldbach J., Stabler S., Devisme S., Chauveau J., "Advancements in the production of meltblown fibres", *Filtr. Sep.* **53**, 36–40, 2016.

[8] Henry J.J., Goldbach J., Stabler S., Chauveau J., "High melt flow fluoropolymer composition", *US Patent Application No. 20170088989(A1)*. 1, 2015–2018, 2017.

[9] Li Y., Li Q., Tan Z., "A review of electrospun nanofiber-based separators for rechargeable lithium-ion batteries", *J. Power Sources,* 443, 227262, 2019.

[10] Gopalan A. *et al.,* "Development of electrospun PVdF – PAN membrane-based polymer electrolytes for lithium batteries", 325, 683–690, 2008.

[11] Alcoutlabi M. *et al.,* "Fabrication and characterization of SiO2/PVDF composite nanofiber-coated PP nonwoven separators for lithium-ion batteries", *J. Polym. Sci. Part B Polym. Phys.,* 51, 349–357, 2013.

[12] Gao K., Hu X., Dai C., Yi T., "Crystal structures of electrospun PVDF membranes and its separator application for rechargeable lithium metal cells", *Mater. Sci. Eng. B Solid-State Mater. Adv. Technol.* 131, 100–105, 2006.

[13] Kim J. R., Choi S.W., Jo S.M., Lee, W.S., Kim, B.C., "Electrospun PVdF-based fibrous polymer electrolytes for lithium ion polymer batteries", *Electrochim. Acta* 50, 69–75, 2004.

[14] Choi S.W., Jo S.M., Lee W.S., Kim Y.R., "An electrospun poly(vinylidene fluoride) nanofibrous membrane and its battery applications", *Adv. Mater.* 15, 2027–2032, 2003.

[15] Kane S.N., Mishra A., Dutta A.K., "Polyvinilidine fluoride (PVDF) nanofiber membrane for Li-ion rechargeable battery separator", *Journal of Physics: Conference Series* 755, 2016.

[16] Zhou W., Bahi A., Li Y., Yang H., Ko F., "Ultra-filtration membranes based on electrospun poly(vinylidene fluoride) (PVDF) fibrous composite membrane scaffolds", *RSC Adv.* 3, 11614–11620, 2013.

[17] Agyemang F.O., Li F., Momade F.W.Y., Kim H., "Effect of poly(ethylene oxide) and water on electrospun poly(vinylidene fluoride) nanofibers with enhanced mechanical properties as pre-filter for oil-in-water filtration", *Mater. Chem. Phys.* 182, 208–218, 2016.

[17] Hou D., Lin D., Ding C., Wang D., Wang J., "Fabrication and characterization of electrospun superhydrophobic PVDF-HFP/SiNPs hybrid membrane for membrane distillation", *Sep. Purif. Technol.* 189, 82–89, 2017.

[19] Laurita, R. *et al.,* "Plasma Processing of Electrospun Li-Ion Battery Separators to Improve Electrolyte Uptake", *Plasma Process. Polym.* 13, 124–133, 2016.

[20] Choi, S. *et al.,* "Electrospun PVDF nanofiber web as polymer electrolyte or separator", *Electrochim. Acta* 50, 339–343, 2004.

[21] Li X. *et al.,* "Polymer electrolytes based on an electrospun poly(vinylidene fluoride-co-hexafluoropropylene) membrane for lithium batteries", *J. Power Sources* 167, 491–498, 2007.

[22] Cheruvally, G. *et al.,* "Electrospun polymer membrane activated with room temperature ionic liquid: Novel polymer electrolytes for lithium batteries", *J. Power Sources* 172, 863–869, 2007.

[23] Liu K. *et al.,* Electrospun core-shell microfiber separator with thermal-triggered flame-retardant properties for lithium-ion batteries", *Sci. Adv.* 3, e1601978, 2017.

[24] Raghavan P. *et al.* "Preparation and electrochemical characterization of polymer electrolytes based on electrospun poly(vinylidene fluoride-co-hexafluoropropylene)/polyacrylonitrile blend/composite membranes for lithium batteries", *J. Power Sources* 195, 6088–6094, 2010.

[25] Li X., Cao Q., Wang X., Jiang S., Deng H., "Preparation of Poly(vinylidene fluoride)/Poly(methyl methacrylate) Membranes by Novel Electrospinning System for Lithium Ion Batteries", *J. Appl. Polym. Sci.* 122, 2616–2620, 2011.

[26] Wu N., Cao Q., Wang X., Li X., Deng, H., "A novel high-performance gel polymer electrolyte membrane basing on electrospinning technique for lithium rechargeable batteries", *J. Power Sources* **196**, 8638–8643, 2011.

[27] Shubha N., Prasanth R., Hng H.H., Srinivasan, M., "Study on effect of poly (ethylene oxide) addition and in-situ porosity generation on poly (vinylidene fluoride)-glass ceramic composite membranes for lithium polymer batteries", *J. Power Sources* 267, 48–57, 2014.

[28] Yanilmaz M., Lu Y., Dirican M., Fu K., Zhang, X., "Nanoparticle-on-nanofiber hybrid membrane separators for lithium-ion batteries via combining electrospraying and electrospinning techniques', *J. Memb. Sci.* 456, 57–65, 2014.

[29] Yanilmaz M., Chen C., Zhang, X., "Fabrication and characterization of SiO 2 /PVDF composite nanofiber-coated PP nonwoven separators for lithium-ion batteries", *J. Polym. Sci. Part B Polym. Phys.* 51, 1719–1726, 2013.

[30] Wu S., Ning J., Jiang F., Shi J., Huang, F., "Ceramic Nanoparticle-Decorated Melt-Electrospun PVDF Nanofiber Membrane with Enhanced Performance as a Lithium-Ion Battery Separator", *ACS Omega* 4, 16309–16317, 2019.

[31] Lee H., Yanilmaz M., Toprakci O., Fu K., Zhang X., "A review of recent developments in membrane separators for rechargeable lithium-ion batteries", *Energy Environ. Sci.* 7, 3857–3886, 2014.

[32] Waqas M. *et al.,* "High-Performance PE-BN/PVDF-HFP Bilayer Separator for Lithium-Ion Batteries", *Adv. Mater. Interfaces* 6, 1801330, 2019.

[33] An M.Y., Kim H.T., Chang D.R., "Multilayered separator based on porous polyethylene layer, Al2O3 layer, and electro-spun PVdF nanofiber layer for lithium batteries", *J. Solid State Electrochem.* 18, 1807–1814, 2014.

[34] Fu Q. *et al.,* "Mechanically Reinforced PVdF/PMMA/SiO2 Composite Membrane and Its Electrochemical Properties as a Separator in Lithium-Ion Batteries", *Energy Technol.* 6, 144–152 2018.

[35] Pan J. L. *et al.,* "Ultrathin and Strong Electrospun Porous Fiber Separator", *ACS Appl. Energy Mater*. 1, 4794–4803, 2018.

[36] Shen X. *et al.,* "Core-shell structured ceramic nonwoven separators by atomic layer deposition for safe lithium-ion batteries", *Appl. Surf. Sci.* 441, 165–173, 2018.

[37] Zhang F., Ma X., Cao C., Li J., Zhu Y., "Poly(vinylidene fluoride)/SiO2 composite membranes prepared by electrospinning and their excellent properties for nonwoven separators for lithium-ion batteries", *J. Power Sources* 251, 423–431, 2014.

[38] Wang H., Li H., Yu L., Jiang Y., Wang K., "Synthesis of porous Al2O3-PVDF composite separators and their application in lithium-ion batteries", *J. Appl. Polym. Sci.* 130, 2886–2890, 2013.

[39] Chen H.L., Jiao X.N., "Preparation and characterization of Polyvinylidene fluoride/Octaphenyl-Polyhedral oligomeric silsesquioxane hybrid Lithium-ion battery separators by electrospinning", *Solid State Ionics* 310, 134–142, 2017.

[40] Zhu Y. *et al.,* "Composite of a nonwoven fabric with poly(vinylidene fluoride) as a gel membrane of high safety for lithium ion battery", *Energy Environ. Sci.* 6, 618, 2013.

[41] Alcoutlabi M., Lee H., Watson J.V., Zhang, X., "Preparation and properties of nanofiber-coated composite membranes as battery separators via electrospinning", *J. Mater. Sci.* 48, 2690–2700, 2013.

[42] Alcoutlabi M., Lee H., Zhang, X., "Nanofiber-Based Membrane Separators for Lithium-ion Batteries", *MRS Proc.* 1718, 157–161, 2015.

[43] Lee H., Alcoutlabi M., Watson J.V., Zhang, X., "Polyvinylidene fluoride-co-chlorotrifluoroethylene and polyvinylidene fluoride-co-hexafluoropropylene nanofiber-coated polypropylene microporous battery separator membranes", *J. Polym. Sci. Part B Polym. Phys.* 51, 349–357, 2013.

[44] Lee H., Alcoutlabi M., Watson J.V., Zhang, X., "Electrospun nanofiber-coated separator membranes for lithium-ion rechargeable batteries", *J. Appl. Polym. Sci.* 129, 1939–1951, 2013.

[45] Lee H. *et al.,* "Preparation and characterization of electrospun nanofiber-coated membrane separators for lithium-ion batteries" *J. Solid State Electrochem.* 18, 2451–2458, 2014.

[46] Zhu C. *et al.,* "Enhanced Wettability and Thermal Stability of a Novel Polyethylene Terephthalate-Based Poly(Vinylidene Fluoride) Nanofiber Hybrid Membrane for the Separator of Lithium-Ion Batteries", CS Appl. Mater. Interfaces 2017, 9, 31, 26400–26406, 2017.

[47] Wu, D. *et al.,* "A high-safety PVDF/Al2O3 composite separator for Li-ion batteries via tip-induced electrospinning and dip-coating", *RSC Adv.* 7, 24410–24416, 2017.

[48] Smoukov, S.K. *et al.,* "Scalable Liquid Shear-Driven Fabrication of Polymer Nanofibers", *Adv. Mater.* 27, 2642–2647, 2015.

[49] Velev O., Smoukov S., Marquez M., "Nanospinning of polymer fibers from sheared solutions". *US Patent No. 8,551,378.* Washington, DC: U.S. Patent and Trademark Office, 2013.

[50] Roh S., Williams A.H., Bang R.S., Stoyanov S.D., Velev, O.D., "Soft dendritic microparticles with unusual adhesion and structuring properties", *Nature Materials* 18, 1315–1320, 2019.

[51] Velev O.D., Smoukov S., Geisen P., Wright M.C., Gangwal, S., "Method for Fabricating Nanofibers", *US Patent No. 9,217,211.* Washington, DC: U.S. Patent and Trademark Office, 2015.

[52] Velev O.D., Roh S., “Fractal-like polymeric particles and their use in diverse applications”, *US Patent Application No. 20190153247(A1).* Washington, DC: U.S. Patent and Trademark Office, 2015.

[53] Luiso S., Williams A.H., Velev O.D., Fedkiw P.S., “Poly(Vinylydene difluoride) Soft Dendritic Colloids as Li-Ion Battery Separators”, *J. Electrochem. Soc.* (2020).

[54] Reifenhauser REICOFIL Meltblown Pilot Line. Available at: https://thenonwovensinstitute.com/wp-content/uploads/2015/04/Reifenhauser-Reicofil-Meltblown-Pilot-Brochure.pdf.

[55] Jena A., Gupata K., “Liquid Extrusion Techniques For Pore Structure Evaluation Of Nonwovens”, *Akshaya Jena and Krishna Gupta Porous Materials, Inc*., 83 Brown Road, Ithaca, NY 14850. *Int. Nonwoven J.* 45–53, 2003.

[56] Cai X., Lei T., Sun D., Lin, L., “A critical analysis of the α, β and γ phases in poly(vinylidene fluoride) using FTIR”, *RSC Adv.* 7, 15382–15389, 2017.

[57] Uppal R., Bhat G., Eash C., Akato K., “Meltblown Nanofiber Media for Enhanced Quality Factor”, *Fibers Polym.* 14, 660–668, 2013.

[58] Hassan M.A., Yeom B.Y., Wilkie A., Pourdeyhim, B., Khan, S.A., “Fabrication of nanofiber meltblown membranes and their filtration properties”, *J. Memb. Sci.* 427, 336–344, 2013.

[59] Lalagiri M. *et al.,* “Filtration Efficiency of Submicrometer Filters”, Ind. Eng. Chem. Res., 52, 46, 16513–16518, 2013.

[60] Li T. *et al.,* “One-Step Bark-Like Imitated Polypropylene”, *Polymers*, 11(8), 1307, 2019.

[61] Neckář, B., Ibrahim, S., “Theoretical Approach for Determining Pore Characteristics Between Fibers”, *Text. Res. J.* 73, 611–619, 2003.

[62] Lifshutz N., “On the ‘Mean Flow’ Pore Size Distribution of Microfiber and Nanofiber Webs”, *Int. Nonwovens J.* os-14, 1558925005os–14, 2005.

[63] Simmonds G.E., Bomberger J.D., Bryner M.A., “Designing Nonwovens to Meet Pore Size Specifications”, *J. Eng. Fiber. Fabr.* 2, 155892500700200, 2007.

[64] Yang D., Chen Y., “β-phase formation of poly(vinylidene fluoride) from the melt induced by quenching”, *J. Mater. Sci. Lett.* 6, 599–603, 1987.

CHAPTER 5: Poly(Vinylidene difluoride) Soft Dendritic Colloids as Li-Ion Battery Separators

Abstract

As an alternative to Li-ion battery (LIB) microporous membrane separators that are typically comprised of polyolefins, other materials and separator morphologies may yield increased cell performance. Here, we present a new class of LIB separators poly(vinylidene difluoride) (PVDF)-based and highly-branched, colloidal polymer particulates, called soft dendritic colloids, that are produced by shear-driven polymer precipitation within a turbulent nonsolvent flow followed by filtration. We show the morphology of the resulting PVDF particulates may be modulated from fibrous soft dendritic colloids to thin and highly porous sheet-like particles. The use of PVDF leads to low thermal shrinkage (5% at 90 ºC) and high tensile strength (<0.7% offset at 1000 psi), while the high porosity (up to 80%) and high particle surface area are responsible for high resulting conductivity (1.2 mS/cm), high electrolyte uptake (325%), and good cell capacity (112 mAh/g in Li/$LiCoO_2$ cell) with <10% loss after 50 cycles. Because shear-driven precipitation with filtration is a facile and versatile process to make a new class of LIB separators with one single polymer without requiring post-processing and with characteristics similar to commercially available battery separators, soft dendritic colloids are promising candidates as separators for next-generation batteries.

Introduction

LIBs are an essential energy storage system for a variety of applications because of their high energy-storage capabilities and long cycle life, comprising a $30 billion market as of 2017 [1–3]. The LIB separator market was $2.6 billion with a compound annual growth rate of 14% at the end of 2017, and it's projected to reach $8 billion by 2030 [3]. The structure and properties of

the separator, which is placed between the anode and the cathode of the battery, play a critical role in cell performance. The separator must be chemically and electrochemically stable and is usually not ionically conductive by itself; the liquid electrolyte imbibed within it effects ion transport. Indeed, the wettability of the separator by liquid electrolyte is important to affect low-internal resistance and high-ionic conductivity [4]. A high wettability permits rapid absorption of the electrolyte in the separator during cell assembly. A desirable battery separator is characterized by low ionic resistance, mechanical and thermal stability, and high affinity and wettability by electrolyte [5]. While separators may be classified according to their structure [6], recent developments tend to classify them as single- or multi-layered, ceramic-based, or surface-modified separators [7]. Polyolefin monolayer microporous separators are the most widely used, but their hydrophobic surface with low surface energy exhibits poor affinity to polar organic electrolytes, and they need surfactants to obtain a high electrolyte wettability [8,9].

Relative to conventional microporous polyolefin separators, fibrous polymeric membranes, such as electrospun nonwovens, have the advantage of low mass and high porosity; in addition, the fibrous mat provides good structural cohesion due to its intertwined fibers [10-13]. Although most polymers used to make fibrous battery separators have resulted in lower cell performance (lower ionic conductivity and, hence higher resistance) than conventional microporous separators, PVDF shows promising results because of its high polarity and good chemical stability and affinity for electrolytes commonly employed in Li-ion cells, owing to the presence of C–F groups [14-21]. PVDF is often used as a copolymer with hexafluoropropylene (HFP) to decrease the degree of crystallinity, and hence increase electrolyte uptake and ionic conductivity, but may decrease the mechanical and thermal properties of the separator; it is often necessary to create blends and composites of PVDF [22-24]. Electronically insulating metal oxides, such as SiO_2, Al_2O_3 and SnO_2

[25], or silicone [26] may be incorporated in the separator to increase membrane and cell performance, but often with non-scalable or expensive techniques, such as sol-gel method [27], in situ deposition, film casting [14], physical vapor deposition [28], or electrophoretic deposition [29].

A different approach to improve PVDF-based membranes is to optimize their morphology, with scalable preparation processes and without the use of composites and blends. In previous work, we prepared PVDF membranes for the first time via meltblowing, a well-established mass-production process for creating membranes with small pores, and we found that interactions between the PVDF fibers and electrolyte (1M $LiPF_6$ in EC/DMC) increase uptake and conductivity [30]. Luo *et al.* [31] have prepared polyethylene/PVDF-HFP separators through a solvent liberation method. The variation in solvent evaporation rate between N-methyl pyrrolidone and acetone creates a hierarchical structure with high porosity and high ionic conductivity. The authors attribute a lower cell capacity loss using these membranes to an inter-island structure formed in the membrane during the processing steps [32]. With a similar idea, Ye *et al.* [33] improved PVDF-HFP separators with an inter-particle chain structure. After casting the polymer from acetone and an electrolyte soaking and drying procedure, polymer chains rearrange toward a high-density and highly-porous structure. The interactions between solvents and non-solvents influence the formation of pores and phase transformation process [31, 34], leading to different morphologies, such as sponge-like or finger-like with an asymmetric distribution of pores [7, 21].

A new method of fabricating nanofibrous material in which a polymer solution is injected into a sheared nonsolvent flow has shown that membranes fabricated with these materials may be produced in a continuous, scalable process using a laminar nonsolvent flow to unidirectionally elongate the polymer droplet into a fiber [35, 36]. Additionally, the transition of the nonsolvent

flow from laminar to turbulent regime alters the morphology of the resulting particulates and may produce highly branched soft dendritic colloids (SDCs), which are characterized by a corona of nanofibers surrounding the core of a particle [37, 38]. The concentration of polymer in the injection solution dictates the morphology of the resulting particulates, with a low concentration resulting in fibrous structures, a high concentration resulting in thin, nano-sheet (NS) morphologies, and an intermediate concentration with combined fibrous-NS morphologies; the concentration at which the morphology transition happens is polymer dependent. In this work, we show that PVDF SDC separators produced by shear-driven polymer precipitation can find application as efficient, versatile, and stable LIB separators. We also investigate how battery performance may be modulated by the particle morphology in the SDC-based separator resulting from the precipitation process.

Experimental

Materials

We use polyvinylidene fluoride (PVDF, Sigma Aldrich, Mw = 530,000 Da), dimethyl sulfoxide (DMSO, Fisher Scientific) and ethanol (EtOH, Koptek) in this study. A Millipore vacuum filtration apparatus with a head diameter of 35 mm was used to filter particulate suspensions in EtOH.

Fabrication of PVDF SDC Membranes

PVDF pellets were dissolved in DMSO by heating at 110°C for 24 hours while stirred. Following dissolution, the PVDF solution was cooled to room temperature and injected at a rate of ~1 mL/s directly through a capillary into the shear zone of a colloidal mill (IKA Magic Lab) set to 20,000 rpm and filled with 500 mL of EtOH also at room temperature. The resulting PVDF SDC suspensions were then washed by centrifugation at 3.0 relative centrifugal force for 2

minutes, discarding the supernatant, and re-suspending the concentrated particles in 40 mL pure EtOH using a Vortex mixer. This process was repeated a minimum of five times to remove DMSO. The suspension was then adjusted to 0.1 wt.% PVDF in EtOH and a known volume of suspension was deposited on a Durapore® filtration membrane (0.45 micron pore size) using a Millipore vacuum filtration apparatus. The suspension was vacuum filtered for 30 minutes, resulting in the formation of the membrane. Samples were removed from the filtration funnel, sandwiched between two glass slides, and placed in an oven at 70°C for 24 hours to remove residual ethanol.

Microscopy and Tensile Strength

The morphology of SDC particles and their membranes were analyzed by field emission scanning electron microscopy (FEI-SEM, Verios 460L). We performed tensiometry on the membranes using a universal testing machine (Instron 4593) with 15 mm x 10 mm samples of varying thickness (15-50 μm) and a crosshead speed of 15 mm/min. A minimum of 4 replicas per membrane were measured for reproducibility.

Capillray Flow Porosimetry and Porosity

The inter-fiber spacing (pore) size was analyzed with an in-plane porometer (Porous Materials Inc.). Each sample was imbibed with a highly-wetting liquid (Galwick®) with a known surface tension of 15.9 dynes/cm. No visible contact angle was detected, so we assumed a contact angle of 0º for calculating pore diameter by using the Young–Laplace equation: $D = 4\gamma_{L/G} cos\theta \,/\, p$, where p is the extrusion pressure in MPa, D is the pore diameter in mm, $\gamma_{L/G}$ is the surface tension of Galwick in N/mm, and θ is the contact angle of Galwick with the sample.. This technique provides the population of pores with a specific diameter at every static pressure applied. By applying the same equations used to calculate the number average molecular weight (M_n), weight average molecular weight (M_w), and polydispersity index (PDI= M_w/M_n) to the

porosimetry results, we calculated the equivalent number average pore size (P_n), weight average pore size (P_w), and heterogeneity index (HG= M_w/M_n) [39]. Porosity was calculated as the complement of the ratio of geometrical density to fiber density: $P = 1 - \left(\frac{W}{t \cdot \rho_{fiber}} \right)$, where W is the basis weight (g/cm^2), t is the mat thickness (cm), and $\rho_{fiber} = 1.78$ g/cm^3 is PVDF density. A minimum of 4 replicas per membrane were measured for reproducibility.

Thermal Stability

The SDC membranes were placed in an oven at 90 °C for 1 hour, imaged, exposed to 130 °C for 1 hour, imaged, and finally exposed to 150 °C for 1 hour, and imaged. The shrinkage of the membranes was determined using pixel analysis on ImageJ software.

Electrolyte Uptake

Because the uptake of electrolyte by the PVDF membranes was fast (<1 s), we did not perform rate-of-wettability measurements. We determined electrolyte uptake with Eq. (1) by weighing the separators before and after soaking in a 1M $LiPF_6$ Ethylene Carbonate/Dimethyl Carbonate 1:1 by volume mixture for 10 min. A minimum of 3 replicas per membrane were measured for reproducibility.

$$\text{Electrolyte uptake} = \left(\frac{W_b - W_a}{W_a} \right) \times 100 \qquad (1)$$

where W_a and W_b are the weights of separator before and after soaking in the electrolyte.

Ionic Conductivity

We assembled CR2032 coin cells in an Argon-filled glove-box. The membranes were cut into disks (15.9 mm diameter). We measured the thickness of the separator and placed it between two stainless steel spacers to ensure symmetry of the circuit. We added 50 μL of 1M $LiPF_6$ in

EC/DMC (1:1 by volume) and crimped the cells with a pneumatic crimper. We obtained ionic resistance by performing electrochemical impedance spectroscopy (EIS) with a Bio-Logic VMP3 Potentiostat. The frequency sweeps ranged from 500 kHz to 1 Hz with an amplitude of 10 mV. The conductivity at high temperature was measured for 3 replicas per membrane with a temperature-controlled chamber. The conductivity σ is calculated with Eq. (2):

$$\sigma = \frac{t}{R_{ion} \cdot A} \qquad (2)$$

where t is the membrane thickness, R_{ion} is the measured ionic resistance (high-frequency intercept of Nyquist plot), and A is the membrane area.

Cell-Cycling Performance

For rate capability and cycling, we used a $LiCoO_2$ (Electrodes and More, Richardson, TX) cathode and Li metal anode, with 50 µL of 1 M $LiPF_6$-EC/DMC (1:1 v/v) and characterized them with the VMP3 potentiostat. We pre-cycled (conditioned) the cells between 3 V and 4.2 V at C/20 for 5 cycles and thereafter cycled the cells at C/10, C/5, C/2, and 1C rates at room temperature. The cycling stability was obtained by cycling the cells for 50 cycles at a C/5 rate. A minimum of 3 replicas per separator were assembled into coin cells and cycled to ensure reproducibility.

Results and Discussion

Membrane fabrication

At a concentration of 5 wt.% PVDF in the injection solution, the resulting particles have the characteristic highly branched, fibrous SDC structure (Fig. 1a, 1b, 1c). An increase in the concentration to 12.5 wt.% PVDF in the injection solution results in the formation of thin, but highly porous nano-sheet (NS) particulates (Fig. 1g, 1h, 1i). Particle morphology affects membrane formation during the filtration step. As the concentration of PVDF increased from 5% to 10 wt.%, the SEM images reveal that the membranes transition from an entirely fibrous network

to a mixed-morphology to a nano-sheet morphology, with pore sizes ranging from 10 to 500 nm (Fig. 1c, 1f, 1i). At a PVDF concentration of 12.5 wt.%, the resulting particles are almost entirely sheet-like with few fibers present. Cross-sectional scanning electron micrographs revel that the membranes are of uniform thickness with a continuous pore network through the material (Fig. 1, Appendix D). SDC fibrous particles show a homogeneous, but wide distribution of pores (Fig. 1c), where pore size and distribution on the membrane surface and its cross-section are similar, as seen from Figs. 1 and 1-Appendix D. On the contrary, NS particles tend to assemble in a specific directional way, in which the nano-sheets are parallel to the membrane surface (Fig. 2). This organization creates a homogeneous, wide-pore distribution in the x-y direction (parallel to the membrane) but not in the z direction (perpendicular to the membrane), leading to a surface more porous than the compact cross-section. SEM images reveals that combination of fibers and nano-sheets in the mixed-morphology create a disrupted pore network in all directions with, however, a narrow distribution (Fig. 1f).

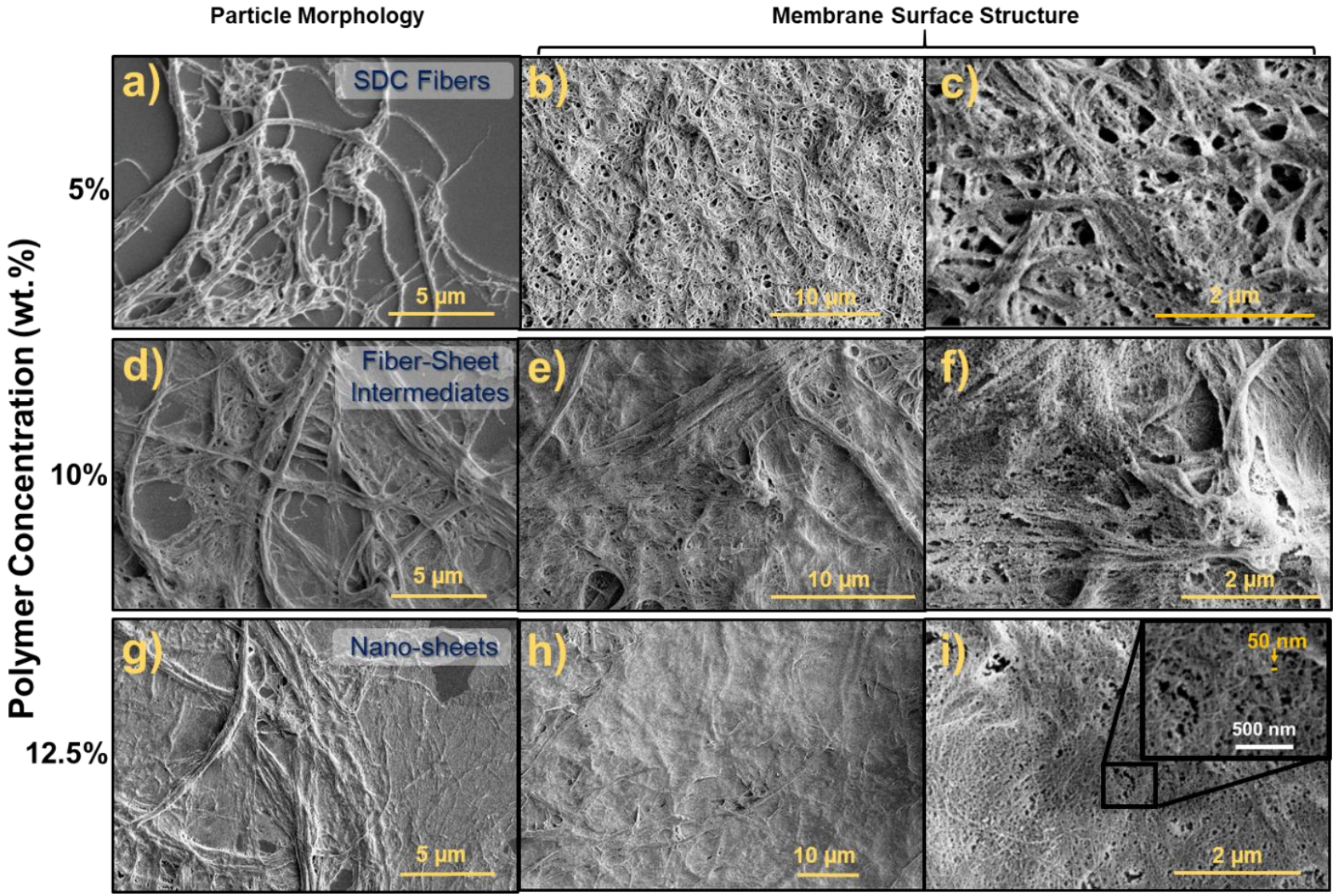

Figure 1. SEM images of particles and the surface features of membranes showing variation in particle morphologies, and membrane features at different magnifications of SDC fibrous (a, b, c), fibrous-NS intermediates (d, e, f) and NS membranes (g, h, i).

The morphology transition is possibly a result of the increase in polymer solution viscosity requiring more energy for droplet deformation by the nonsolvent while maintaining a similar rate of polymer precipitation, resulting in the exfoliation of thin sheets at the solvent-nonsolvent interface. Regardless of the morphology of the resulting particulates, the PVDF suspensions can be filtered to form porous membranes with different thicknesses (15 µm minimum).

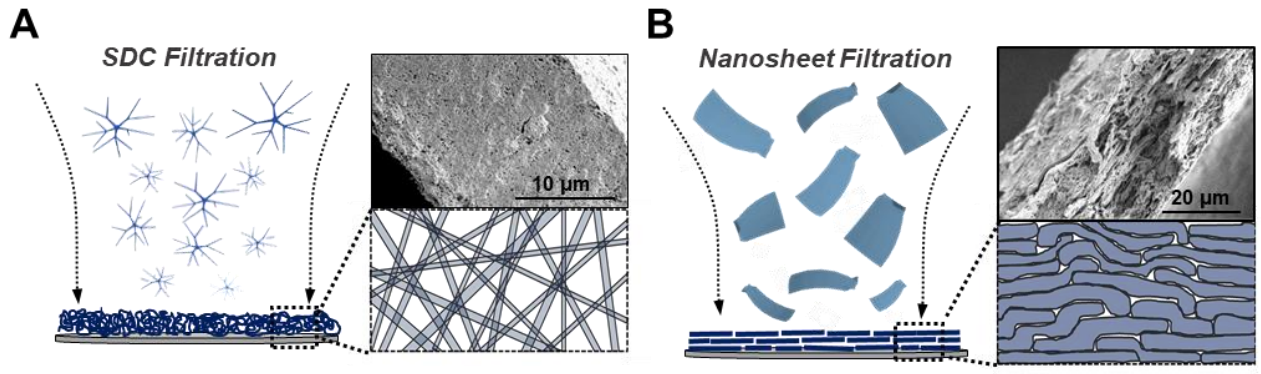

Figure 2. SEM of membrane cross-sections and schematic of the formation of (a) fibrous SDC membranes at 5 wt.% PVDF in DMSO, and (b) the formation of NS membranes at 12.5 wt.% PVDF in DMSO following solution injection into a turbulent EtOH flow.

Thermal Stability

The PVDF SDC membranes showed 5.1% shrinkage after being exposed to air in an oven at 90°C for 1 hour (5% shrinkage in Machine Direction for Celgard® 2500). The shrinkage measured at temperatures of 130°C and 150°C was 8.5% and 16.2%, respectively. The results shown in Figure 2-Appendix D indicate that the membranes are stable at high temperatures (no wrinkles or folding) and the shrinkage is within battery operation guidelines (5% at 90°C for 1 hour) [40]. Similar membranes composed of layered nanofibers of materials of differing melting temperatures have been utilized as active shutdown materials with the low-melting point layer serving as a sacrificial, pore-filling material [41–44]. While SDCs membranes may be suitable for this purpose, we did not investigate layered separators in this study.

Mechanical Properties

A typical stress-strain curve of a PVDF SDC fibrous-NS mixed-morphology shown in Figure 3 indicates mechanical properties similar to those displayed by electrospun mats with elastic response and brittle fracture [10]. The elastic modulus of the material was 347 MPa, with >30% strain before fracture and just 0.7% offset at 1000 psi (Yield stress is 5 MPa), which indicates these membranes are suitable for roll-to-roll manufacturing. We established that as the concentration of PVDF in the injection solution increases, the elastic modulus, tensile strength, and elongation at break of the resulting membranes increase (Fig. 3b), indicating that the membranes with more sheet-like particle morphology are more mechanically robust than those with fibrous morphology.

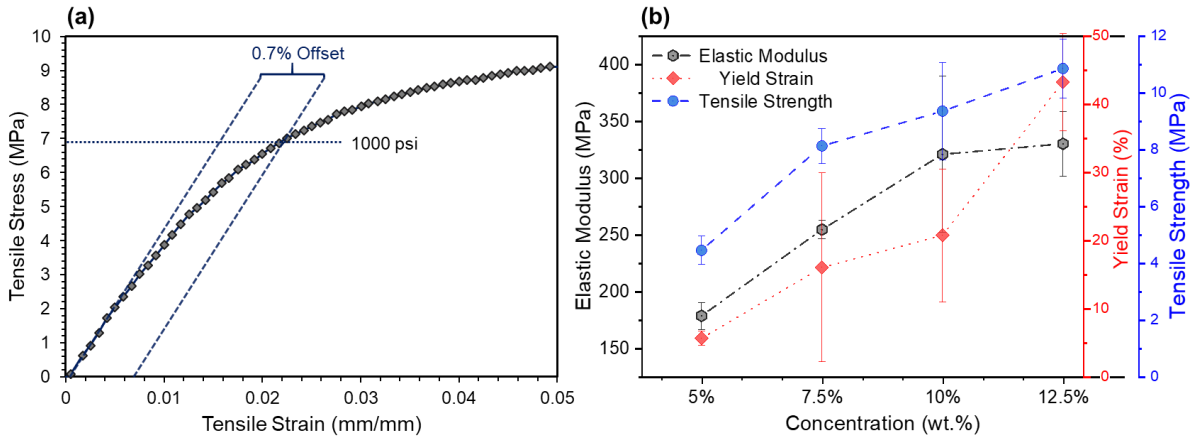

Figure 3. Mechanical properties of PVDF SDC membranes. (a) Stress-strain curve of a 48-µm thick PVDF SDC membrane. (b) Elastic modulus, elongation at break, and tensile strength of PVDF SDC membranes dependent on the concentration of the injection solution for particle formation.

The porosity of the SDC membranes is 70-80% (Table 2). This range of porosity is higher than commercially available microporous battery separators (Celgard® 2500 porosity is 55%) and is sufficient for obtaining a high electrolyte uptake and ionic conductivity while retaining mechanical integrity of the separator. Table 1 shows results for average pore size and heterogeneity of pore sizes for the SDC membranes. While it is often found in the literature that a small pore size

is preferable for electrochemical performance, we noticed that the heterogeneity of pore sizes (hence the pore-size distribution) also plays an important role. In particular, SDC fibrous membranes show the lowest pore size, but their pore-size distribution is wide (Heterogeneity index (HG)=1.42); their conductivity is the highest among the three morphologies, and cells built with SDC fibrous membranes retain a higher capacity during cycling, as discussed later. The NS morphology membranes show a higher average pore size but a comparable distribution with a HG index equal to 1.49. Indeed, their electrochemical performance is slightly lower than the fibrous morphology. The mixed-morphology membranes show a high average pore size and a narrow distribution, which seems to be detrimental for battery performance.

Table 1. Number-average pore size (Pn), weight-average pore size (Pw), and heterogeneity index (HG= Mw/Mn) of PVDF SDC membranes.

Morphology	**P_n (nm)**	**P_w (nm)**	**HG**
SDC Fibrous	233	331	1.42
SDC Fibrous-NS	451	555	1.12
NS	286	426	1.49

Electrochemical Performance

We observed that the fibers swell after imbibing the mat with liquid electrolyte. This is line with PVDF-electrolyte interactions we reported in a previous work (30). The electrolyte uptake of 5% PVDF membrane samples was as much as 325%. The lower the fiber content in the membranes, the lower was the uptake at approximately the same porosity. The reason may be attributed to the absorption of electrolyte in the outer surface of the fibers and in the higher surface area of the fibrous membranes compared to the sheet-based membranes (Table 2) [30]. The ionic

conductivity of PVDF SDC membranes is also dependent on the concentration of PVDF in the injection solution (which modifies the morphology) as shown in Table 2.

Table 2. Thickness and conductivity of PVDF SDC membranes from particles prepared at differing injection solution concentrations.

Initial PVDF Concentration (wt.%)	**Porosity (%)**	**Electrolyte Uptake (%)**	**Conductivity (mS/cm)**
5% (Fibrous)	78	325	1.21
7.5% (Fibrous)	77	250	0.78
10% (Fibrous-NS)	67	234	0.51
12.5% (NS)	76	238	0.56
Celgard®	55	70	0.94

As with electrolyte uptake, the hierarchically fibrous morphology enhances the resulting membrane conductivity. This is due to a higher surface area (and, speculatively, a greater fraction of amorphous phase [30]) of the fibrous mats compared to the NS structure, which leads to a higher electrolyte uptake (Table 2). The conductivity of SDC membranes is comparable to the commercial Celgard® membranes. At low temperatures, Celgard® has a slightly higher conductivity (except membranes with 5% initial PVDF concentration), but PVDF SDC and Celgard® have comparable conductivities at temperatures above 60 ºC, with PVDF showing stability up to 150 ºC, with a conductivity of 1 mS/cm (Fig. 4). We recognize at high temperatures (>90 ºC), there is most likely a two-phase mixture within the coin cell. However, none of the cells lost their seal. We are also aware that typical batteries are not run at these high temperatures, but nonetheless these data help develop a better understanding of the SDC membranes.

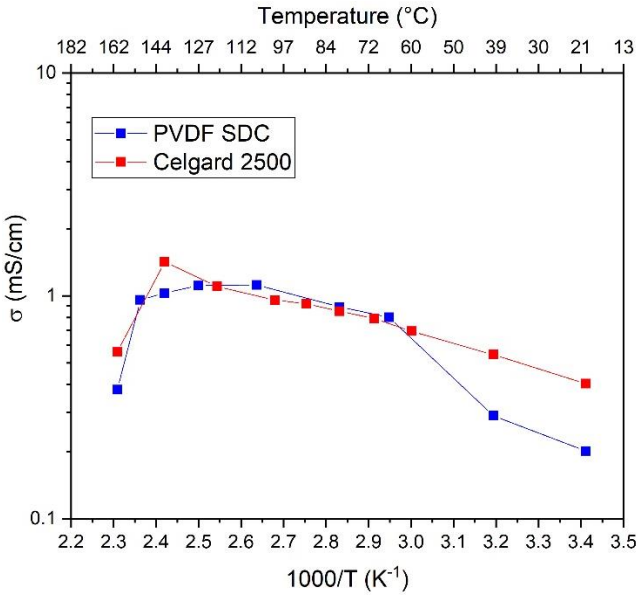

Figure 4. Conductivity at different temperatures of PVDF SDC fibrous-NS membranes and Celgard® 2500.

The electrochemical stability of the SDC membranes was assessed by measuring the potential at which a current of 10 μA/cm^2 was observed in a cell containing stainless steel electrodes (Fig. 3, Appendix D) [45]. Although Celgard® has a higher oxidation limit (5 V), the limit for the PVDF SDC membranes (4.5 V) is sufficient to be compatible with most of the common materials used for lithium battery cathodes [46, 47].

Charge-discharge curves were obtained using the SDC separators in Li/$LiCoO_2$ coin cells. The first-cycle capacity was obtained at a C/20 discharge rate (Fig. 5a). With all separator morphologies, PVDF SDC membranes showed a capacity similar or superior to Celgard® separators in the first cycle, with NS membranes showing a capacity of 112 mAh/g. Charge-discharge curves show that the cells containing fibrous PVDF SDC morphology have the highest capacity for each rate of discharge cycling (Fig. 5); however, these values are not significantly higher than those of cells containing separators with fibrous-NS or NS morphologies. The difference in capacity fade between cells containing separators with different morphologies

increases at rates higher than C/2. For example, cells containing SDC fibrous-NS separators show a significant capacity loss when switching from C/2 to 1C rate, and the loss increases with each subsequent cycle at 1C (Fig. 5).

A range of pore sizes is always present in nonwoven separators. The SDC membranes with largest pores and narrowest distribution among the 3 morphologies (*i.e.* fibrous-NS) are less suitable as battery separators (Table 1). However, based upon the observations made with the SDC membranes with various morphologies, membranes with only small pores tend to have high resistance to the flow of liquids or ions; in this case small pores are mainly created by nanofibers, which weaken the web. The combined effect of large pores for strength and openness from microfibers scaffolding, the small average pore size from a nanofiber net, and the high number of pores for a high-porosity membrane provide a superior structure for a Li-ion battery separator [48].

PVDF SDC separators and Celgard® have a similar rate capability (max charge/discharge rate) up to 1C rate, and the capacity loss is <5% after cycling through C/10 to 1C. A major benefit of PVDF SDC membranes is the simple chemical composition and production process. By creating the right particle morphology of one single polymer, we are able to create a battery separator whose properties are similar or superior to commercial separators, which usually require additives or surfactants to increase their affinity with liquid electrolytes [8].

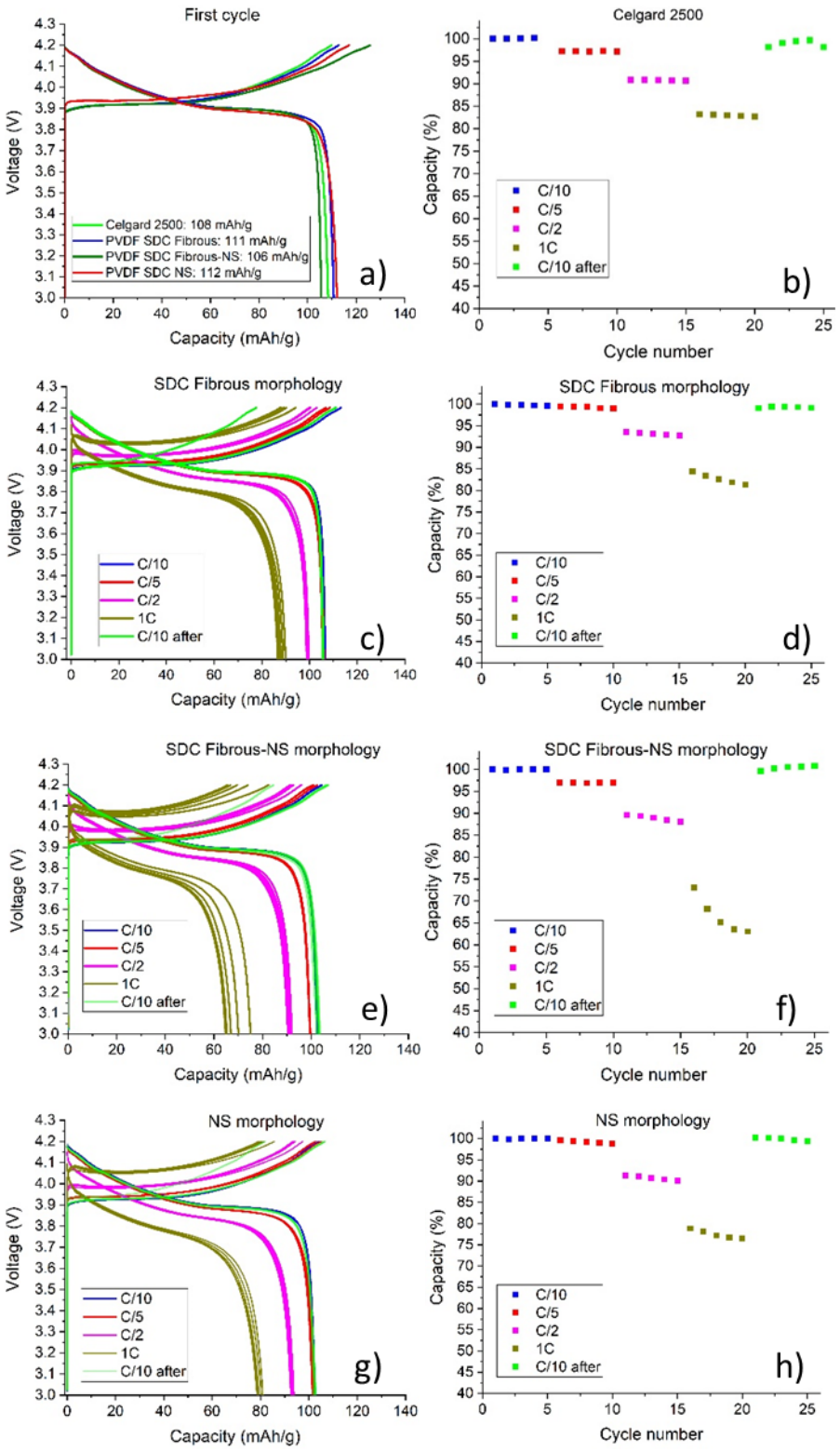

Figure 5. First cycle capacity of Celgard® and PVDF SDCs membranes (a), charge-discharge curves and rate capability of cells containing Celgard® (b), PVDF SDC fibrous (c,d), fibrous-NS (e,f), and NS membrane separators (g,h).

To determine if these separators were capable of repeated cyclic use, 50 charge/discharge cycles were performed with cells containing PVDF SDC fibrous-NS (Fig. 6). Following 50 cycles of charge/discharge at a C/5 rate, the capacity of the cell decreased by ~10%, while the coulombic efficiency is higher than 95%, which is comparable to Celgard® (~1% capacity fade, 99% efficiency). This resiliency indicates that PVDF SDC membranes have long term chemical and electrochemical stability and can resist after 50 charge-recharge cycles.

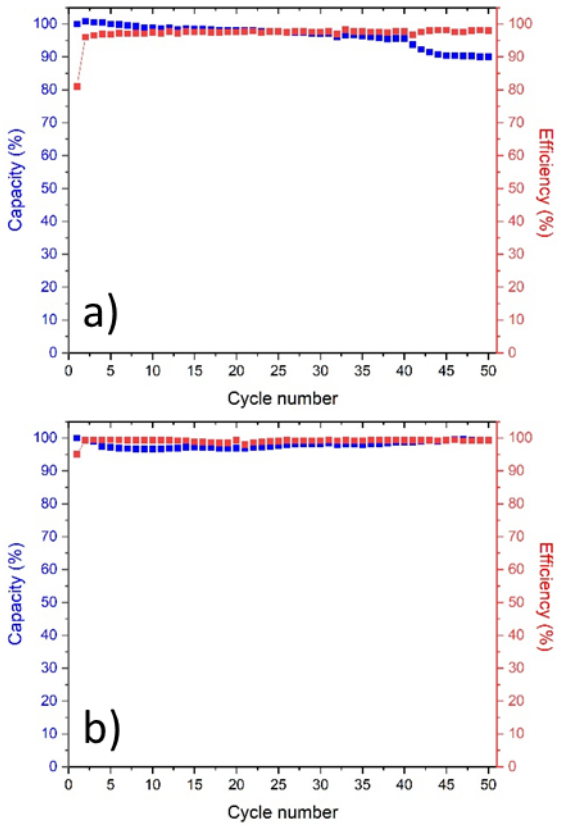

Figure 6. 50 Charge-discharge cycles of PVDF SDC fibrous-NS membrane separator (a) and Celgard (b) at C/5 rate in a Li/$LiCoO_2$ cell with 1M $LiPF_6$ in EC/DMC 1:1 %wt.

The three different morphologies of SDC membranes have advantages in different properties. SDC fibrous morphology (obtained with a low PVDF concentration in injection solutions) have small mean-pore size, high surface area, high electrolyte uptake, and high rate capability. The closer the particles are to fibrous morphology, the lower the mean pore size is, but

the pore distribution is wider. The heterogeneity of pore sizes creates strong and highly-performing membranes, with high electrolyte uptake and conductivity. Even though the SDC fibrous mats showed the best electrochemical performance, all morphologies showed performance comparable to Celgard®.

Conclusions

Shear-driven polymer precipitation offers a new method of producing porous membranes. This method could be conveniently and efficiently adapted for producing battery separators not only because of the scalability of the process, but also the versatility by which nanofibrous and sheet-like particles can be produced from a variety of polymers. The ability to produce these extremely high aspect ratio particles from different polymers allows the facile formation of membranes with a network of fibers or sheets tortuous enough for high electrochemical stability in LIBs, but also porous enough for high conductivity. The cells containing fibrous membranes (low initial PVDF concentration) showed a high conductivity, high capacity, and high maximum charging rate, while the sheet-like membranes showed better mechanical properties. The morphology of the membranes determines the performance and can be adjusted to the specific application, *e.g.* by layering or mixing the two distinct morphology particles. The versatility of the process allows for multiple polymer precipitation and for incorporation of additives such as ceramic particles, for composite separators. However, we've shown that even with one single component the structure of the pore network is the key factor in making these membranes competitive LIB separators.

References

[1] Tarascon J., Armand M., "Issues and challenges facing rechargeable lithium batteries", *Nature,* 414, 359–367, 2001.

[2] Yang M., Hou J. ,"Membranes in lithium ion batteries", *Membranes,* 2(3), 367–383, 2012.

[3] Pillot, C., "The Rechargeable Battery Market and Main Trends 2017- 2025", *Avicenne Energy,* 2018.

[4] Lagadec M.F., Zahn R., Wood V., "Characterization and performance evaluation of lithium-ion battery separators", *Nat Energy,* 4, 16–25, 2019.

[5] Deimede V., Elmasides C., "Separators for Lithium-Ion Batteries: A Review on the Production Processes and Recent Developments", *Energy Technol,* 3(5):453–68, 2015.

[6] Costa C.M., Lee Y.H., Kim J.H., Lee S.Y., Lanceros-Méndez S., "Recent advances on separator membranes for lithium-ion battery applications: From porous membranes to solid electrolytes", *Energy Storage Mater.,* 22,346–375, 2019.

[5] Luiso S., Fedkiw P.S., "Lithium-ion battery separators: Recent developments and state of art", *Curr Opin Electrochem,* 20, 99–107, 2020.

[6] Abraham K.M., Alamgir M., Hoffman D.K., "Polymer Electrolytes Reinforced by Celgard® Membranes", *J Electrochem Soc.,* 142(3):683, 1995.

[7] Heidari A.A., Mahdavi H., "Recent Development of Polyolefin-Based Microporous Separators for Li−Ion Batteries: A Review", *Chem Rec.,* 20, 570-595, 2020.

[8] Li Y., Li Q., Tan Z. "A review of electrospun nanofiber-based separators for rechargeable lithium-ion batteries", *J Power Sources,* 443, 227262, 2019.

[9] Song K., Zhang P., Huang,Y., "Electrospun PU/PVP/GO Separator for Li-ion Batteries", *Fibers Polym,* 20, 961–965, 2019.

[10] Liang Z., Zhao Y., Li Y. “Electrospun Core-Shell Nanofiber as Separator for Lithium-Ion Batteries with High Performance and Improved Safety”, *Energies,* 12, 3391, 2019

[11] Wang L., Wang Z., Sun Y., Liang X., Xiang H., “Sb_2O_3 modified PVDF-CTFE electrospun fibrous membrane as a safe lithium-ion battery separator”, *J Memb Sci.,*572, 512–519, 2019.

[12] Shekarian E., Nasr M.R.J., Mohammadi T., Bakhtiari O., Javanbakht M., “Enhanced Wettability and Electrolyte Uptake of Coated Commercial Polypropylene Separators with Inorganic Nanopowders for Application in Lithium-ion Battery”, *J Nanostruct.*, 9(4): 736–750, 2019.

[13] Lee H., Alcoutlabi M., Toprakci O., “Preparation and characterization of electrospun nanofiber-coated membrane separators for lithium-ion batteries”, *J Solid State Electrochem,* 18, 2451–2458, 2014.

[14] Yang C., Jia Z., Guan Z., Wang L. “Polyvinylidene fluoride membrane by novel electrospinning system for separator of Li-ion batteries”, *J Power Sources,* 189(1), 716–720, 2009.

[15] Pan J.L., Zhang Z., Zhang H., Zhu P.P., Wei J.C., Cai J.X., Yu J., Koratkar N., Yang Z.Y. “Ultrathin and Strong Electrospun Porous Fiber Separator”, *ACS Appl Energy Mater,* 1, 9, 4794–4803, 2018.

[16] Zhu Y., Yin M., Liu H., Na B., Lv R, Wang B, Huang Y. “Modification and characterization of electrospun poly (vinylidene fluoride)/poly (acrylonitrile) blend separator membranes”, *Compos Part B Eng,* 112, 31–37, 2017.

[17] Barbosa J.C., Dias J.P., Lanceros-Méndez S., Costa C.M., “Recent advances in poly(Vinylidene fluoride) and its copolymers for lithium-ion battery separators”, *Membranes,* 8, 45, 2018.

[18] Choi S.S., Lee Y.S., Joo C.W., Lee S.G., Park J.K., Han K.S., "Electrospun PVDF nanofiber web as polymer electrolyte or separator", *Electrochim Acta*, 50(2–3), 339–343, 2004.

[19] Waqas M., Ali S., Feng C., Chen D., Han J., He W., "Recent Development in Separators for High-Temperature Lithium-Ion Batteries" *Small*, 15, 1901689, 2019.

[20] Bicy K., Suriyakumar S., Anu Paul P., Anu A.S., Kalarikkal N., Stephen A.M., Geethamma V.G., Rouxel D., Thomas S., "Highly lithium ion conductive, Al_2O_3 decorated electrospun P(VDF-TrFE) membranes for lithium ion battery separators", *New J. Chem.*, 42, 19505-19520, 2018.

[21] Yang S., Ma W., Wang A., Gu J., Yin Y., "A core-shell structured polyacrylonitrile@poly(vinylidene fluoride-hexafluoro propylene) microfiber complex membrane as a separator by co-axial electrospinning", *RSC Adv.*, 8, 23390-23396, 2018.

[22] Boateng B., Zhu G., Lv W., Chen D., Feng C., Waqas M., Ali S., Wen K., He W., "An Efficient, Scalable Route to Robust PVDF-co-HFP/SiO_2 Separator for Long-Cycle Lithium Ion Batteries", *Phys. Status Solidi RRL*, 12, 1800319, 2018.

[23] Xiang Y., Zhu W., Qiu W., Guo W., Lei J., Liu D., Qu D., Xie Z., Tang H., Li J., "SnO_2 Functionalized Polyethylene Separator with Enhanced Thermal Stability for High Performance Lithium Ion Battery", *ChemistrySelect*, 3, 911–916, 2018.

[24] Gao H., Chen Y., Sun H., Zhao A., Wang L., Liu N., "Silicone modified polypropylene separator for high temperature lithium ion battery applications", *Mater. Res. Express*, 5, 065512, 2018.

[25] Chao C.Y., Feng Y.F., Hua K., Li H., Wu L.J., Zhou Y.S., Dong Z.W., "Enhanced wettability and thermal stability of polypropylene separators by organic–inorganic coating layer for lithium-ion batteries", *J Appl Polym Sci*, 135(28), 46478, 2018.

[26] Herle S.P., Gordon J.G., “Ceramic coating on battery separators”, *US Patent 10193116B2*, Washington, DC: U.S. Patent and Trademark Office, 2019.

[27] Han Y., Ye L., Boateng B., Sun Q., Zhen C., Chen N., Shi X., Dickerson J.H., Li X., He W., “Direct electrophoretic deposition of an ultra-strong separator on an anode in a surfactant-free colloidal system for lithium ion batteries”, *J. Mater. Chem. A*, 7, 1410-1417, 2019.

[28] Luiso S., Henry J.J., Pourdeyhimi B., Fedkiw P.S., “Fabrication and Characterization of Meltblown Poly(vinylidene difluoride) Membranes”, *ACS Appl Polym Mater*, 2, 7, 2849–2857, 2020.

[29] Luo R., Wang C., Zhang Z., Lv W., Wei Z., Zhang Y., Luo X., He W., “Three-Dimensional Nanoporous Polyethylene-Reinforced PVDF-HFP Separator Enabled by Dual-Solvent Hierarchical Gas Liberation for Ultrahigh-Rate Lithium Ion Batteries”, *ACS Appl Energy Mater*, 1, 3, 921–927, 2018.

[30] Liu J., Shi X., Boateng B., Han Y., Chen D., He W., “A Highly Stable Separator from an Instantly Reformed Gel with Direct Post-Solidation for Long-Cycle High-Rate Lithium-Ion Batteries”, *ChemSusChem*, 12, 908 –914, 2019.

[31] Ye L., Shi X., Zhang Z., Liu J., Jian X., Waqas M., He W., “An Efficient Route to Polymeric Electrolyte Membranes with Interparticle Chain Microstructure Toward High-Temperature Lithium-Ion Batteries”, *Adv Mater Interfaces*, 4, 1601236, 2017.

[32] Liu B., Huang Y., Zhao L., Huang Y., Song A., Lin Y., Wang M., Li X., Cao H., “A novel non-woven fabric supported gel polymer electrolyte based on poly(methylmethacrylate-polyhedral oligomeric silsesquioxane) by phase inversion method for lithium ion batteries”, *J Memb Sci*, 564, 62-72, 2018.

[33] Velev O.D., Smoukov S., Geisen P., Wright M.C., Gangwal S., "Method for Fabricating Nanofibers", *US Patent No. 9,217,211(B2)*, Washington, DC: U.S. Patent and Trademark Office, 2015.

[34] Velev O.D., Smoukov S., Marquez M. "Nanospinning of polymer fibers from sheared solutions", *US Patent No.8,551,378*, Washington, DC: U.S. Patent and Trademark Office, 2013.

[35] Velev O.D., Roh S. "Fractal-like polymeric particles and their use in diverse applications", *WIPO Patent Application No. 2017196864(A1)*, 2017.

[36] Roh S., Williams A.H., Bang R.S., Stoyanov S.D., Velev O.D., "Soft dendritic microparticles with unusual adhesion and structuring properties", *Nature Materials*, 18, 1315–1320, 2019.

[37] Painter P.C., Coleman M.M., "Essentials of Polymer Science and Engineering", Lancaster, *Pa: DEStech*, 2009.

[38] Lee H., Yanilmaz M., Toprakci O., Fu K., Zhang X., "A review of recent developments in membrane separators for rechargeable lithium-ion batteries", *Energy Environ. Sci.*, 7, 3857-3886, 2014.

[39] Shi C., Zhang P., Huang S., He X., Yang P., Wu D., Sun D., Zhao J., "Functional separator consisted of polyimide nonwoven fabrics and polyethylene coating layer for lithium-ion batteries", *J Power Sources*, 298, 158–165,2015.

[40] Li Z., Xiong Y., Sun S., Zhang L., Li S., Liu X., Xu Z., Xu S., "Tri-layer nonwoven membrane with shutdown property and high robustness as a high-safety lithium ion battery separator", *J Memb Sci.*, 565, 50–60, 2018.

[41] Li Y., Pu H., "Facile fabrication of multilayer separators for lithium-ion battery via multilayer coextrusion and thermal induced phase separation", *J Power Sources*, 384, 408–416, 2018.

[42] Li Y., Pu H., Wei Y. “Polypropylene/polyethylene multilayer separators with enhanced thermal stability for lithium-ion battery via multilayer coextrusion”, *Electrochim Acta*, 264, 140–149, 2018.

[43] Choe H.S., Carroll B.G., Pasquariello D.M., Abraham K.M., “Characterization of Some Polyacrylonitrile-Based Electrolytes”, *Chem Mater*, 9, 1, 369–379, 1997.

[44] Li X., Cheruvally G., Kim J.K., Choi J.W., Ahn J.H., Kim K.W., Ahn H.J., “Polymer electrolytes based on an electrospun poly(vinylidene fluoride-co-hexafluoropropylene) membrane for lithium batteries”, *J Power Sources*, 167(2), 491–498, 2007.

[45] Cheruvally G., Kim J.K., Choi J.W., Ahn J.H., Shin Y.J., Manuel J., Raghavan P., Kim K.W., Ahn H.J., Choi D.S., Song C.E., “Electrospun polymer membrane activated with room temperature ionic liquid: Novel polymer electrolytes for lithium batteries”, *J Power Sources*, 172(2), 863–869, 2007.

[46] Brinson A., “Dreamweaver GoldTM brochure”, 2019. Accessed on 09/20/2020 at https://www.dreamweaverintl.com/uploads/5/7/8/8/57886015/dwi_brochure-_gold_170419.pdf

CHAPTER 6: An Optimal Structure for Li-Ion Battery Fiber-based Separators

Abstract

Lithium-ion battery separators are receiving increased consideration from the scientific community, but challenges remain on designing a structure that maximizes electrochemical properties, such as ionic conductivity and in-use cell discharge capacity and rate capability. While the trend of creating high-performing fiber-based or fibrous battery separators has moved toward achieving a small and uniform pore size, similar to well-established microporous membrane separators, we show here that not only the pore size but also the pore-size distribution has a pronounced effect on these electrochemical properties. This study compares nonwoven membranes with different pore sizes and distributions that are fabricated from a single polymer, poly(vinylidene fluoride) (PVDF), using three different techniques (meltblowing, electrospinning, and shear-spinning). We evaluate their performance as a separator in a Li-ion cell. While meltblowing is commonly employed for the production of commercial micro/nanofibers, electrospinning has been studied mostly in the academic literature. Shear-spinning is a new and novel method of fabricating nanofibrous material where, for this study, the morphology of the resulting PVDF membranes may be controlled from fibrous-like to nano-sheet-like with subsequent effects on the electrochemical properties. By comparing PVDF separators made with the same fabrication technique, we show that the smaller is the pore size and the wider the pore-size distribution the higher are the electrolyte uptake and ionic conductivity of the mats, resulting in improved in-use discharge capacity and rate capability in Li/$LiCoO_2$ cells.

Introduction

Lithium-ion battery (LIB) separators are one of the main components of a battery, but their chemical and electrochemical properties have been a subject of limited investigations relative to

the other constituents of the cell. Different raw materials, combinations thereof, and manufacturing processes for separators have attracted the attention of most literature studies [1–7]. Among them, several reports showed correlations between structural properties of separators, such as pore size and thickness, and electrochemical properties, such as electrolyte uptake/ionic conductivity of the membranes and discharge capacity/rate capability of Li cells assembled with those separators [5,8–12]. However, these were single-case studies, and few focused on understanding the role of the separator pore network and its relation to its electrochemical properties. In this research, we focus on analyzing the relationships between the pore structure of poly(vinylidene fluoride) (PVDF)-based membranes made with different processes to their in-use electrochemical properties, such as discharge capacity and rate capability of a Li-ion cell.

The relationships between structural and electrochemical properties of battery separators have recently attracted the attention of the scientific community. Hierarchically-structured separators were prepared by Luo *et al.* [13] through a solvent liberation method and by Liu *et al.* [14] through a reformed gel with direct post-solidation procedure. By exploiting the difference in solvent evaporation rate between N-methyl pyrrolidone and acetone, both groups created separators with high porosity with resulting high ionic conductivity after electrolyte uptake. The authors claim that the inter-island and inner-bound structures of the separators cause low capacity loss in a $LiFePO_4$/Li cell. Ye *et al.* [15] fabricated separators with a highly-dense and porous inter-particle chain structure. The rearrangement of the polymer chains after electrolyte uptake is reported to create a microstructure that decreases thermal shrinkage and improves electrochemical properties. Different separator morphologies, such as sponge-like material with asymmetric distribution of pores [17], may be obtained not only with solvent-nonsolvent interactions [5,13,16], but also by changing the conditions used in the separator fabrication processes [7,12].

Fibrous separators have been widely studied because their pore structure allows high electrolyte wettability, ionic conductivity, and cell-cycling performance [6,18,19]. Nano-structured fibrous battery separators are attractive because of their controllable compositions and pore structures. A fibrous network forms an interconnected nano- and microporous structure that provides both openness for enhanced lithium-ion transport and mechanical strength for cell assembly. While the trend of creating a fibrous battery separator have largely sought to achieve a pore size and distribution similar to well-established microporous membranes, *i.e.*, small and uniform pore size, a few outlier studies [20-24] suggest that a small pore size and a high porosity (reported as responsible for improved cycling performance in nonwovens) do not capture the effect that pore-size distribution has on the electrochemical properties. Lee *et al.* [20] reported the importance of correlating the separator pore structure to the electrochemical properties. The authors relate the ionic conductance and the rate capability ($Li/LiMnO_4$ cells) to the normalized Gurley number [25], which in turn they relate to thickness and porosity. However, these correlations do not uniquely specify the electrochemical performance of fibrous-based separators, as other factors, such as pore-size distribution, must be considered. Ye *et al.* [21] decorated the surface of electrospun polyimide nanofibers with polyaniline to create a 3D hierarchical micro/nano-architecture. The presence of the so-called polyaniline nanowires decreased the average pore size, but also increased the electrolyte uptake, resulting in an improved conductivity and cell-cycling performance. Sabetzadeh *et al.* [22] showed that an increased battery performance can be achieved when multi-scale porosity of the separator is present. These researchers introduced nanoporosity by means of phase separation in electrospun fibers, which increased conductivity and in-use capacity retention in a $Li(Ni_{1/3}Co_{1/3}Mn_{1/3})O_2/Li$ cell. A wide pore-size distribution is regarded as an improvement also by Jiang *et al.* [23], who introduced TiO_2 nanotubes in a

poly(vinylpyrrolidone) matrix. After a treatment at 500 °C, the separator presented nano- and meso-pores with a broad distribution, which improved ionic conductivity and battery cycling. A small average pore size is not sufficient to improve the electrochemical properties of LIB separators, and a broad pore distribution seems to have a beneficial effect. Zhai *et al.* [24] show that a tri-layered poly(m-phenylene isophthalamide) (PMIA)/PVDF/PMIA composite separator with a mean pore size of 0.85 μm (range 0.71-2.41μm) has superior conductivity, tensile strength, and cycling performance compared to single-layer PVDF (mean pore size=2.50 μm, range 2.09-3.18 μm) or PMIA (mean pore size=0.53 μm, range 0.51-0.57 μm). A small mean pore size and a wide pore size distribution seem to be necessary for a high-performing LIB separator.

In this study, we compare membranes with different pore sizes and distributions that are fabricated with a single polymer, PVDF, using three different techniques (meltblowing, electrospinning, and shear-spinning), and we evaluate their performance as separators in $Li/LiCoO_2$ cell. Meltblowing is a process commonly employed for the production of commercial micro/nanofibers where the melted polymer is extruded through a die with fine capillaries, after which a jet of hot air impinges on the emerging polymer filaments to form fibrous webs. In a previous work, we demonstrated the feasibility of meltblowing PVDF and using the resulting webs as a battery separator [7,12]. Electrospinning has been widely used as a method to prepare a wide variety of functional fibrous membranes through the use of an electrical force. Shear-spinning is a novel method of fabricating nanofibrous material in which a polymer solution is injected into a sheared nonsolvent flow to create soft dendritic colloid (SDC) particles of various morphologies [26–28]. In a previous study [5], we showed that the morphology of PVDF membranes prepared by the shear-spinning technique may be controlled from fibrous to nano-sheet, with subsequent effects on the electrochemical properties. Here, we show that for PVDF separators made with these

three processes, a decrease in pore size and a widening of pore-size distribution in separators made with the same process result in higher electrolyte uptake and ionic conductivity of the mats, and higher discharge capacity and rate capability in-use in Li/$LiCoO_2$ cells.

Experimental

Melblowing process

For meltblowing, we used an experimental grade of PVDF Kynar® resin RC 10,287 (Arkema, Inc.). The resin has low molecular weight (MW) (15 – 100 kDa), melt viscosity of 0.2 kP at 230° C at a shear rate of 100 s^{-1}, and a 2.0 poly-dispersity index (PDI) [12,29,30]. After drying the resin overnight at 70 ºC, we prepared meltblown mats using a 1.2-m Reifenhauser-Reicofil Meltblown Pilot Line at the Nonwovens Institute at NC State University [31]. Based on our previous work [7,12], the temperatures of both the die and the impinging air jets were kept at 240 ºC and samples were fabricated at a basis weight (BW) of 40 g/m^2 with the following process variables (The designation M1, M2, and M3 are abbreviations for these conditions and referenced in the Results and Discussion section):

M1. Throughput=46 kg h^{-1}; airflow=1100 m^3 h^{-1}; die-to-collector distance (DCD)=20 cm

M2. Throughput=11 kg h^{-1}; airflow=1000 m^3 h^{-1}; DCD=15 cm

M3. Throughput=36 kg h^{-1}; airflow=1100 m^3 h^{-1}; DCD=15 cm

Electrospinning process

PVDF Kynar® resin 761 (MW=300 – 400 kDa, PDI=4.0) was obtained from Arkema and dissolved in a mixture of dimethylformamide (DMF) and acetone (7:3 v/v) at 12% or 16% concentration. We loaded the polymer solution in a 10 mL syringe with a 22-gauge needle and placed it on a precision syringe pump with a constant flow rate of 1.5 mL h^{-1}. The nanofibers were collected on aluminum foil placed on an aluminum collector plate connected to the grounded

electrode. We fabricated electrospun PVDF mats at room temperature and 55 ± 5% relative humidity with the following process variables:

E1. PVDF concentration=12 wt.%; voltage=15 kV; tip-to-collector distance (TCD)=15 cm; BW=100 g/m^2

E2. PVDF%=16 wt.%; voltage=15 kV; TCD=15 cm; BW=17 g/m^2

E3. PVDF%=12 wt.%; voltage=20 kV; TCD=10 cm; BW=150 g/m^2

High-shear precipitation process

We dissolved PVDF resin (Sigma Aldrich, MW = 530 kDa, PDI=2.0) in dimethyl sulfoxide (DMSO, Fisher Scientific) by heating at 110°C for 24 hours while stirred. After cooling, we injected the PVDF solution at a rate of 1 mL/s into the shear zone of a colloidal mill (IKA Magic Lab) set to 20,000 rpm and filled with 500 mL of ethanol, as discussed in previous publications [5,26-28]. After centrifuging the resulting PVDF soft dendritic colloids (SDC) suspensions and recovering the solid, we re-suspended the particles in ethanol and repeated the process five times to remove residual DMSO. The final suspension was filtered to form a membrane (0.45 μm filter pore size), and the resulting membranes were dried in an air oven at 70°C for 24 hours. We produced the following samples of SDC membranes with a basis weight of BW=20 g/m^2:

S1. PVDF concentration in the injection solution=5 wt.% (fibers)

S2. PVDF%=10 wt.% (fibers-nanosheets)

S3. PVDF%=12.5 wt.% (nanosheets)

Microscopy

We used a field emission scanning electron microscope (FEI Verios 460L) under a 2 kV accelerating voltage to examine the membrane morphology. We calculated the average fiber

diameters by using Fiji (ImageJ) software after taking at least 100 measurements from 5 different areas in each sample.

Thickness and Solid Volume Percent

We measured the mat thickness with a Mitutoyo micrometer and calculated the solid volume percent ε_s by using Eq. (1):

$$\varepsilon_s = \left(\frac{W}{t\rho_{fiber}} \right) \times 100 \qquad (1)$$

where W is the basis weight of the mat in g cm^{-2}, t is the thickness in cm, and ρ_{fiber} is the density of the polymer (1.78 g cm^{-3}).

Capillary flow porosimetry

We measured the pore diameter at the most constricted part of the pore (the bubble point diameter) as well as the pore-diameter distribution with an in-plane porometer (Porous Materials Inc.). A highly wetting liquid (Salwick®) with a known surface tension of 20.1 dynes cm^{-1} was used to wet the mats and no visible contact angle was detected (contact angle=0º). The pore diameter was calculated with the Young–Laplace equation [32]: $D = 4\gamma_{L/G} \cos\theta / p$, where p is the extrusion pressure in MPa, D is the pore diameter in mm, $\gamma_{L/G}$ is the surface tension of Salwick® in N/mm, and θ is the contact angle of Salwick® with the sample.

Electrolyte uptake

All PVDF mats absorbed electrolyte quickly (<1 s) and electrolyte uptake was calculated with Eq. (2) by weighing the separators before and after soaking for 10 min in a 1M $LiPF_6$ ethylene carbonate (EC)/dimethyl carbonate (DMC) 1:1 v/v mixture:

$$\text{Electrolyte uptake} = \left(\frac{W_a - W_b}{W_b} \right) \times 100 \qquad (2)$$

where W_b and W_a are the weights of separator before and after soaking in the electrolyte, respectively. When soaking in electrolyte, the fibers swell and the mat undergoes volume expansion, which may vary with the density of its fibrous network. Non-uniform distribution of the fibrous morphology may cause significant variations in the uptake measurements. To reduce uncertainties and assess reproducibility, we removed the surface-bound electrolyte with wax paper and measured electrolyte uptake on at least 5 replicas.

Ionic conductivity

In an Argon-filled glove-box, we added 50 µl of 1M $LiPF_6$ in EC/DMC (1:1 v/v) to punched separators (15.9-mm diameter), which were then sandwiched between stainless steel spacers and assembled in a CR2032 coin cell. We performed electrochemical impedance spectroscopy (EIS) measurements with a Bio-Logic VMP3 16-Channel Potentiostat. The frequency sweep ranged from 500 kHz to 1 Hz with an amplitude of 10 mV. The conductivity σ was calculated with Eq. (3):

$$\sigma = \frac{t}{R_{ion}A} \qquad (3)$$

where t is the membrane thickness, R_{ion} is the measured ionic resistance (high-frequency intercept of Nyquist plot), and A is the membrane area.

Rate capability and cyclying performance.

We assembled coin cells with a $LiCoO_2$ cathode (Electrodes and More, Richardson, TX) and a Li metal anode, with 1 M $LiPF_6$ EC/DMC (1:1 v/v) and performed chronopotentiometry measurements with the VMP3 potentiostat. After conditioning the cells by cycling them between 3 V and 4.20 V at a constant rate of C/20 for 5 cycles, we cycled them at different C-rates at room temperature. We refer to these experiments in the discussion section as rate-capability measurements. Capacity is calculated as % from the first-cycle capacity, which corresponds to

100%. A minimum of 3 replicas per separator were assembled into coin cells and cycled to assess reproducibility.

Results and Discussion

Morphology, fiber and pore distributions

Fig. 1 shows SEM images of representative meltblown PVDF mats prepared under the three processing conditions employed in this study, and their normal distribution curve-fits to the fiber-diameter data. Meltblown fiber diameters have been reported to be log-normally distributed, regardless of the mean fiber diameter [33-36]. However, the presence of a few large fibers in otherwise fine fibrous samples skews the distribution and increases their relative dispersity, leading to distributions that can be better approximated with normal curve fits [37].

The fibers are smooth and featureless, but roping and entanglements of the fibers are present, especially with sample M1. The average fiber diameters are 1.7, 1.5, and 1.4 μm for samples M1, M2, and M3, respectively, with distributions spanning a few microns in all cases. In particular, sample M1 being meltblown with a high throughput and high airflow shows the widest fiber size distribution, with a standard deviation (SD) of 0.9 μm. The lower meltblowing throughput in preparation of sample M3 (compared to sample M1) produced a narrower distribution with a slight decrease of fiber diameter. If polymer throughput and air flow are not well balanced, a high instability of the melt exiting the die leads to fiber roping, entanglements, and a wide size distribution. A wide size distribution is not only easier to obtain, but it is also surprisingly beneficial for cycling stability, as we show later.

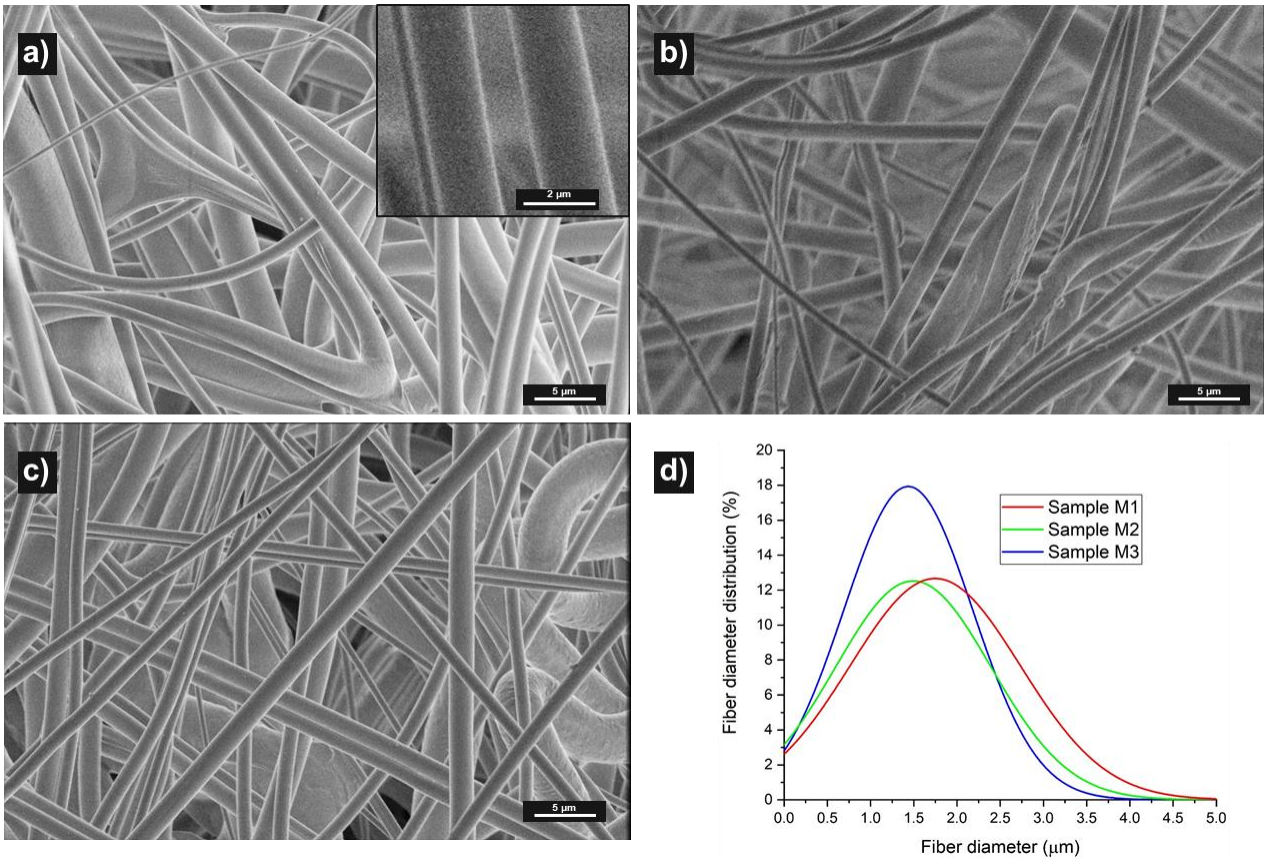

Figure 1. SEM images of meltblown PVDF sample M1 (a, with inset at higher magnification), (b) M2, (c) M3, and (d) resulting fiber diameter distribution. The distributions are well approximated as normal.

In comparison to fibers in the meltblown mats, the fibers in electrospun PVDF mats do not have as smooth a surface (Fig. 2). The rapid evaporation of solvent during electrospinning is responsible for the small features visible on the fiber surface. Electrospun fiber diameters were fit to log-normal distributions as previously described [38-39]. The average fiber diameters are typically smaller (0.25-0.50 µm) than that of meltblown samples (1.4-1.7 µm). Sample E2 showed the largest average fiber diameter among the electrospun samples (0.51 µm) with the broadest fiber size distribution. We suggest this distribution results from sample E2 having the highest PVDF concentration in the electrospinning solution and the resulting viscosity did not allow the filaments to attenuate as much as in samples E1 and E3. On the other hand, samples E1 and E3 have similar

average fiber diameters (0.26 and 0.29 μm), with sample E3 showing the narrowest distribution with only 0.08 μm standard deviation. In the electrochemical properties section below, we show that the combination of small average fiber diameter and wide diameter distribution is the most suitable structure for obtaining the highest cell-cycling stability.

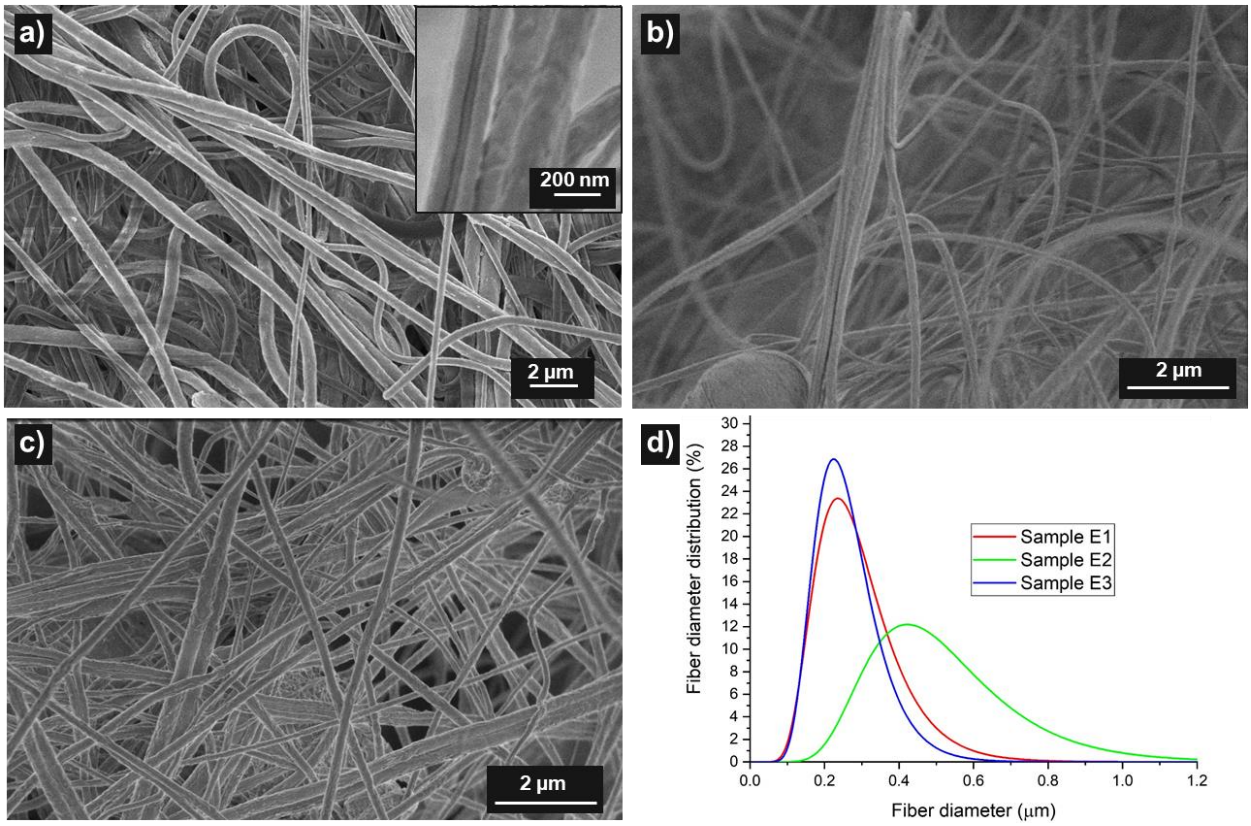

Figure 2. SEM images of electrospun PVDF sample E1 (a, with inset at higher magnification), E2 (b), and E3 (c); and resulting fiber diameter distributions (d).

We have shown in previous work [12] that pore size is proportional to fiber diameter in mats. The shear-spun mats, however, do not all display fibrous morphology as discussed in our previous study [5]. Consequently, the comparison metric we employ here is pore size measured with capillary porosimetry rather than fiber diameter. Porosimetry fails to detect some of the narrow channels connecting the pores (typical of nonwovens) or overestimates their diameter, hence we do not place confidence in porosimetry data for meltblown and electrospun mats. Shear-

spun samples, however, have a dense structure and porosimetry is an applicable technique. SDC-based membranes differ from meltblown and electrospun mats because of their densely interconnected structure, as seen in Fig. 3. The fibrous morphology is created with a low concentration (5%) of PVDF in the injection solution, which allows the SDC particles to branch out freely during formation (Fig. 3a) [5]. At higher concentration (10%), the higher solution viscosity requires more energy to deform the polymer particles, leading to a mixed fibrous/nano-sheet (NS) morphology (Fig. 3b). At 12.5% PVDF, the membranes are formed almost entirely by thin and highly porous NS particulates (Fig. 3c).

Because the size of a SDC particles is not defined by one unique dimension (as they comprise highly branched fibers, nanosheets, and mixtures thereof), the pore network may have a Gaussian, Lorentzian or a mixed distribution [40]. Here, the pore size data were fit to Lorentzian distribution curves, as shown in Fig. 3d. The SDC-based membranes have a uniform thickness with a continuous pore network, with pore sizes ranging from 10 to 500 nm. The NS particles assemble parallel to the membrane surface to create a spatially homogeneous and wide-pore distribution (full width at half maximum, FWHM=65 nm), but with an average pore size (250 nm) higher than SDC fibrous membranes (170 nm). The latter also present a broad pore distribution (FWHM=42 nm) despite the high number of pores below 200 nm. The fibrous-NS morphology membranes show a relatively narrow distribution (FWHM=22 nm) with large pore size (520 nm), probably due to a disrupted pore network caused by the combination of fibrous and nano-sheet morphologies.

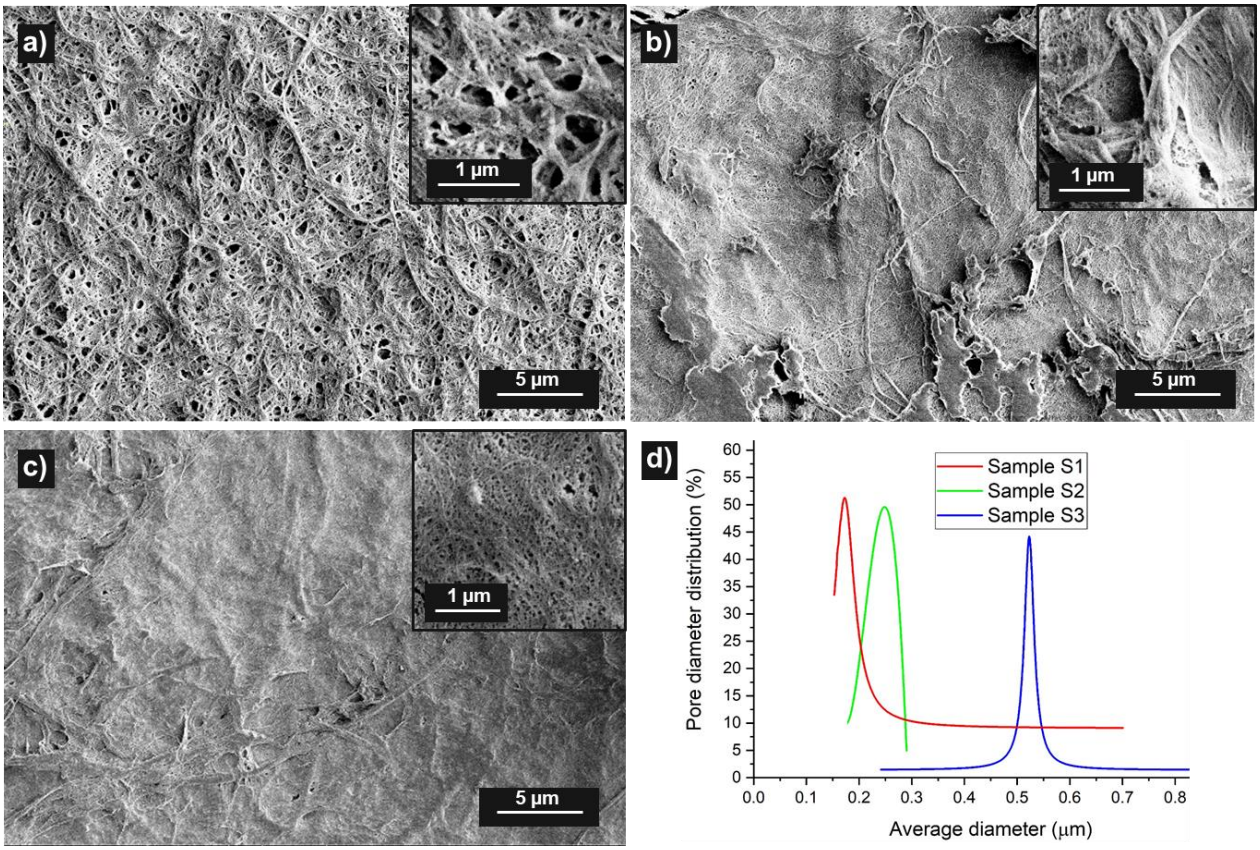

Figure 3. SEM images of SDC PVDF sample S1 (a, with inset at higher magnification), S2 (b), and S3 (c); resulting pore diameter distributions (d).

Electrochemical and mat properties

Meltblowing produces samples with the lowest solid volume percent (<20%) among the three techniques (Table 1), followed by samples from shear-spinning (23-33%). The low solid volume percent is partly responsible for the high electrolyte uptake of meltblown samples (up to 910%). In addition, absorption of electrolyte in the outer surface of the PVDF fibers plays an important role [7,12]. Because shear-spun samples have a lower basis weight but a greater thickness than electrospun samples, the solid volume fraction of electrospun and shear-spun mats are comparable. The lower the solid volume fraction of a mat, the higher is its ionic conductivity, with meltblown samples having conductivities at least four times higher than shear-spun samples. We note that the higher is the electrolyte uptake, the higher is the conductivity for each set of

separators (except sample M1, probably because the spatial non-uniformity of the fibrous network did not enable a uniform volume expansion during electrolyte uptake).

Table 1. Solid volume percent, electrolyte uptake, ionic conductivity, and thickness of PVDF separators made by meltblowing (M), electrospinning (E), and shear-spinning (S).

	M1	**M2**	**M3**	**E1**	**E2**	**E3**	**S1**	**S2**	**S3**
Solid Volume Percent	18%	16%	18%	54%	27%	37%	23%	24%	33%
Electrolyte uptake	740%	910%	705%	380%	475%	335%	325%	240%	235%
Ionic conductivity (mS/cm)	4.34	6.91	5.61	0.47	2.00	0.29	1.21	0.56	0.51
Thickness (µm)	115	175	140	110	150	200	20	23	27

Electrochemical stability of the in-use separators is assessed by cycling Li-ion cells containing the PVDF mats at different C-rates. We compared the electrochemical properties of mats fabricated with the same technique at comparable thicknesses. As shown in Fig. 4e-f, cells with meltblown sample M3 separators change in capacity with cycle number at low-discharge rate (C/10) and show significant capacity loss at higher discharge rates. Capacity retention after rate-capability measurements is poor, and the cells have low coulombic efficiencies. Sample M2 has a similar average fiber diameter compared to sample M3, but a wider diameter distribution, and shows an improved cell cycling, with higher stability at high C-rates and higher capacity retention after cycling (Fig. 4c-d).

The only significant difference between cells containing M2 and M3 samples is the fiber diameter distribution of the separators. However, initial low-rate cycling of cells with M3 shows significant capacity loss, change in capacity with cycle number, and low-coulombic efficiency. Sample M1 has the widest diameter distribution among the three-meltblown samples and provides

the best cycling performance. Fig. 4a-b show that discharge capacity values at C/10 and at C/5 rates vary less and capacity loss is reduced in cells employing meltblown separator M1 compared to cells with samples M2 and M3. According to Table 1, thickness, ionic conductivity, electrolyte uptake, and solid volume percent are similar between sample M1 and M3, and comparable with sample M2. Without other significant differences, the distribution of fiber diameters is the effective factor influencing the cell behavior during cycling. Thus, we conclude that a broader diameter distribution in the separator is advantageous for battery cycling stability [22-24].

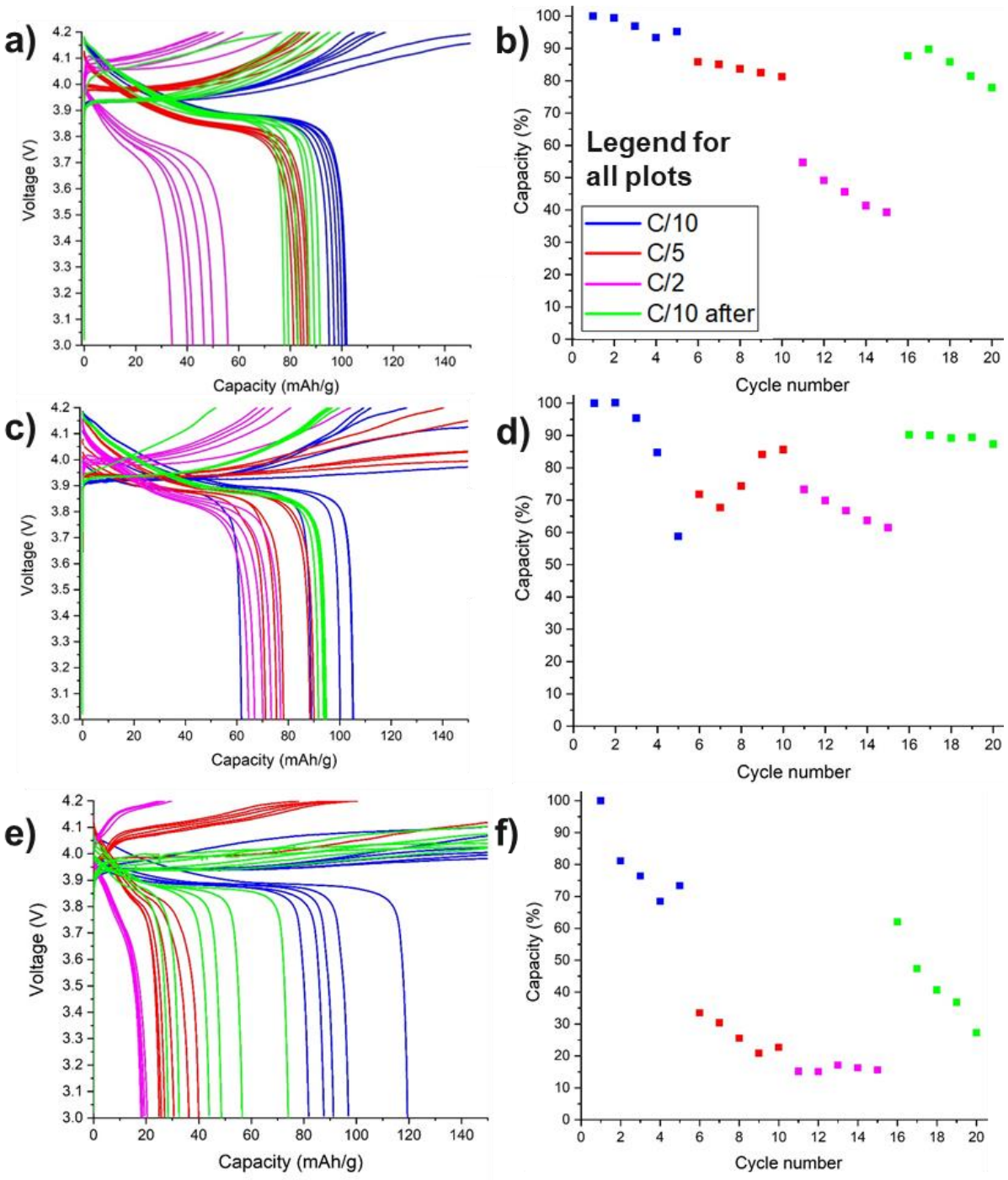

Figure 4. Charge-discharge curves and rate capability of cells containing meltblown PVDF samples M1 (a, b), M2 (c, d), and M3 (e, f).

Cells containing electrospun PVDF separators show better cycling performance than cells with meltblown samples (Fig. 5). This can be explained by the smaller average fiber diameter for

electrospun samples (0.25-0.50 μm) than the one for meltblown samples (1.4-1.7 μm), as shown in Fig. 1 and 2. Sample E3 was fabricated at higher voltage (20 kV) than samples E1 and E2 (15 kV), which led to a narrower fiber diameter distribution. As seen with meltblown samples, cells containing electrospun PVDF separators with narrow fiber size distributions show significant capacity variation with cycle number and capacity loss at rates higher than C/5 (Fig. 5f). Sample E2 shows a wide diameter distribution and stable cycling at all C-rates, including 1C (not possible with sample E3). The capacity loss and the coulombic efficiency at low C-rates are both improved compared to sample E3. However, sample E2 not only shows a wide diameter distribution, but also a large fiber diameter (0.51 μm), double that of sample E1. Cells with sample E1 separator shows the best performance during cycling compared to cells employing samples E2 and E3. Indeed, cells containing sample E1 showed little or no capacity loss at C/10 and C/5, high and stable discharge capacity at all rates, and improved coulombic efficiency.

Table 1 shows that samples E1 and E3 have lower ionic conductivities than sample E2, which has the highest electrolyte uptake. Nonetheless, cells employing sample E1, which has the widest diameter distribution, show the highest capacity retention. On the other hand, solid volume percent, mat thickness, and average fiber diameter affect electrolyte uptake and ionic conductivity, whose values are not necessarily reflected in cycling performance; for example, samples E1 and E3 have comparable uptake and conductivity but significantly different cycling performance. We conclude that the main factors influencing cycling performance for electrospun separators are the fiber diameter and its distribution. Low-capacity variation with cycling and low-capacity loss are achieved when the separator is fabricated with a low average fiber diameter (0.2-0.3μm) and a wide diameter distribution.

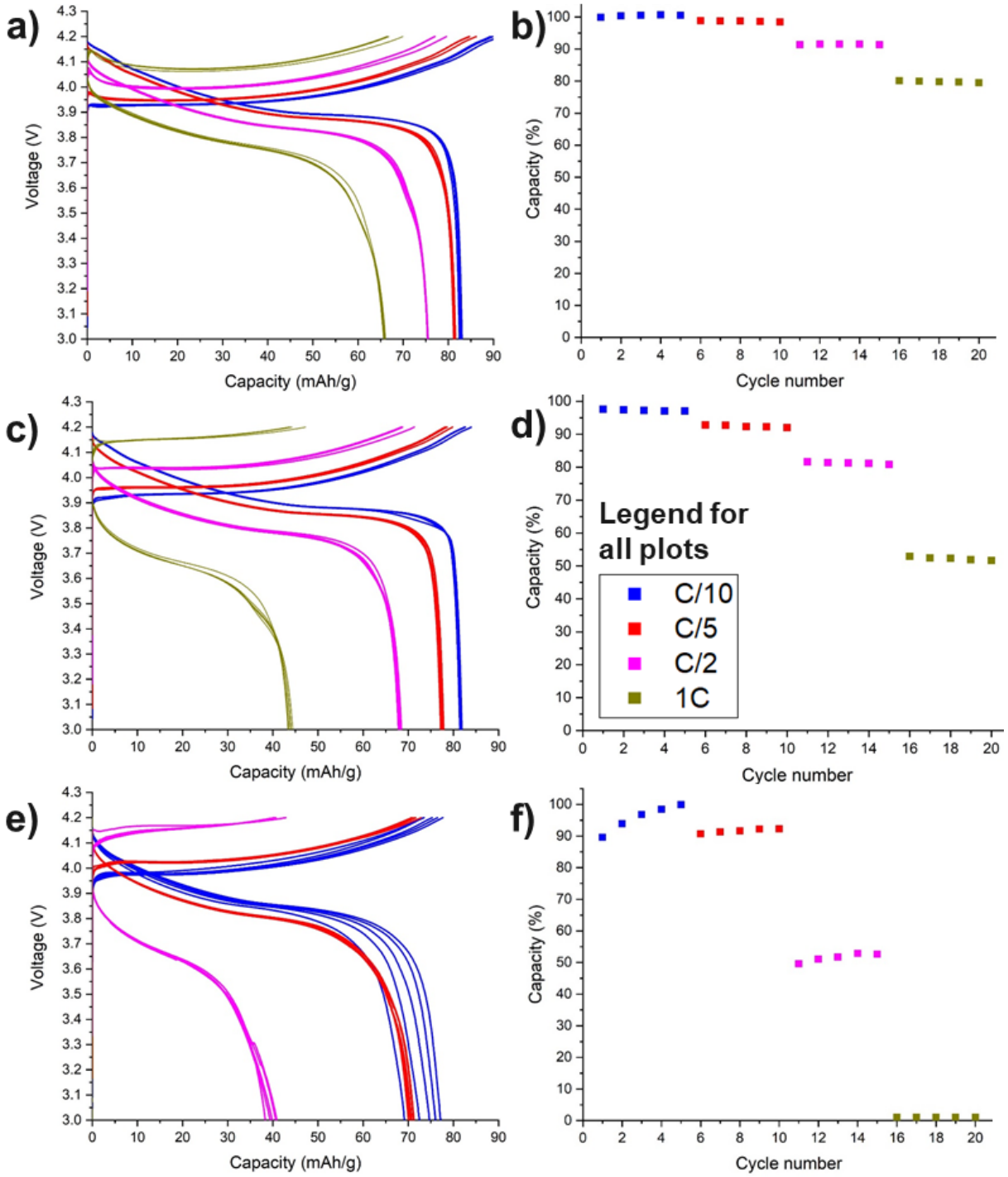

Figure 5. Charge-discharge curves and rate capability of cells containing electrospun PVDF samples E1 (a, b), E2 (c, d), and E3 (e, f).

SDC-based membranes are relatively new and their emerging applications in electrochemical devices are just beginning to be explored; to our knowledge, the present work is

the first to evaluate their comparative performance. Cycling performance of SDC separators seem comparable or better than electrospun separators, and cells containing SDC samples show high coulombic efficiency and high cycling stability relative to electrospun samples (Figs. 5 and 6). Also, cells containing SDC separators showed discharge capacity as high as meltblown samples, but with higher stability compared to electrospun samples, which means that high-shear precipitation is able to create separators that are better performing than meltblown and electrospun separators.

We fabricated the sample S3 with 10% PVDF injection solution, which created a fibrous/nano-sheet mixed web. This morphology formed a homogeneous pore network with large pore size (0.52 μm) and narrow distribution (FWHM=22 nm), as plotted in Fig. 3d. As shown for electrospun samples, cells containing separators with a narrow pore size distribution show higher capacity loss (in this case only at 1C rate) than cells with separators with wide pore size distribution. Cells employing sample S2 with a NS morphology show improved stability compared to cells with sample S3 (mixed morphology), with little or no capacity loss at C/10 and at C/5, and stable 1C cycling. Sample S1 with fibrous morphology shows the highest stability and best performance, with a discharge capacity at C/10 of 106 mAh/g (vs. M1=102 mAh/g and E1=86 mAh/g) and capacity loss at 1C equal to 18% (vs. S2=23% and S3=35%).

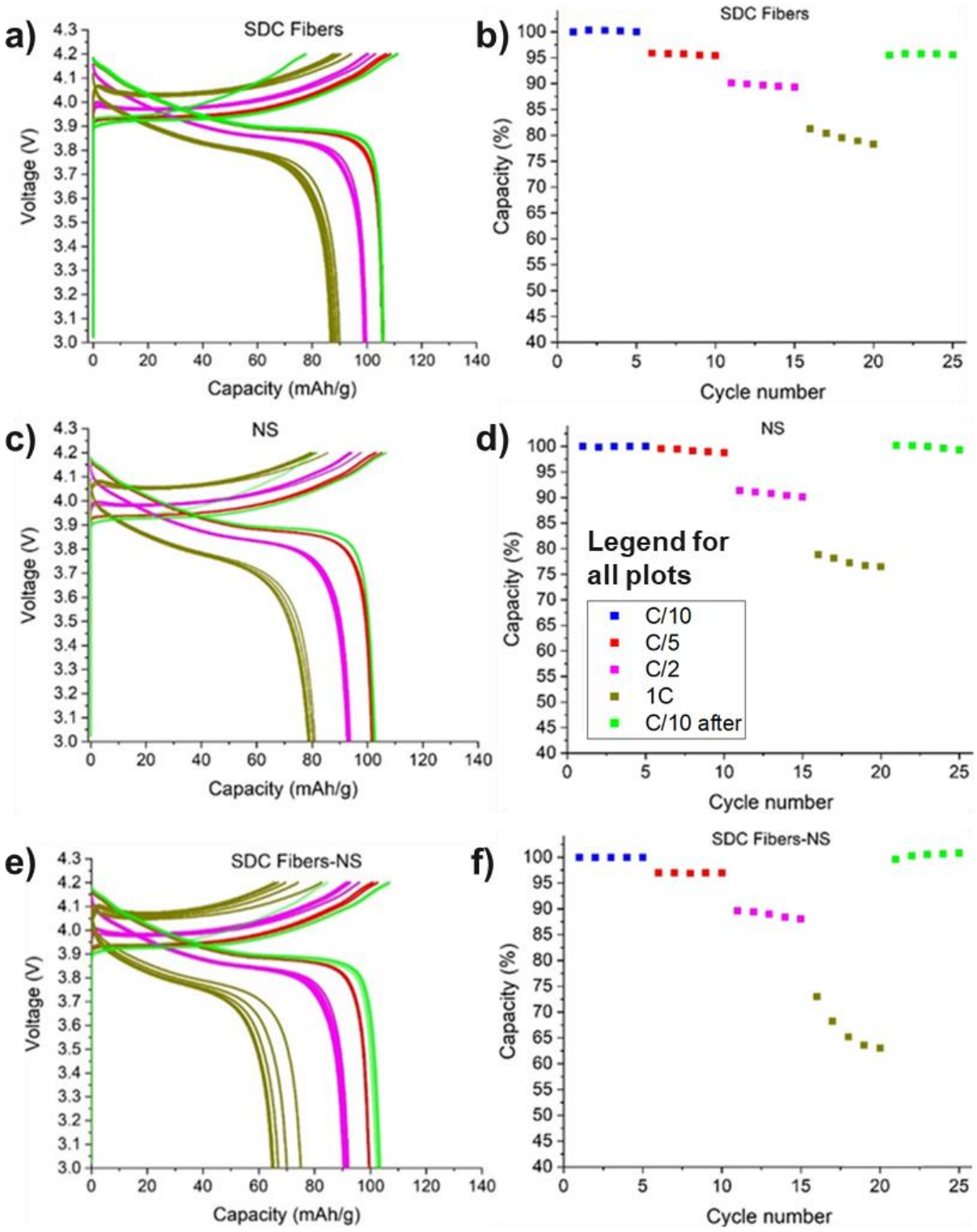

Figure 6. Charge-discharge curves and rate capability of cells containing SDC PVDF samples S1 (a, b), S2 (c, d), and S3 (e, f). Re-printed with permission from (5), Copyright IoP Science.

By using one component (PVDF) and three different techniques to fabricate membranes used in this study, we were able to correlate the structural parameters of the separator mats to their electrochemical properties. Similar conclusions may be drawn for each of the three different techniques used to fabricate separators. The fiber diameter or pore distribution has a major influence not only on the mat's physical and electrochemical properties, such as solid volume percent, ionic conductivity, and electrolyte uptake, but also and more importantly on in-use cell-cycling stability and performance in a Li-ion cell. Meltblown samples had similar average fiber diameter but the wider fiber distribution of sample M1 compared to samples M2 and M3 decreased capacity loss and improved cycling stability. By comparing electrospun sample E1 with samples E2 and E3, we see that the combination of a wide-diameter distribution and a small pore size (<200 nm) lead to the best cell-cycling performance; an improvement in discharge capacity values at all C-rates was observed. Finally, cells using the SDC mats, fibrous and nano-sheet morphologies, showed a similar cycling behavior as electrospun samples, suggesting that a key factor in designing an optimal structure for a Li-ion battery separator is the combination of a small pore size and a wide pore distribution, regardless of how the pore network is formed.

Conclusions

By using three different techniques, meltblowing, electrospinning, and shear-spinning, we fabricated PVDF Li-ion battery separators with varying fiber/pore diameters and distributions. We adjusted the processing conditions to ensure that the main difference between separators produced using the same technique was the average fiber/pore diameter and size distribution. All samples showed the same trend when in-use cycled in a Li-ion battery, *i.e.*, when the fiber/pore distribution was widened and/or pore size was decreased, the capacity loss decreased and cycling stability increased. This effect was accentuated at C-rates higher than C/5, suggesting that this specific

separator structure is essential to enable high-rate cycling of Li-ion batteries. We also showed that shear-spinning produces separators with homogeneous and controlled structure, which combine the low-solid volume percent and low-capacity losses of meltblown mats with the cycling stability of electrospun samples.

This work shows that by using a technique that fabricates homogeneous mats, separators may be produced with an optimal structure to improve the cycling performance of Li-ion batteries by designing the network with a small average pore size and a wide pore size distribution.

References

[1] Fu Q., Lin G., Chen X., Yu Z., Yang R., Li M., Zeng X., Chen J., "Mechanically Reinforced PVdF/PMMA/SiO_2 Composite Membrane and Its Electrochemical Properties as a Separator in Lithium-Ion Batteries", *Energy Technol*, 6(1):144–52, 2018.

[2] Pan J.L., Zhang Z., Zhang H., Zhu P.P., Wei J.C., Cai J.X., Yu J., Koratkar N., Yang Z.Y., "Ultrathin and Strong Electrospun Porous Fiber Separator", *ACS Appl Energy Mater*, 1(9):4794–803, 2018.

[3] Li M., Liao Y., Liu Q., Xu J., Sun P., Shi H., Li W.. "Application of the imidazolium ionic liquid based nano-particle decorated gel polymer electrolyte for high safety lithium ion battery", *Electrochim Acta*, 284:188–201, 2018.

[4] Banerjee A., Ziv B., Shilina Y., Luski S., Halalay I.C., Aurbach D., "Multifunctional Manganese Ions Trapping and Hydrofluoric Acid Scavenging Separator for Lithium Ion Batteries Based on Poly(ethylene- alternate -maleic acid) Dilithium Salt", *Adv Energy Mater*, 7(3):1601556, 2017.

[5] Luiso S., Williams A.H., Petrecca M.J., Roh S., Velev O.D., Fedkiw P.S., "Poly(Vinylydene difluoride) Soft Dendritic Colloids as Li-Ion Battery Separators". *J Electrochem Soc*., 168 020517, 2021.

[6] Luiso S., Fedkiw P.S., "Lithium-ion battery separators: Recent developments and state of art", *Curr Opin Electrochem*, 20:99–107, 2020.

[7] Luiso S., Henry J.J., Pourdeyhimi B., Fedkiw P.S., "Meltblown PVDF as A Li-Ion Battery Separator", *ACS Appl Polym Mater*, 2021, submitted.

[8] Huang X., "Separator technologies for lithium-ion batteries", *J Solid State Electrochem*, 15(4):649–62., 2011.

[9] Venugopal G., Moore J., Howard J., Pendalwar S., “Characterization of microporous separators for lithium-ion batteries”, *J Power Sources,* 77(1):34–41, 1999.

[10] Djian D., Alloin F., Martinet S., Lignier H., Sanchez J.Y., “Lithium-ion batteries with high charge rate capacity: Influence of the porous separator”, *J Power Sources,* 172(1):416–21, 2007.

[11] Kim J.Y., Lim D.Y., “Surface-modified membrane as a separator for lithium-ion polymer battery”, *Energies. Molecular Diversity Preservation International,* 3, 866–85, 2010.

[12] Luiso S., Henry J.J., Pourdeyhimi B., Fedkiw P.S., “Fabrication and Characterization of Meltblown Poly(vinylidene difluoride) Membranes”, *ACS Appl Polym Mater*, 10;2(7):2849–57, 2020.

[13] Luo R., Wang C., Zhang Z., Lv W., Wei Z., Zhang Y., Luo X., He W., “Three-Dimensional Nanoporous Polyethylene-Reinforced PVDF-HFP Separator Enabled by Dual-Solvent Hierarchical Gas Liberation for Ultrahigh-Rate Lithium Ion Batteries”, *ACS Appl Energy Mater,* 1(3):921–7, 2018.

[14] Liu J., Shi X., Boateng B., Han Y., Chen D., He W., “A Highly Stable Separator from an Instantly Reformed Gel with Direct Post-Solidation for Long-Cycle High-Rate Lithium-Ion Batteries”, *ChemSusChem,* 12(4):908–14, 2019.

[15] Ye L., Shi X., Zhang Z., Liu J., Jian X., Waqas M., He W., “An Efficient Route to Polymeric Electrolyte Membranes with Interparticle Chain Microstructure Toward High-Temperature Lithium-Ion Batteries”, *Adv Mater Interfaces,* 4(11):1–6, 2017.

[16] Liu B., Huang Y., Zhao L., Huang Y., Song A., Lin Y., Wang M., Li X., Cao H., “A novel non-woven fabric supported gel polymer electrolyte based on poly(methylmethacrylate-

polyhedral oligomeric silsesquioxane) by phase inversion method for lithium ion batteries", *J Memb Sci*., 564:62–72, 2018.

[17] Wang X., Xu G., Wang Q., Lu C., Zong C., Zhang J., Yue L., Cui G., "A phase inversion based sponge-like polysulfonamide/SiO_2 composite separator for high performance lithium-ion batteries", *Chinese J Chem Eng*, 26(6):1292–9, 2018.

[18] Li Y., Li Q., Tan Z., "A review of electrospun nanofiber-based separators for rechargeable lithium-ion batteries", *J Power Sources*, 443, 227262, 2019.

[19] Waqas M., Ali S., Feng C., Chen D., Han J., He W., "Recent Development in Separators for High-Temperature Lithium-Ion Batteries", *Small*, 15(33), 2019.

[20] Lee Y., Park J., Jeon H., Yeon D., Kim B.H., Cho K.Y., Ryou M.H., Lee Y.M., "In-depth correlation of separator pore structure and electrochemical performance in lithium-ion batteries", *J Power Sources*, 325:732–8, 2016.

[21] Ye W., Zhu J., Liao X., Jiang S., Li Y., Fang H., Hou H., "Hierarchical three-dimensional micro/nano-architecture of polyaniline nanowires wrapped-on polyimide nanofibers for high performance lithium-ion battery separators", *J Power Sources*, 299:417–24, 2015.

[22] Sabetzadeh N., Gharehaghaji A.A., Javanbakht M., "Porous PAN micro/nanofiber separators for enhanced lithium-ion battery performance", *Solid State Ionics*, 325, 251-257, 2018.

[23] Jiang Y., Ding Y., Zhang P., Li F., Yang Z., "Temperature-dependent on/off PVP@TiO_2 separator for safe Li-storage", *J Memb Sci*, 565:33–41, 2018.

[24] Zhai Y., Wang N., Mao X., Si Y., Yu J., Al-Deyab S.S., El-Newehy M., Ding B., "Sandwich-structured PVdF/PMIA/PVdF nanofibrous separators with robust mechanical strength and thermal stability for lithium ion batteries", *J Mater Chem A*, 2(35):14511–8, 2014.

[25] International Organization for Standardization. (2003). Paper and board — Determination of air permeance and air resistance (medium range) — Part 5: Gurley method (ISO Standard No. 5636-5). Retrieved from https://www.iso.org/standard/37376.html.

[26] Velev OD, Smoukov S, Geisen P, Wright MC, Gangwal S., "Method for Fabricating Nanofibers", *US Patent No. 9,217,211(B2)*, Washington, DC: U.S. Patent and Trademark Office, 2015.

[27] Velev O, Smoukov S, Marquez M., "Nanospinning of polymer fibers from sheared solutions", US Patent No. 8,551,378. Washington, DC: U.S. Patent and Trademark Office, 2015.

[28] Roh S., Williams A.H., Bang R.S., Stoyanov S.D., Velev O.D., "Soft dendritic microparticles with unusual adhesion and structuring properties", *Nature Materials*, 18, p. 1315–20, 2019.

[29] Henry J.J., Goldbach J., Stabler S., Devisme S., Chauveau J., "Advancements in the production of meltblown fibres", *Filtr Sep*, 53(3):36–40, 2016.

[30] Henry J.J., Goldbach J., Stabler S., Chauveau J., "High melt flow fluoropolymer composition", *US Patent Application No. 20170088989(A1)*. Washington, DC: U.S. Patent and Trademark Office, 2017.

[31] Reifenhauser REICOFIL Meltblown Pilot Line, Available from: https://thenonwovensinstitute.com/wp-content/uploads/2015/04/Reifenhauser-Reicofil-Meltblown-Pilot-Brochure.pdf

[32] Jena A., Gupata K., "Liquid extrusion techniques for pore structure evaluation of nonwovens" *Int Nonwoven J*, 2003, 45–53, 2003.

[33] Yarin A.L., Sinharay S., Pourdeyhimi B., "Meltblowing : Multiple polymer jets and fiber-size distribution and lay-down patterns," *Polymer*, 52,13, 2929–2938, 2011.

[34] Wang X., Ke Q., “Experimental Investigation of Adhesive Meltblown Web Production Using Accessory Air,” *Polym. Eng. Sci.*, 46, 1, 1–7, 2006.

[35] Tan D.H., Zhou C., Ellison C.J., Kumar S., Macosko C.W., Bates F.S., “Meltblown fibers: Influence of viscosity and elasticity on diameter distribution,” *J. Nonnewton. Fluid Mech*., 165, 15–16, 892–900, 2010.

[36] Ellison C.J., Phatak A., Giles D.W., Macosko C.W., Bates F.S., “Melt blown nanofibers : Fiber diameter distributions and onset of fiber breakup,” *Polymer*, 48, 3306–3316, 2007.

[37] Barilovits, S., “Experimental Study of a Unique Multi-Row Meltblowing Fiber Formation Process and the Web Structures Produced Thereby” (Doctoral dissertation), 2018. Retrieved from NC State Repository.

[38] Tan A.R., Ifkovits J.L., Baker B.M., Brey D.M., Mauck R.L., Burdick J.A., “Electrospinning of photocrosslinked and degradablefibrous scaffolds”, *Journal of Biomedical Materials Research Part A*; 87(4):1034-1043, 2008.

[39] Malašauskienė J., Milašius R., “Mathematical Analysis of the Diameter Distribution of Electrospun Nanofibres”, *FIBRES & TEXTILES in Eastern Europe*, Vol. 18, No. 6 (83) pp. 45-48, 2010.

[40] Petrakis D.E., Hudson M.J., Sdoukos A.T., Pomonis P.J., Bakas T.B., “Controlled modulation of mesoporosities in metal (M = Al, Fe) phosphate solids”, *Colloids and Surfaces*, A: Physicochemical and Engineering Aspects, 90 191-202, 1994.

CHAPTER 7: Recommendations

Die density and capillary size in meltblowing

In this work, we investigated the use of nonwoven or nonwoven-like separators for Li-ion batteries and examined structure-property-process relationships using three processing techniques. We demonstrated the possibility to melt-blow PVDF Kynar® resin RC 10,287 to produce a high quality mat. Fiber mats showed 30-40% sub-micron fibers with diameters as small as <400 nm, but an investigation on the effect that different dies and capillary size have on the mat structure would bring more insights on structure-property-process relationships and could possibly enable mats with smaller-diameter fibers. In fact, changing the die density from 45 to 60 holes-per-inch not only will decrease the amount of roping, but will also change the membrane structure [1]. Roping is considered a defect in nonwovens and may influence the mat's electrolyte uptake and lithium ion transport due to decrease of surface area. Cycle-life experiments of cells containing meltblown PVDF separators showed long-term stability issues possibly due in part to large pore size that caused micro-shorts. Capillary size has a strong influence on fiber diameter, especially at high throughputs. Using a die with capillary diameter lower than 0.3 mm (used in the Reicofil experiments), will enable throughputs lower than 11 kg h^{-1} (the lowest used in this work). As demonstrated in Chapter 3, the lower is the throughput, the lower are the fiber diameter and the pore size.

Purity of PVDF Resin

As explained in Chapter 4, chain-transfer agents in high level are added during Kynar® RC 10,287 resin polymerization, and additives, such as low-molecular weight glycols and other surfactants, are reported to be added afterwards to improve melt-processability [2]. Chain-transfer agents, additives, and surfactants are susceptible to electrochemical reaction and we presume that

they are still residual in the resin we used. These components will leach out of the fiber mat and will electrochemically react, causing fiber morphological changes, separator activation step, and unstable capacity. Fabricating this PVDF resin with a higher purity without sacrificing melt-processability properties would be not only be beneficial for battery operations in terms of coulombic efficiency and long-term cycling when using these nonwoven mats as separators, but would likely reduce capacity loss too.

New morphologies and composites of SDC membranes

In Chapter 5, we showed that a shear-spinning process may be used to control the morphology of the web-forming PVDF particles and, therefore, the cell-cycling performance using separators formed from them. The morphology of the membranes may be adjusted in other ways, such as layering or mixing together SDC particles with two or more morphologies, which would tailor these membranes to specific applications. The versatility of the process allows for multiple polymer precipitation, which include the investigation of new solvent/non-solvent combinations, and for incorporation of additives such as ceramic particles, for composite separators. The addition of ceramic additives increases thermal and mechanical properties of the mat, but the traditional incorporation techniques (Chapter 2) do not provide additional functionality. The SDC process could be used to fabricate multifunctional separators by adding to the injection solution reactive precursors (such as poly(ethylene-*alternate*-maleic acid or examethyldisiloxane) to form functional groups in the separator, which becomes chemically active and provides additional features in terms of safety and performance. Research on these membranes needs to take into consideration both the market and safety needs. By nano-engineering the material network in a battery separator, we could be able to create preferred pathways for ion transport in 3D structures that maximize the Li ions motion and reduce the chances of dendrite formation. To investigate the

3D structure of separators, nano-computed tomography or synchroton imaging of the separator alone or inside the battery could give insights not only on the 3D distribution of pores, but also on morphological changes and dendrites pathways after battery use.

β-phase PVDF

The crystalline phase with the largest polarization in PVDF is the β-phase [3], which is useful for pyro- and piezoelectricity. Obtaining β-phase PVDF requires solvent-casting, mechanical stretching of the α-phase PVDF, or polarization under high electric fields [4], but all of these methods usually are complicated to implement for large scale industrial processing [3]. Meltblown PVDF mats are produced from the melt, and the crystalline regions of the fibers are expected to be all α-phase PVDF [3]. However, as discussed in the Appendix C, meltblown mats surprisingly showed 55% β-phase content (through FT-IR), which decreases to 50% after melt-pressing the mats. When the polymer filaments exit the die during meltblowing, they are quickly drawn by hot air jets. We believe that there is a specific moment when the outer surface of the fibers has solidified but the fibers are still being stretched. The fast re-crystallization of PVDF from the melt, together with the increase in polymer chain orientation due to filament stretching, produce a high content of β-phase [5,6]. Kundu *et al.* [7] showed that the higher is the content of β-phase in PVDF-based Li-ion battery separators, the higher is the polarity with subsequent fast lithium ion migration, and improved electrochemical performance, such as discharge capacity and capacity retention. An investigation of the effect that the β-phase content has on separator performance would lead to an improved design of experiments for additional meltblowing experiments. For example, the die-to collector distance could be increased during meltblowing to allow a higher fiber stretching, leading to a higher β-phase content. FT-IR, DSC, and X-ray diffraction characterizations on meltblown, electrospun, and shear-spun separators before and after

use in a Li-ion cell would elucidate whether the different β-phase content of the mats is responsible for different cycling behaviors of separators made with different processes and whether cycling the separators has an effect on the β-phase content.

References

[1] Roberts, E. M., "Advanced Meltblown Structures" (Doctoral dissertation), 2020. Retrieved from NC State Repository.

[2] Henry J.J., Goldbach J., Stabler S., Chauveau J., "High melt flow fluoropolymer composition", *US Patent Application No. 20170088989(A1).* Washington, DC: U.S. Patent and Trademark Office, 2017.

[3] Martins P., Lopes A.C.C., Lanceros-Mendez S., "Electroactive phases of poly(vinylidene fluoride): Determination, processing and applications", *Prog. Polym. Sci.*, 39, 683–706, 2014.

[4] Liang C.L., Mai Z.H., Xie Q., Bao R.Y., Yang W., Xie B.H., Yang M.B., "Induced Formation of Dominating Polar Phases of Poly(vinylidene fluoride): Positive Ion–CF_2 Dipole or Negative Ion–CH_2 Dipole Interaction", *J. Phys. Chem. B*, 118, 9104–9111, 2014.

[5] Cai X., Lei T., Sun D., Lin, L., "A critical analysis of the α, β and γ phases in poly(vinylidene fluoride) using FTIR", *RSC Adv.*, 7, 15382–15389, 2017.

[6] Yang D., Chen, Y., "β-phase formation of poly(vinylidene fluoride) from the melt induced by quenching", *J. Mater. Sci. Lett.*, 6, 599–603, 1987.

[7] Kundu M., Costa C.M., Dias J., Maceiras A., Vilas J.L., Lanceros-Mendez S., "On the Relevance of the Polar β-Phase of Poly(vinylidene fluoride) for High Performance Lithium-Ion Battery Separators", *J. Phys. Chem. C*, 121, 26216−26225, 2017.

APPENDICES

Appendix A: Lithium-ion conducting water-in-salt sulfonated pentablock polymer as a quasi-solid-state electrolyte

Introduction

Lithium-ion batteries exemplify advancements in battery storage technology due to their impressive energy storage capacity and ongoing improvements in production costs. However, while most of the discussion related to lithium-ion batteries has focused on the anode and cathode materials, our focus here is on the separator. While the separator located between the anode and the cathode of the battery is independent of the electrochemical reactions that occur, its structure and properties play a critical role in the performance of the cells. While the cell is in use, the primary role of the separator is to allow lithium ions to pass through the electrolyte from anode to cathode. When the cell is not in use, the separator limits ion diffusion. Unfortunately, the liquid electrolytes often employed in conventional lithium-ion batteries are highly flammable at elevated temperatures and can undergo combustion within the cell. One promising route to address these concerns is the use of gel polymer electrolytes (GPEs). The field of GPEs is a rapidly growing area of materials research because of the negligible volatility and decreased hazard risk of GPEs compared to traditional liquid electrolytes, which contain toxic compounds and can combust. In the GPE design, liquid electrolytes are imbibed into a polymer matrix, which effectively entrains a liquid component while allowing it to remain functionally active, thereby presenting a methodology by which to design safe and efficient next-generation battery components.

Their soft, elastomeric characteristics make thermoplastic elastomers (TPEs) possessing ionic (charged) blocks good potential candidates for a variety of electrochemical applications. In fact, TPEs have been tailored for ionic conductivity on the molecular scale. For instance, the sulfonation of the styrenic endblocks of conventional TPEs derived from poly[styrene-*b*-(ethylene-

co-butylene)-*b*-styrene] (SEBS) copolymers has been accomplished on multiple occasions[1]. Elabd *et al.* [2,3] have reported promising results for these materials in both proton and lithium exchange membranes, due to the presence of bound $–SO_3$ groups. Highly endblock-sulfonated poly[styrene-*b*-isobutylene-*b*-styrene] (SIBS) polymers, for example, achieve proton conductivity levels of ~0.1 S/cm [4]. However, polar organic electrolytes, as those used in batteries and fuel cells, compromise the physical cross-links of TPE membranes. These physical cross-links are the result of microphase separation of the thermodynamically-incompatible chemical sequences and are primarily responsible for endowing TPEs with their elastomeric characteristics. Realizing the shortcoming associated with endblock sulfonation, recent studies have examined similar functional groups attached to the midblock of TPEs. An approach that is now commercially available relies on sulfonating a styrenic midblock and replacing the endblocks with one or more ionophobic blocks such as certain acrylics [5,6] or further substituted styrene [7]. An alternative approach to ionically functionalize the midblocks of TPEs is to retain styrenic endblocks and sulfonate the softer midblock. Vargantwar *et al.* [8] sulfonated butadiene units in a poly(styrene-*b*-butadiene-*b*-styrene) (SBS) copolymer, whereas Xie *et al.* [9]quaternized the midblock of a chemically similar SBS copolymer. The sulfonated midblock approach has been repeatedly demonstrated to enhance the mechanical shortcoming of endblock-sulfonated TPEs and maintain comparable conductivity at similar sulfonation levels [10].

Addition of a midblock-selective liquid to a TPE yields a TPE gel (TPEG), and amphiphilic TPEGs containing a hydrophilic midblock have been successfully used as solar cell electrolytes after incorporation of photosensitive dye molecules. For example, TPEGs composed of poly[styrene-*b*-(ethylene oxide)-*b*-styrene] (SEOS)/ionic liquid [11] and Nexar^{TM}/H_2O [12], each containing one of several Ru^{2+}-based dyes, have achieved solar efficiencies of ~2.5% and ~7.0%,

respectively (Fig. 1a). The thermodynamic stability of these TPEGs also greatly enhances their operational lifetime (Fig. 1b) as compared to liquid-based electrolytes, which have a tendency to dissolve or degrade the cell sealant and leach into the environment over time. The production of polar and ionic TPEs and TPEGs also translates to intriguing material transport properties due to their favorable interactions with polar molecules and salts.

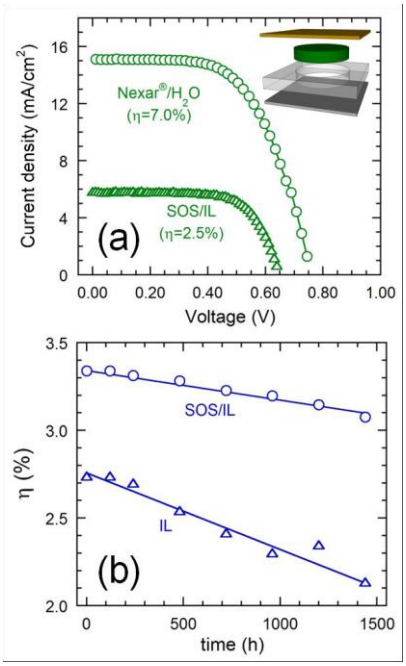

Figure 1. Photocurrent-density as a function of voltage for Ru^{2+}-dyed TPEGs: poly[styrene-b-(ethylene oxide)-b-styrene]/ionic liquid (SOS/IL) and Nexar®/H2O (a), and a comparison of the stability in solar cell efficiency (η) between SOS/IL and its pure-IL analog (b) [11.12].

A midblock-sulfonated pentablock TPE commercially designated as Nexar™ has proven particularly promising in this regard [13,14]. The chemical structure of Nexar™, a poly[*tert*-butyl styrene-*b*-(ethylene-*alt*-propylene)-*b*-(styrene-*co*-styrenesulfonate)-*b*-(ethylene-*alt*-propylene)-*b*-*tert*-butyl styrene] pentablock polymer, is displayed in Fig. 2. In recent studies, Nexar™, in combination with a number of solvents and fillers, has been used as an electrically-induced actuator. Lee *et al.* have successfully incorporated a midblock-compatible sulfonated

montmorillonite [15] and ionic liquid [16,17] into Nexar™. Other efforts have incorporated ethylene glycol and glycerol into Li^+-exchanged Nexar™ resulting in a lower ionic concentration and consequently a slower mechanical response of the actuator, but with one of the highest overall actuations ever captured for an ionic polymer-metal composite [18,19]. The microphase-separated nanostructure of Nexar™ allows for selective incorporation of polar electrolytes [12,18] and ionic liquids [19] within the hydrophilic sulfonated microdomains of the polymer. Selective swelling of the sulfonated midblock provides nanoscale channels by which ions can transport, while maintaining structural integrity due to the thermoplastic elastomeric network, which is not possible with traditional polymer electrolytes.

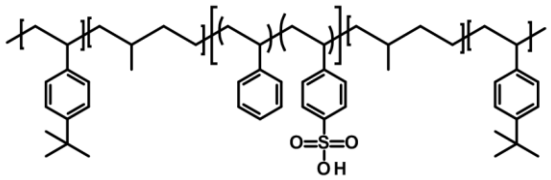

Figure 2. Chemical structure of Nexar™.

However, one drawback of using GPEs, specifically Nexar™, is that they are not as conductive as their liquid electrolyte counterparts. Aqueous electrolytes constitute a highly attractive alternative to common organic electrolytes. Mineart *et al.* [20] have demonstrated that Nexar™ membranes with dispersed ion-rich micelles swell in water beyond 100% as the morphology converts to a highly disordered, but irreversibly connected, ion-rich channel network. In this work, the micelles along the diffusion direction connect as water enters the membrane, eventually connecting the hydrophilic pathways in a continuous network, which is likely more effective for ion transport. Dai *et al.* [21] demonstrated that the final morphology of the membranes after immersion in water is dependent on the casting solvent. If membranes are cast from 85/15 w/w toluene/isopropyl alcohol (TIPA), the original irregular morphology cannot be well-defined

after water immersion, while for tetrahydrofuran (THF)-cast membranes, the morphology remains lamellar even after immersion in water.

The stability window of water-based electrolytes is narrow due to water electrolysis. At low potential values (<3.0 V), hydrogen evolution occurs, which severely deteriorates the electrode and presents safety concerns [22]. Suo *et al.* [23] have reported the use of water-in-salt electrolyte (WiSE) to achieve a voltage window up to ~3 V using 21 m lithium bis(trifluoromethane sulfonyl)imide ($LiTf_2N$) as the electrolyte in water. The WISE extends the operational voltage because all water molecules interact with Li^+ ions. Dubouis *et al.* [24] have established that hydroxyl groups are responsible for surface passivation by water reduction, which create a stable solid electrolyte interphase (SEI). The WiSE design enables the use of electrode materials that have been previously incompatible, such as MoS_2, which has recently attracted considerable attention by the scientific community because Li ions easily intercalate in its structure [25,26]. Quan *et al.* [27] have observed that MoS_3 electrodes can be used as anodes in WiSE Li-ion batteries and the cell is stable after 1000 cycles.

In this work, we fabricate a Li-ion conducting WiSE sulfonated pentablock polymer and report the cycling performance of a $MoS_3/LiMnO_4$ cell with this quasi-solid-state electrolyte. We also examine the morphology of the polymer after different solvent-related templating and annealing procedures, as well as exposure to electrolyte at different concentrations.

Experimental

Membrane preparation

The Nexar^{TM} was provided in film form by Kraton Polymers (Houston, TX). These ionomers were prepared by midblock-selective sulfonation of a parent pentablock copolymer (with corresponding block weights of 15–10–28–10–15 kDa). Preparation

considerations and solvent templating of Nexar™ films have been previously described in detail by Mineart *et al.* [28] and the method for fabricating these nanostructured materials will follow those guidelines. The first step of the process is dissolving Nexar™ in either pure tetrahydrofuran (THF) solvent or an 85/15 w/w toluene/isopropanol (TIPA) cosolvent. The films were cast in Teflon molds, which are covered to limit the rate of solvent evaporation and left to dry for 48 h. Some of the resultant films were solvent-vapor annealed in THF for 24 h and subsequently dried under vacuum for 2 h at ambient temperature. After drying, the membrane was immersed in LiTFSI/H_2O solutions varying in electrolyte concentration for 24 h.

MoS_3 anode preparation

After dispersing 0.2 g of ammonium tetrathiomolybdate $(NH_4)_2MoS_4$ in 200 ml of water, 1 mol/L HCl was added drop-by-drop during stirring until the pH of the solution dropped below 3. The solution was then stirred for another 2 h. The acidification of $(NH_4)_2MoS_4$ can be described according to [29]:

$$MoS_4^{2-} + 2H^+ \rightarrow MoS_3 + H_2S$$

It is important to maintain a gas phase rich in H_2S, since every uncontrolled loss of sulfur could promote an undesirable variation in the final product. The obtained product was collected by centrifugation and then washed several times with deionized water. After freeze-drying, it was annealed under argon at 200 °C for 2 h.

Electrochemical measurements

The anodes were fabricated by uniformly mixing and compressing $LiMn_2O_4$, carbon black and poly(tetrafluoroethylene) (PTFE) at a mass ratio of 8:1:1, and the cathodes combined MoS_3, carbon black and PTFE at a mass ratio of 7:2:1. Electrolyte was not added to the electrodes but rather excess electrolyte was added to the separator by soaking Nexar™ membranes in 21 m

LiTFSI/H_2O for 24 h $LiMn_2O_4/MoS_3$ coin cells were assembled and chronopotentiometry measurements were conducted with a VMP3 potentiometer. The cells were cycled between 0.7 and 2 V at a constant rate of 0.1 A/g for 10 cycles and thereafter cycled at 1 A/g for 1000 cycles to assess cycling stability. A minimum of 3 replicas per separator were assembled into coin cells and cycled to assess reproducibility.

Small-angle X-ray scattering (SAXS)

We examine SAXS profiles collected from Nexar^{TM} at the Advanced Light Source (Argonne National Laboratory) under a variety of casting/exposure conditions to determine how the morphology is affected. The positions of the scattering peaks relative to q* provides information regarding the spatial symmetry of the morphology.

Results and discussion

Cyclic voltammetry (CV) data are measured at a scan rate of 1 mV/s Figure 3b displays one broad but distinct redox peak couple of lithiation/delithiation after the initial two cycles. In the initial cycles, the cathodic scan (*i.e.*, battery charging) profile has a distinct peak at 1.8 V that disappears from the fifth cycle, implying an irreversible phase transformation of MoS_3 during its lithiation during the initial cycles. The cathodic scan profile remains stable after 5 cycles, indicating the stabilization and reversibility of electrode materials after the initial transformation. In comparison, cells with glass-fiber separators (Fig. 3a) indicate a similar irreversible peak but with a broader area inside the curve, confirming that cells constructed with Nexar^{TM} possess a more capacitive-like behavior. The galvanostatic dis-/charge curve in Figure 4b shows a sloping voltage plateau at ~1.3 V (mid-voltage) during both charge and discharge, despite its appearance to be more sloped in the initial cycle. These observations, are in good agreement with the results of CV because it is clear that MoS_3 first undergoes irreversible conversion and then remains stable.

Cells with glass-fiber separators show slightly different curves with a plateau on discharge from 1.7 to 1.5 V. This is likewise in agreement with a more capacitive behavior of cells containing Nexar^{TM}.

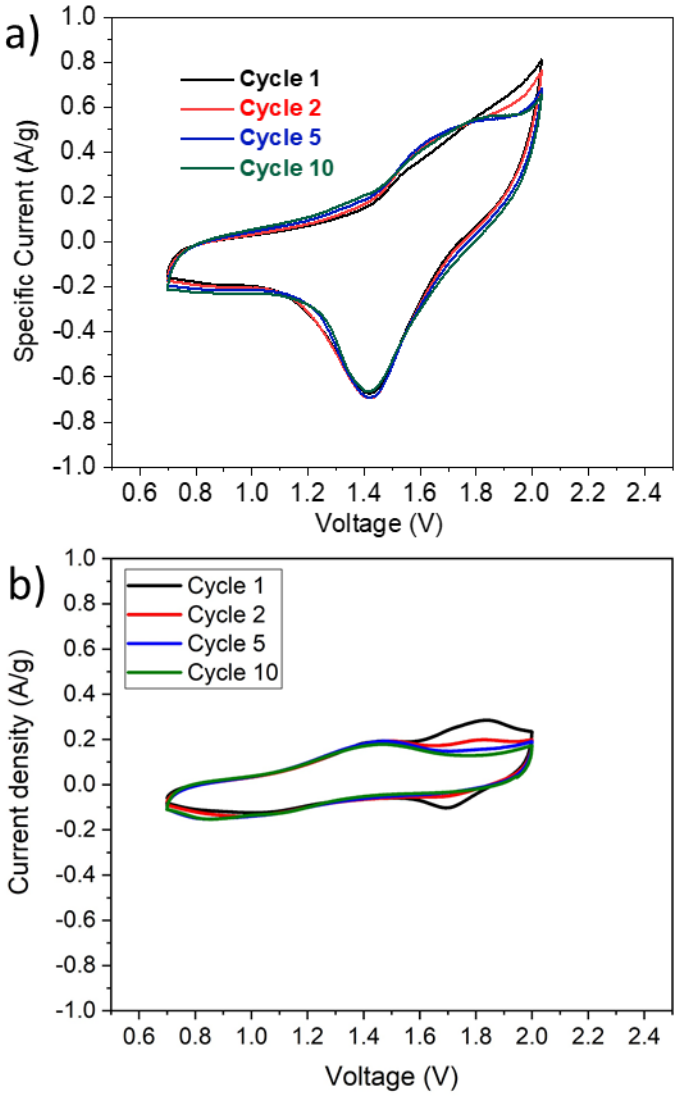

Figure 3. Cyclic voltammetry curves at initial cycles at 1 mV/s of the WISE-based $LiMn_2O_4/MoS_3$ with fiber-glass (a) and Nexar (b) separator.

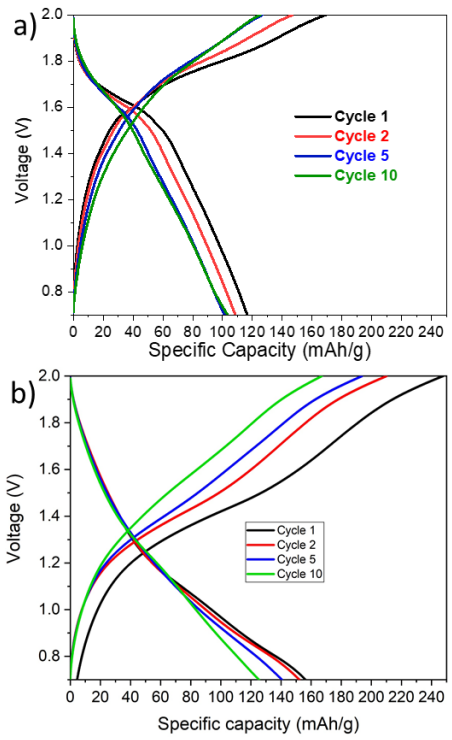

Figure 4. Galvanostatic charge/discharge profiles of the WISE-based $LiMn_2O_4/MoS_3$ with fiber-glass (a) and Nexar (b) separator,

The cycling stability of the full cell has been evaluated at high current density (1 A/g) for 1000 cycles. The specific capacities of MoS_3 are 156 mAh/g at 0.1 A/g and 82 mAh/g at 1 A/g for the first cycle. In comparison, cells constructed with glass-fiber separators reveal an initial specific capacity of 116 mAh/g at 0.1 A/g. Cells containing Nexar^{TM} achieve excellent cycling stability with a 75% capacity retention after 1000 cycles at 1 A/g, corresponding to a capacity decay rate of 0.025% per cycle. In contrast, cells containing glass-fiber separator cycled at rates 10 times lower (0.1 A/g) indicate a 59% capacity retention in 1000 cycles, corresponding to a capacity decay of 0.041% per cycle. The initial Coulombic efficiency of the cell is 90% for Nexar^{TM} and 49% for glass-fiber, due to the irreversible phase transformation of MoS_3 and the formation of SEI. After 10 cycles, the Coulombic efficiency increases to 96% and 82% for Nexar^{TM} and glass-fiber cells, respectively. It takes several cycles for the efficiency to stabilize at 99% for cells containing

either Nexar™ or glass-fiber separators, with the latter taking longer. The completion of phase transformation and the formation of a stable and protective SEI is faster when Nexar™ is used as the separator, most likely due to improved Li-ion diffusion through the quasi-solid-state-electrolyte.

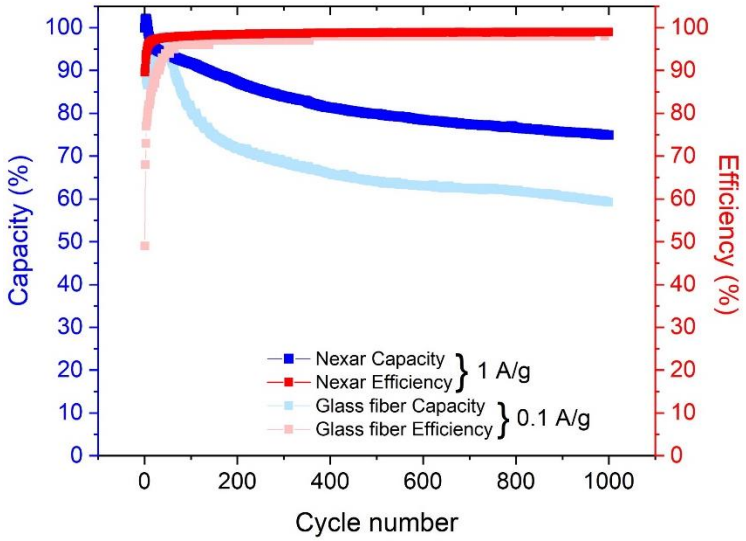

Figure 5. Cyclic voltammetry curves at initial cycles at 1 mV/s of the WISE-based $LiMn_2O_4/MoS_3$ with fiber-glass (a) and Nexar (b) separator.

The electrochemical measurements reported herein indicate very promising results for Nexar™ -based separators in aqueous Li-ion batteries. As demonstrated previously, exposure of Nexar™ to different casting solvents, solvent vapors and water can strongly impact the nanoscale morphology of Nexar™. As a preface, casting Nexar™ from THF typically results in nonequilibrium coexisting morphologies consisting of hexagonally-packed ionophobic cylinders embedded in an ionophilic matrix and co-alternating lamellae, whereas casting from TIPA generated highly nonequilibrium morphologies that can be described as micellar with ionophilic cores and ionophobic shells. After solvent-vapor annealing in THF, both morphologies evolve toward a single equilibrium lamellar morphology. To identify these conditions as well as the

electrolyte concentration, we designate the specimens prepared here as (casting solvent)(solvent-vapor annealing time, in h)/(electrolyte concentration, in m). As an example, TIPA24/21 refers to Nexar^{TM} cast from 85/15 w/w TIPA, subsequently subjected to solvent-vapor annealing in THF for 24 h and finally immersed in an aqueous 21 m LiTFSI solution for 24 h (the immersion time is held constant).

A series of SAXS intensity profiles acquired from Nexar^{TM} specimens that correspond to limiting cases is presented as a function of scattering vector (q) in Figure 6. Two important pieces of information can immediately be gleaned from these data. First, the position of the first (principal) peak (q*, filled arrowhead) is sensitive to specimen history. A shift in q* to lower q corresponds to microdomain swelling. According to Bragg's law, the microdomain period (D) is related to q* by D = 2□/q*, and values of D extracted from the profiles are included for color-coded comparison in Figure 6. The dashed vertical line in this figure corresponds to the equilibrium morphology for Nexar^{TM} that was previously reported by Mineart *et al.* [30], indicating that most of the specimens examined here are swollen. The second characteristic of these profiles is that all but one exhibits higher-order scattering peaks (open arrowheads), indicative of long-range order. The positions of these peaks relative to q* provides information regarding the spatial symmetry of the morphology. Since these peaks are located at integer values of q*, we can conclude that all these morphologies are lamellar. However, the shoulder evident on the principal peak for the specimens that were solvent-vapor annealed for 24 h, along with the unaccounted peak in the vicinity of 0.32 nm^{-1} (stick arrowheads), indicate the existence of a second characteristic size scale. While this could reflect the presence of lamellae differing in size, it more likely corresponds to periodic perforations in the lamellae. Perforated lamellae have been previously identified experimentally and computationally in a wide range of block polymers. While ideal, single-grain

lamellae can provide continuous pathways for ion diffusion, real systems consist of grain boundaries and other defects that could hinder diffusion. Existence of perforated lamellae could overcome this drawback by providing additional diffusive pathways.

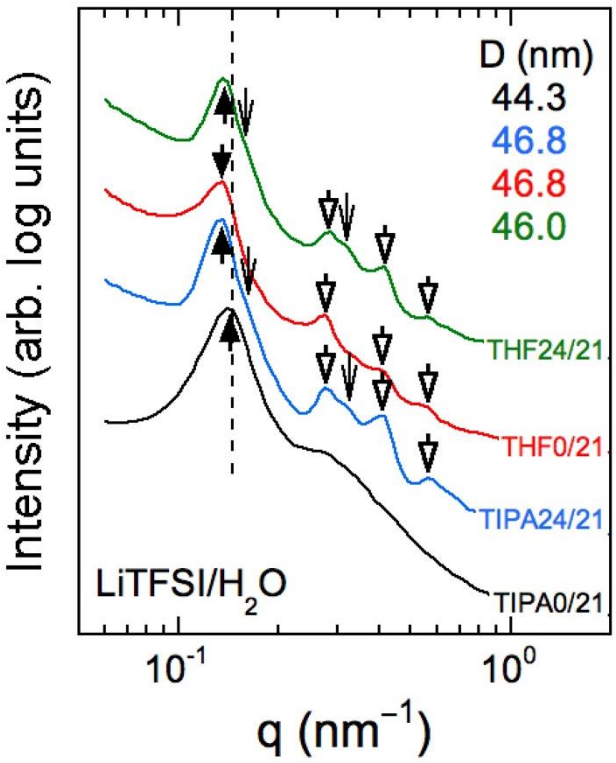

Figure 6. SAXS profiles of color-coded specimens according to designations in the text.

Additional SAXS profiles of Nexar™ specimens after immersion in different electrolyte concentrations for 24 h are displayed in Figure 7 for films cast from TIPA and Figure 8 for films. cast from THF. In all cases except the TIPA0 series, a lamellar morphology develops due to extensive solvent-vapor annealing. The coexistence of a second structural detail differing in length scale is confirmed by a shoulder on the principal peak of several profiles, as well as the convoluted principal peak in the TIPA24 series.

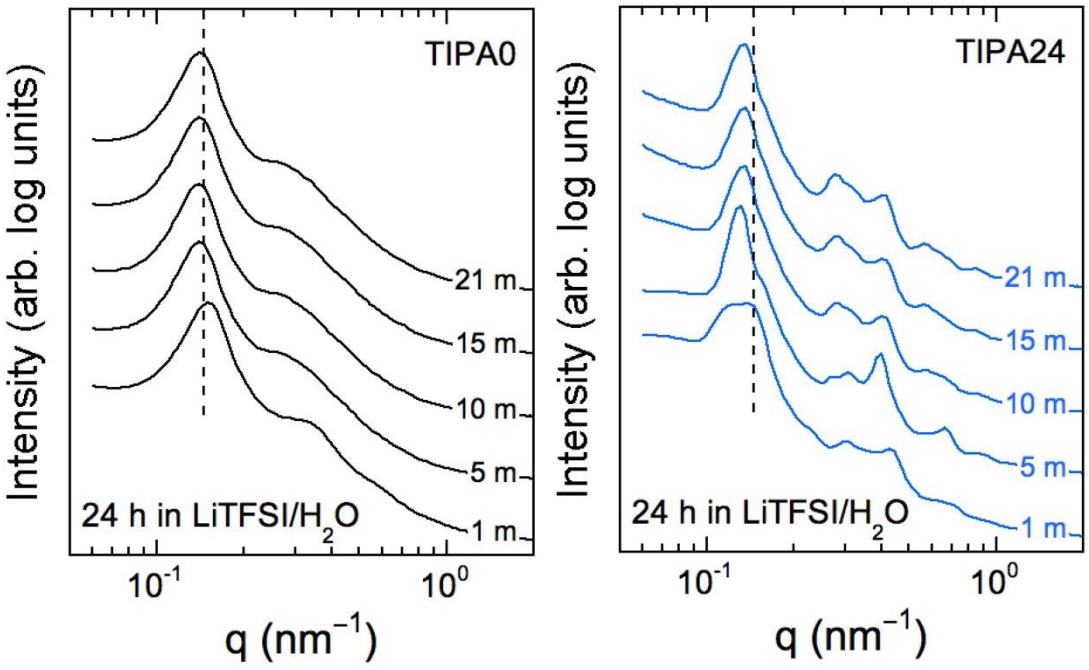

Figure 7. SAXS profiles collected from TIPA-cast Nexar™, followed by solvent-vapor annealing in THF for 0 h (*left*) and 24 h (*right*) prior to immersion in aqueous LiTFSI solutions at different concentrations.

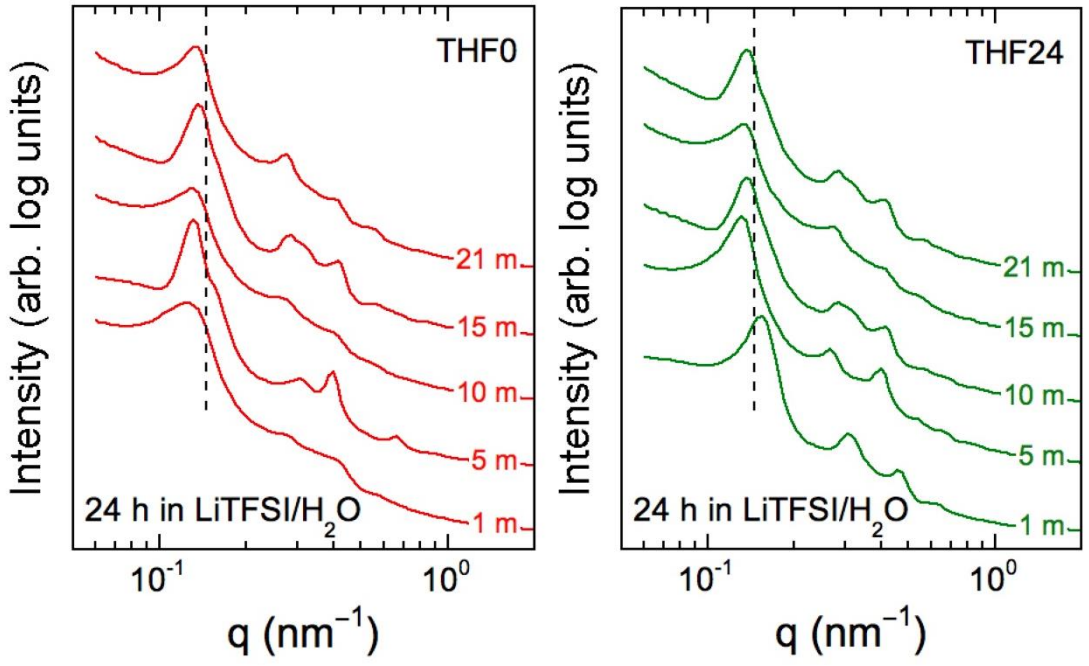

Figure 8. SAXS profiles collected from THF-cast Nexar™, followed by solvent-vapor annealing in THF for 0 h (*left*) and 24 h (*right*) prior to immersion in aqueous LiTFSI solutions at different concentrations.

Values of the microdomain period extracted from these data are compiled in Figure 9 and indicate that most of the membranes undergo progressive swelling to saturation as the electrolyte concentration is increased. Specimens cast from TIPA display equilibrium swelling with little noise in the data, whereas THF-cast films show evidence of fluctuations. This mirrors previous studies wherein solvent-vapor annealing of TIPA-cast films generate highly-ordered lamellae in ~4 min because they are so far from equilibrium, whereas the THF-cast films are much closer to equilibrium and require significantly more time to eliminate defects in their morphology.

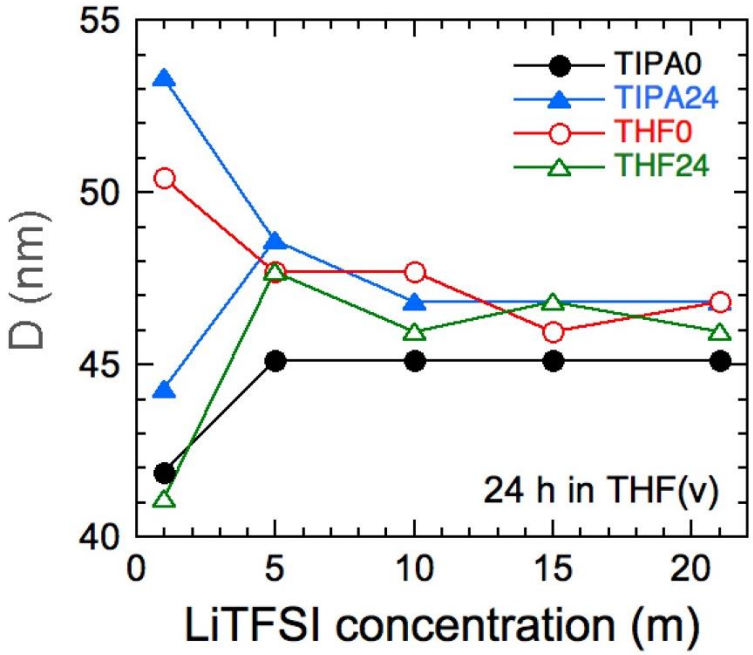

Figure 9. Values of the microdomain period extracted from the SAXS profiles in Figures 7 and 8 (labeled and color-coded) and presented here as a function of LiTFSI concentration. The solid lines serve to connect the data.

Conclusions

We report the fabrication of a quasi-solid-state electrolyte by combination of WiSE electrolyte and a sulfonated pentablock polymer. We have also investigated the cycling performance of MoS_3/$LiMnO_4$ cells containing the WiSE-polymer separator. These cells exhibit

high specific capacity (156 mAh/g) and excellent capacity retention (75%) after 1000 cycles. During battery operation, MoS_3 undergoes irreversible reaction that allows the cell to reach a 99% coulombic efficiency. Compared to glass-fiber, cells containing WiSE-Nexar™ display a more capacitive behavior. Preliminary morphological studies confirm that the structure of the Nexar™ membranes is sensitive to solvent-related processing and electrolyte immersion. This study promises the possibility to fabricate quasi-solid polymer electrolyte to enable good Li-ion diffusion for aqueous energy storage.

References

[1] Weiss R.A., Sen A., Willis C.L., Pottick L.A., "Block copolymer ionomers: 1. Synthesis and physical properties of sulphonated poly(styrene-ethylene/butylene-styrene)", *Polymer (Guildf)* , 32(10):1867–74, 1991.

[2] Elabd Y.A., Walker C.W., Beyer F.L., "Triblock copolymer ionomer membranes: Part II. Structure characterization and its effects on transport properties and direct methanol fuel cell performance", *J Memb Sci,* 1(1–2):181–8, 2004.

[3] Elabd Y.A., Napadensky E., Sloan J.M., Crawford D.M., Walker C.W., "Triblock copolymer ionomer membranes: Part I. Methanol and proton transport", *J Memb Sci* , 217(1–2):227–42, 2003.

[4] Elabd Y.A., Napadensky E., Walker C.W., Winey K.I., "Transport Properties of Sulfonated Poly(styrene-b-isobutylene-b-styrene) Triblock Copolymers at High Ion-Exchange Capacities", *Macromolecules,* 39(1):399–407, 2006.

[5] Saito T., Moore H.D., Hickner M.A., "Synthesis of Midblock-Sulfonated Triblock Copolymers", *Macromolecules,* 43(2):599–601, 2010.

[6] Moore H.D., Saito T., Hickner M.A., "Morphology and transport properties of midblock-sulfonated triblock copolymers", *J Mater Chem,* 20(30):6316–21, 2010.

[7] Vargantwar P.H., Brannock M.C., Smith S.D., Spontak R.J., "Midblock sulfonation of a model long-chain poly(p-tert-butylstyrene-b-styrene-b-p-tert-butylstyrene) triblock copolymer", *J Mater Chem,* 22(48):25262–71, 2012.

[8] Vargantwar P.H., Brannock M.C., Tauer K., Spontak R.J., "Midblock-sulfonated triblock ionomers derived from a long-chain poly[styrene-b-butadiene-b-styrene] triblock copolymer", *J Mater Chem A , (*10):3430–9, 2013.

[9] Xie H.Q., Chen Y., Guan J.G., Xie D., "Novel method for preparation of quaternary ammonium ionomer from epoxidized styrene–butadiene–styrene triblock copolymer and its use as compatibilizer for blending of styrene–butadiene–styrene and chlorosulfonated polyethylene", *J Appl Polym Sci* , 99(4):1975–80, 2007.

[10] Disabb-Miller M.L., Johnson Z.D., Hickner M.A., "Ion Motion in Anion and Proton-Conducting Triblock Copolymers", *Macromolecules,* 46(3):949–56, 2013.

[11] Yoon J., Kang D., Won J., Park J.Y., Kang Y.S., "Dye-sensitized solar cells using ion-gel electrolytes for long-term stability", *J Power Sources*, 201:395–401, 2012.

[12] Al-Mohsin H.A., Mineart K.P., Spontak R.J., "Highly Flexible Aqueous Photovoltaic Elastomer Gels Derived from Sulfonated Block Ionomers", *Adv Energy Mater*.; 5(8):1401941, 2015.

[13] Choi J.H., Willis C.L., Winey K.I., "Structure-property relationship in sulfonated pentablock copolymers", *J Memb Sci, 3*94–395:169–74, 2012.

[14] Choi J.H., Willis C.L., Winey K.I., "Effects of neutralization with Et3Al on structure and properties in sulfonated styrenic pentablock copolymers", *J Memb Sci*, 428:516–22, 2013.

[15] Lee J.W., Hong S.M., Kim J., Koo C.M., "Novel sulfonated styrenic pentablock copolymer/silicate nanocomposite membranes with controlled ion channels and their IPMC transducers", *Sensors Actuators B Chem*, 162(1):369–76, 2012.

[16] Lee J.W., Lee J.H., Kim M., Hong S.M., Koo C.M., "Thermal annealing effects on the physical properties of styrenic pentablock ionomers and their electromechanical responses", *J Nanosci Nanotechnol,* 13(5):3606–10, 2013.

[17] Lee J.W., Hong S.M., Koo C.M., "High-performance polymer ionomer–ionic liquid membrane IPMC actuator", *Res Chem Intermed*, 40(1):41–8, 2014.

[18] Vargantwar P.H., Roskov K.E., Ghosh T.K., Spontak R.J., “Enhanced Biomimetic Performance of Ionic Polymer–Metal Composite Actuators Prepared with Nanostructured Block Ionomers”, *Macromol Rapid Commun.*, 33(1):61–8, 2011.

[19] Vargantwar P.H., Shankar R., Krishnan A.S., Ghosh T.K., Spontak R.J., “Exceptional versatility of solvated block copolymer/ionomer networks as electroactive polymers”, *Soft Matter.*, 7(5):1651–5, 2011.

[20] Mineart K.P., Al-Mohsin H.A., Lee B., Spontak R.J., “Water-induced nanochannel networks in self-assembled block ionomers”, *Appl Phys Lett.*, 108(10):101907, 2016.

[21] Dai Z., Deng J., Aboukeila H., Yan J., Ansaloni L., Mineart K.P., Giacinti B. M., Spontak R.J., “Deng L. Highly CO2-permeable membranes derived from a midblock-sulfonated multiblock polymer after submersion in water”, *NPG Asia Mater*, 11(1), 2019.

[22] Kim H., Hong J., Park K.Y., Kim H., Kim S.W., Kang K., “Aqueous rechargeable Li and Na ion batteries”, *Chemical Reviews*, Vol. 114, p. 11788–827, 2014.

[23] Suo L., Borodin O., Gao T., Olguin M., Ho J., Fan X., Luo C., Wang C., Xu K., “Water-in-salt” electrolyte enables high-voltage aqueous lithium-ion chemistries”, *Science*, 350(6263):938–43, 2015.

[24] Dubouis N., Lemaire P., Mirvaux B., Salager E., Deschamps M., Grimaud A., “The role of the hydrogen evolution reaction in the solid-electrolyte interphase formation mechanism for ": Water-in-Salt " electrolytes”, *Energy Environ Sci.*, 11(12):3491–9, 2018.

[25] Zhang L., Wu H., Yan Y., Wang X., Lou X.W., “Hierarchical MoS2 microboxes constructed by nanosheets with enhanced electrochemical properties for lithium storage and water splitting”, *Energy Environ Sci.*, 7(10):3302–6, 2014.

[26] Wang J.G., Liu H., Zhou R., Liu X., Wei B., “Onion-like nanospheres organized by carbon encapsulated few-layer MoS2 nanosheets with enhanced lithium storage performance”,. *J Power Sources,* 413:327–33, 2019.

[27] Quan T., Xu Y., Tovar M., Goubard-Bretesché N., Li Z., Kochovski Z., Kirmse H., Skrodczky K., Mei S., Yu H., Abou-Ras D., Wagemaker M., Lu Y., “Hollow MoS 3 Nanospheres as Electrode Material for “Water-in-Salt” Li–Ion Batteries”, *Batter Supercaps,* 27;3(8):747–56, 2020.

[28] Mineart K.P., Jiang X., Jinnai H., Takahara A., Spontak R.J., “Morphological investigation of midblock-sulfonated block ionomers prepared from solvents differing in polarity”, *Macromol Rapid Commun.,* 36(5):432–8, 2015.

[29] Afanasiev P., Xia G.F., Berhault G., Jouguet B., Lacroix M., “Surfactant-assisted synthesis of highly dispersed molybdenum sulfide”, *Chem Mater,* 11(11):3216–9, 1999.

[30] Mineart K.P., Jiang X., Jinnai H., Takahara A., Spontak R.J., “Morphological Investigation of Midblock-Sulfonated Block Ionomers Prepared from Solvents Differing in Polarity”, *Macromol. Rapid Commun.,* 36: 432-438, 2015.

Appendix B: Fabrication and characterization of meltblown Poly(Vinylidene difluoride) membranes

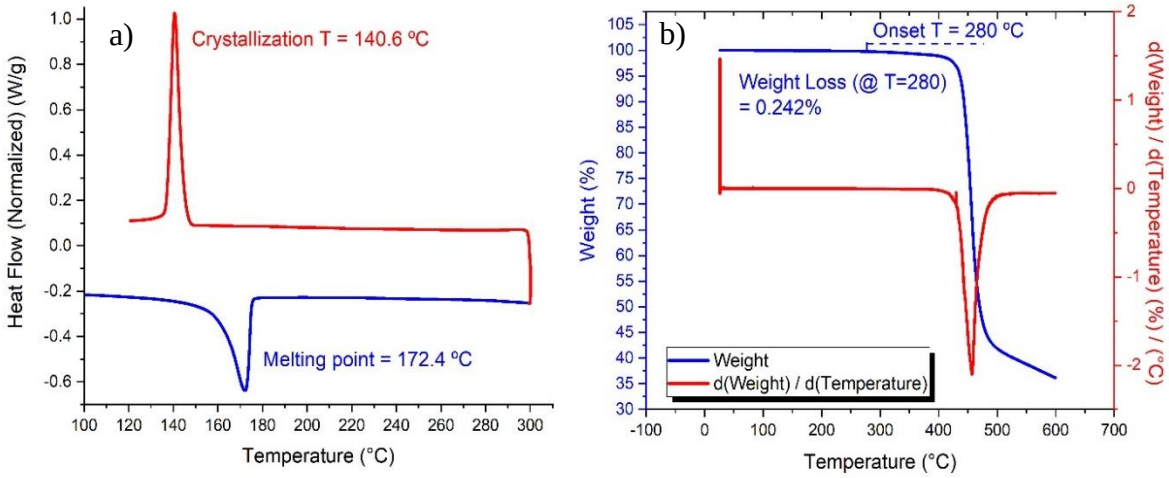

Figure 1. DSC (a) and TGA (b) of PVDF Kynar® resin RC 10,287.

Rheological experiments

Temperatures = 200/220/240/260 ºC

Steady shear experiment

Shear rate range = 0.01 – 100 s^{-1}

Geometry: parallel plate

Oscillatory experiment

%strain = 10%

Frequency (ω) range = 0.01 to 600 s^{-1}

Geometry: parallel plate

Cox-Merz rule: $\eta(\omega) = \eta(\dot{\gamma})$

Capillary rheometry

Shear rate range (s-1) = 100 - 10000

Geometries (Length:Diameter): 5:1, 20:1, 30:1

End pressure effect

We used equation 1 (Bagley corrections) to determine the true shear stress [1].

$$\tau = \frac{P}{4(L/D + e)} \quad \textbf{(1)}$$

where, τ is the true shear stress, P is the test pressure, L/D is the die length to diameter ratio and e is the die-length correction.

Non-homogeneous flow

We used equation 2 (Rabinowitz corrections) to determine the true shear rate [1].

$$\dot{\gamma} = \frac{\dot{\gamma}_{ap}}{4}\left[3 + \frac{d\log\dot{\gamma}_{ap}}{d\log\tau}\right] \quad \textbf{(2)}$$

where, $\dot{\gamma}$ is the true shear rate, $\dot{\gamma}_{ap}$ is the apparent shear rate, and $d(\log\dot{\gamma}_{ap})/d(\log\tau)$ is the slope of the curve $\log\dot{\gamma}_{ap}$ *vs* $\log\tau$, and τ is the true shear stress from equation 1.

By superimposing the data from these three experiments we were able to create viscosity curves over a wide range of shear rates, *i.e.* from 0.01 to 10000 s^{-1}. Figure 1 shows an example of the superimposition.

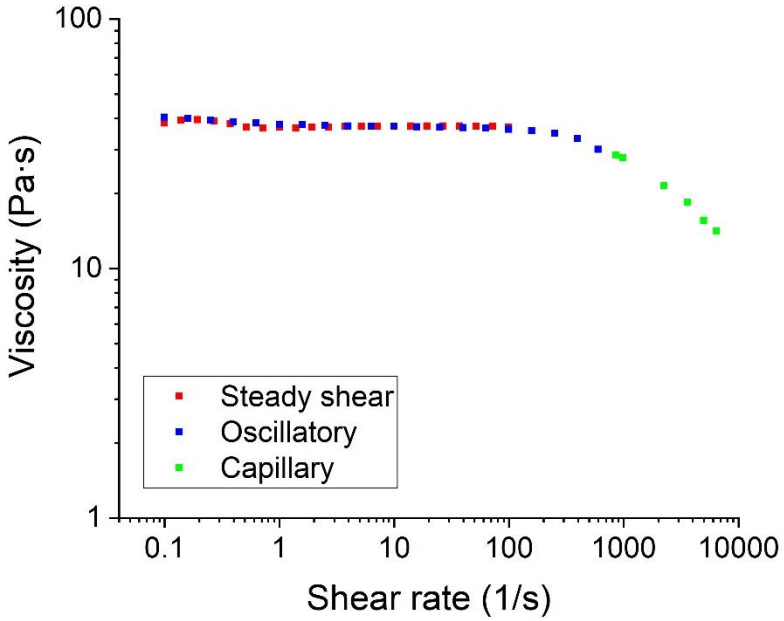

Figure 2. Viscosity curves from steady shear, oscillatory, and capillary rheometry experiments of PVDF Kynar® resin RC 10,287 at 200°C.

Cristallinity across Fiber Cross-Section

We soaked both the as-received PVDF pellets and the melt-blown PVDF membranes in 1M $LiPF_6$ EC/DMC battery electrolyte at room temperature for 4 weeks, while continuously stirring the solution. No visible dissolution of the membranes or the polymer pellets was detected. The fibers absorbed electrolyte and did not dissolve at room temperature. By visual inspection, the polymer pellets did not absorb electrolyte. Our explanation for this phenomenon is a change in crystallinity across the fiber cross-section: a highly-crystalline core prevents the fiber from dissolving. Moreover, because the difference in crystallinity between the polymer pellets (53%) and the fibers (48%) is small, the only difference in terms of crystalline and amorphous regions between the polymer pellets and the fibers is the presence of a second population of crystals in the fibers (visible in the DSC experiment). We used electron diffraction TEM to explore the change in crystallinity across the fiber cross-section[1]. We embedded the fiber mat in an epoxy resin and we used Focused Ion Beam etching to make a clean cut of the fiber cross-sections (Fig. 3a). We

examined the fiber mats with a Talos F200X TEM, and we used a bar across the fiber cross-sections as a beam-stopper to cover the bright central beam spot so that more diffuse intensity spots could be captured. It was possible to notice a change in the diffraction patterns (in both intensity spots and concentric rings) while moving the bar across the fiber cross-section (Fig. 3 b,c,d), meaning that there was a difference in crystallinity across the cross-section. Unfortunately, the bar was too large to be able to quantify the change in crystallinity.

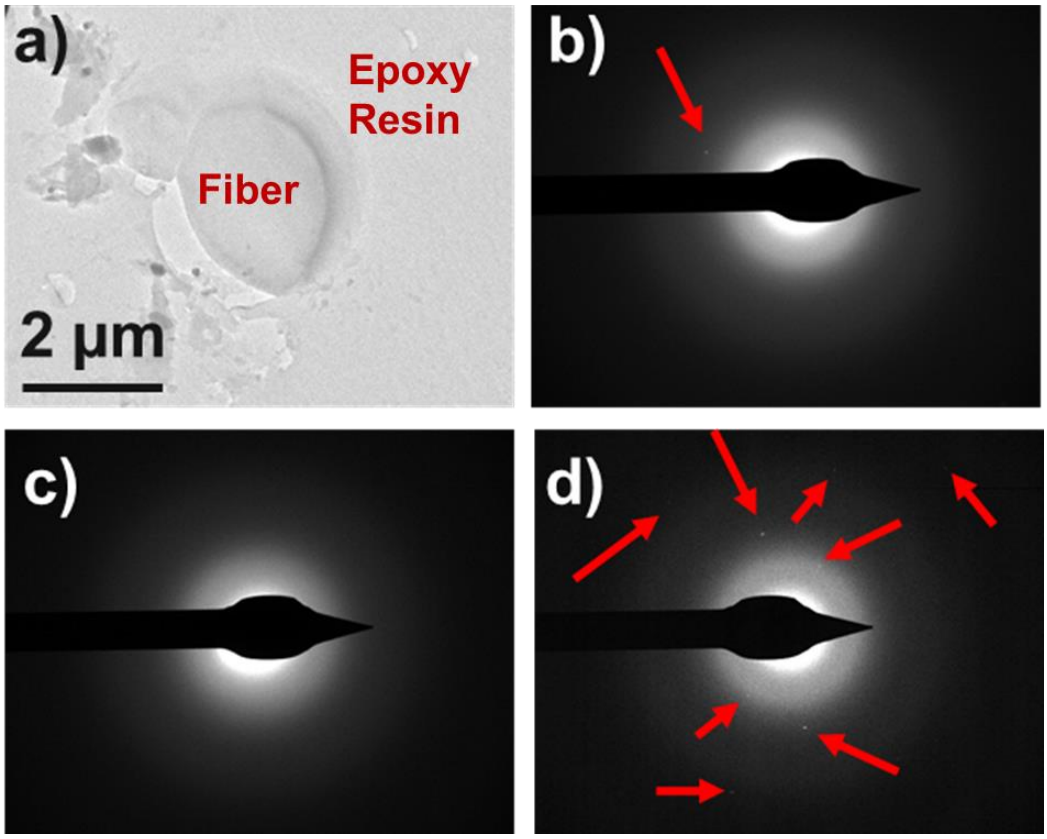

Figure 3. TEM image of fiber cross-section (a), TEM diffraction patterns at different positions of the beam-stopper bar (b), (c), and (d). Red arrows indicate diffraction intensity spot.

Table 1. Tensile properties of four representative meltblown PVDF samples.

	Cross direction		Machine Direction	
Sample	Peak load (kPa)	Strain at break (%)	Peak load (kPa)	Strain at break (%)
3	0.62	11	1.52	8
8	0.48	6	0.90	6
12 (@ 40g m^{-2})	1.24	11	2.28	9
18	0.62	9	1.34	6

References

[1] An B.S., Kwon Y., Cha H.W., Kang M.C., Oh J.S., Yang C.W., "Quantification of crystallinity using zero-loss filtered electron diffraction", *Microsc Res Tech.*;82:39–46, 2019.

Appendix C: Melt-blown PVDF as A Li-Ion Battery Separator

FT-IR

The β-phase of PVDF contains the largest spontaneous polarization, useful for pyro- and piezoelectricity. Among the 3 electroactive phases of PVDF (β, γ, and δ), γ and δ are rare and difficult to obtain, and to quantify the most electroactive phase (β) we need to look for peaks specific of β-phase. In the absence of a peak at 1234 cm^{-1}, specific of γ-phase, we can assume that peaks at 763 and 840 cm^{-1} are specific of the β-phase [1]. As we can see from Fig. 1, the unprocessed polymer has the highest β-phase content (67%), which decreases after meltblowing (55%) and again after melt-pressing the mats (50%). The meltblowing process involves a fast re-crystallization from the melt, which, together with the increase in polymer chain orientation due to filament stretching, keeps the β-phase content high [1,2]. We also noted a high retention of static electricity in the meltblown mats. Melt-pressing the polymer partially melts the fibers at their cross-section and the slow re-crystallization slightly decreases both β-phase content and static electricity retention.

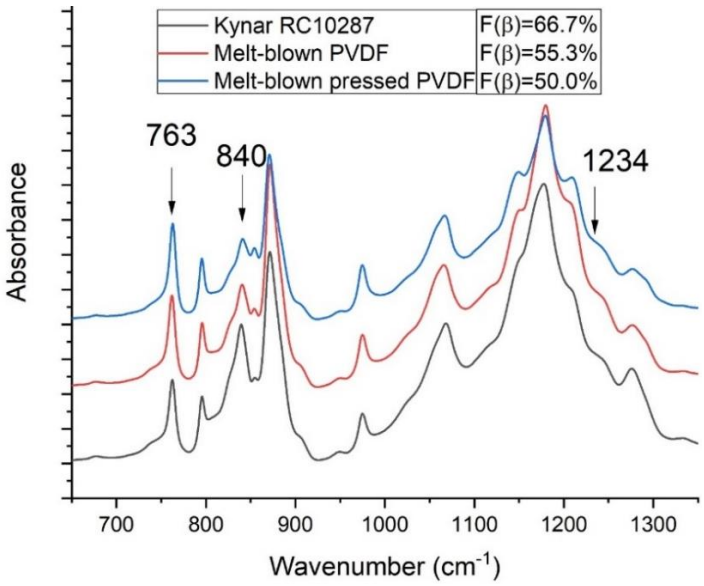

Figure 1. FT-IR spectra of unprocessed PVDF Kynar® resin 10,287, meltblown PVDF, meltblown pressed PVDF and their respective β-phase content.

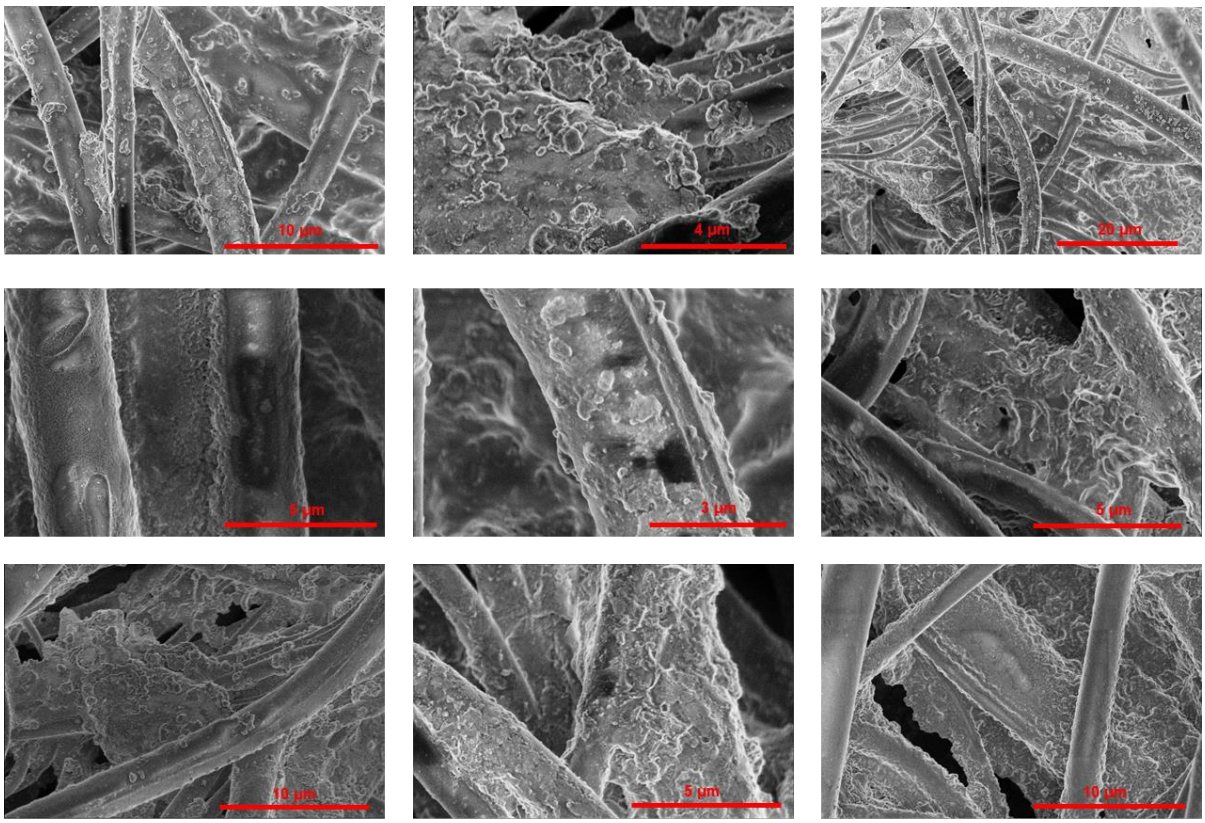

Figure 2. SEM images at different locations of meltblown PVDF after cycling in a Li/$LiCoO_2$ cell and vacuum-drying the mat.

References

[1] Cai, X., Lei, T., Sun, D. & Lin, L., "A critical analysis of the α, β and γ phases in poly(vinylidene fluoride) using FTIR". *RSC Adv.* **7**, 15382–15389, 2017.

[2] Yang, D. & Chen, Y., "β-phase formation of poly(vinylidene fluoride) from the melt induced by quenching". *J. Mater. Sci. Lett.* 6, 599–603, 1987.

Appendix D: Poly(Vinylidene difluoride) Soft Dendritic Colloids as Li-Ion Battery Separators

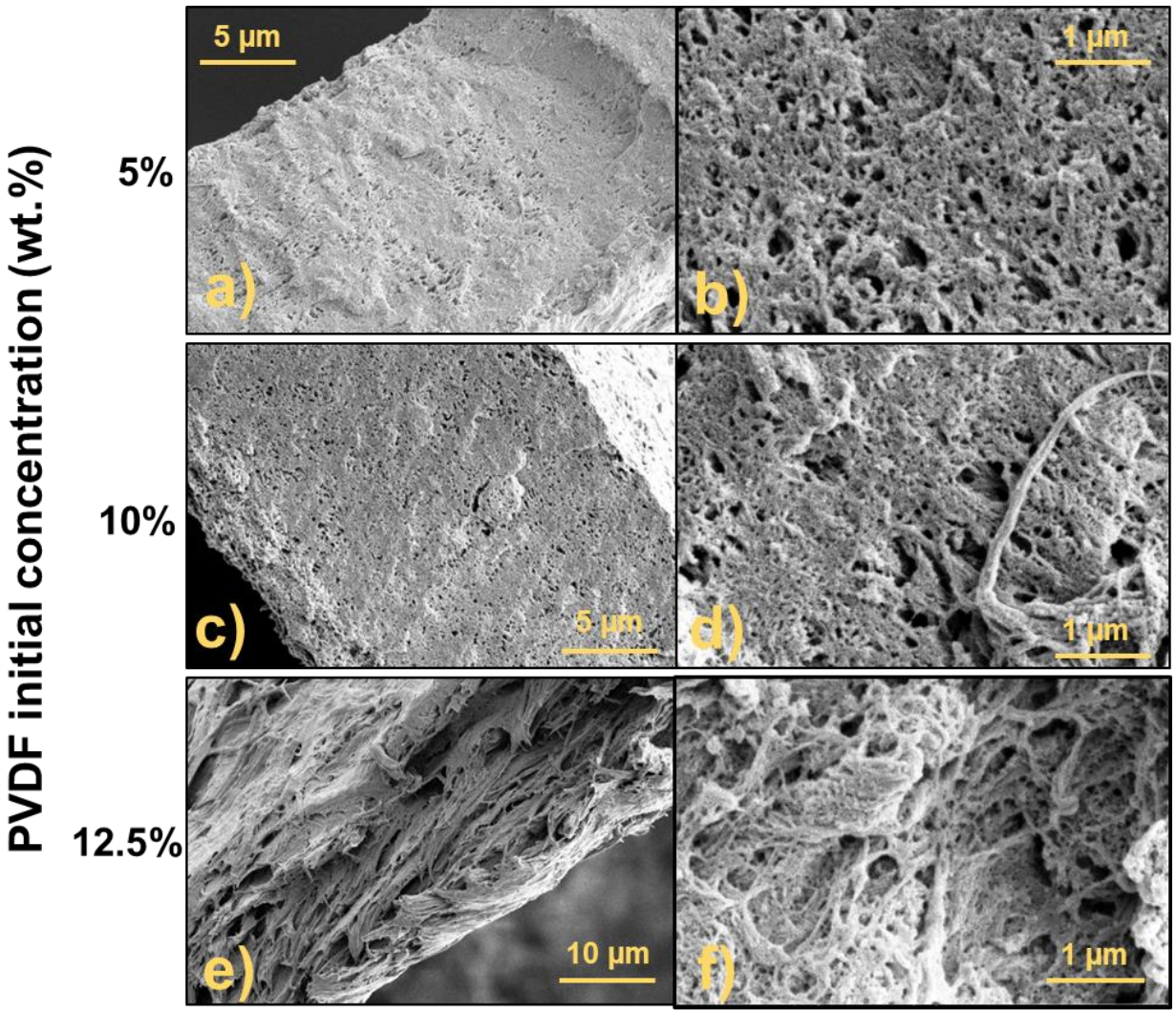

Figure 1. Scanning electron micrographs of membranes' cross-sections at different magnifications of SDC fibers (a, b), SDC fibers-NS intermediates (c, d) and NSs (e, f).

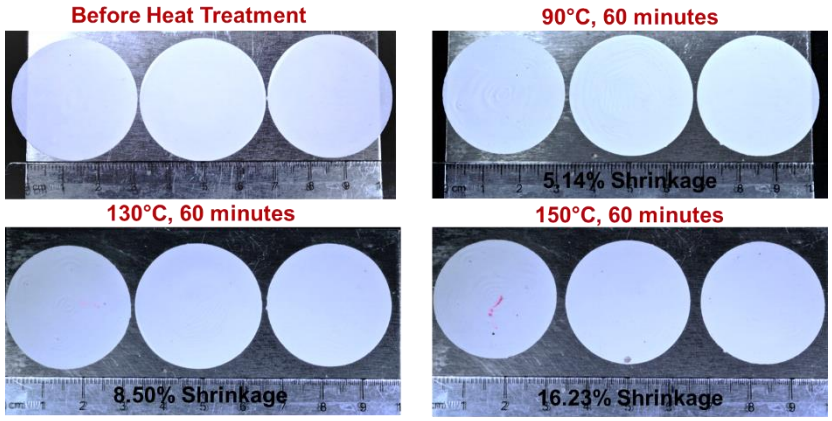

Figure 2. Thermal stability of 10% PVDF SDC membrane membranes following exposure to increasing temperatures. The SDC fibers-NS intermediate membranes show that the PVDF membranes display minimal shrinkage following exposure at temperature far above polyolefin melting points.

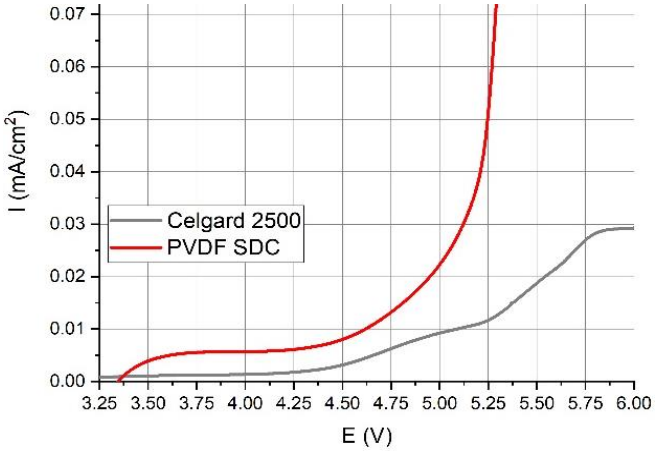

Figure 3. Oxidative limit for Celgard® and PVDF SDC Fibers-NS membranes. The oxidative limit of PVDF SDC membranes is below 10 µA/cm2 at 4.5 V, appropriate for commercial use.